

BULK NUCLEAR PROPERTIES FROM DYNAMICAL DESCRIPTION OF HEAVY-ION  
COLLISIONS

By

Jun Hong

A DISSERTATION

Submitted to  
Michigan State University  
in partial fulfillment of the requirements  
for the degree of

Physics-Doctor of Philosophy

2016

## ABSTRACT

### BULK NUCLEAR PROPERTIES FROM DYNAMICAL DESCRIPTION OF HEAVY-ION COLLISIONS

By

Jun Hong

Mapping out the equation of state (EOS) of nuclear matter is a long standing problem in nuclear physics. Both experimentalists and theoretical physicists spare no effort in improving understanding of the EOS. In this thesis, we examine observables sensitive to the EOS within the pBUU transport model based on the Boltzmann equation. By comparing theoretical predictions with experimental data, we arrive at new constraints for the EOS. Further we propose novel promising observables for analysis of future experimental data.

One set of observables that we examine within the pBUU model are pion yields. First, we find that net pion yields in central heavy-ion collisions (HIC) are strongly sensitive to the momentum dependence of the isoscalar nuclear mean field. We reexamine the momentum dependence that is assumed in the Boltzmann equation model for the collisions and optimize that dependence to describe the FOPI measurements of pion yields from the Au+Au collisions at different beam energies. Alas such optimized dependence yields a somewhat weaker baryonic elliptic flow than seen in measurements.

Subsequently, we use the same pBUU model to generate predictions for baryonic elliptic flow observable in HIC, while varying the incompressibility of nuclear matter. In parallel, we test the sensitivity of pion multiplicity to the density dependence of EOS, and in particular to incompressibility, and optimize that dependence to describe both the elliptic flow and pion yields. Upon arriving at acceptable regions of density dependence of pressure and energy, we compare our constraints on EOS with those recently arrived at by the joint experiment and theory effort FOPI-IQMD. We should mention that, for the more advanced observables from HIC, there remain discrepancies of up to 30%, depending on energy, between the theory and experiment, indicating the limitations of

the transport theory.

Next, we explore the impact of the density dependence of the symmetry energy on observables, motivated by experiments aiming at constraining the symmetry energy. In contradiction to IBUU and ImIQMD models in the literature, that claim sensitivity of net charged pion yields to the density dependence of the symmetry energy, albeit in direction opposite from each other, we find practically no such sensitivity in pBUU. However, we find a rather dramatic sensitivity of differential high-energy charged-pion yield ratio to that density dependence, which can be qualitatively understood, and we propose that that differential ratio be used in future experiments to constrain the symmetry energy.

Finally, we present Gaussian phase-space representation method for studying strongly correlated systems. This approach allows to follow time evolution of quantum many-body systems with large Hilbert spaces through stochastic sampling, provided the interactions are two-body in nature. We demonstrate the advantage of the Gaussian phase-space representation method in coping with the notorious numerical sign problem for fermion systems. Lastly, we discuss the difficulty in trying to stabilize the system during its time evolution, within the Gaussian phase-space method.

Copyright by  
JUN HONG  
2016

## ACKNOWLEDGEMENTS

It has been a long journey for me, and I owe my deep appreciation to the many people who provided care and support along the way. First of all, I would like to thank my advisor Pawel Danielewicz. His broad knowledge and passion shows me a great example of a theoretical nuclear physicist. Despite his busy schedule, he makes every effort to provide weekly advise on our research projects, even it means skype meeting during a layover in the airport.

Special thanks are addressed to Betty Tsang and Bill Lynch. From the many helpful discussions, I gained better understanding in the related research projects and beyond. I am also thankful for their kind help in some of my personal issues. I gained tremendous experience collaborating with HiRA group. From symmetry energy club to close work with some of the graduate students, I learned many specifics of experimental measurements and analysis, as well as making many new friends. I enjoyed conversations with Justin Estee, Rachel Hodges, Setiawan Hananiel, Daniel Coupland, Mike Youngs.

I would like to acknowledge the National Science Foundation for supporting my research projects. I enjoyed the nice working environment provided by the Department of Physics and Astronomy and the National Superconducting Cyclotron Laboratory.

Brent Barker has been my officemate, group member, house mate and will be a good friend of mine forever. His help and encouragement lifted me during my difficult times over the years. We shared good memories in our daily meetings, we had many fruitful conversations online and off. Yuanyuan Zhang was another group member that later became my close friend. We learn and grow together, and I thank her for her genuine friendship.

I would like to express my gratitude to Prof. Filomena Nunes. My one-year research experience with her was wonderful. And she has been very understanding and supportive ever since. I thank Prof. Artimes Spyrou for her kindness in providing many nice clothes for little Audrey and useful tips for me.

Rebecca Shane has been a good friend for many years. Having thanksgiving dinner at her place has become one of my family tradition since 2011. I owe her many thanks for all her help. I am grateful to have known Sarah Comstock and Zaje Harrell during our lunch talks at the daycare. Those will be some of the unforgettable moments in my life.

I also thank many of the friends I made in the beginning of my graduate program, Adam Fritsch, Scott Bustabad, Lingying Lin, Michael Scott, River Huang, Ding Wang, the list goes on. Last but not least, I would like to thank my father Wenzhang Hong and my mother Chunhua Wu for their unconditional love and support. I am most thankful for having my husband Yaxing Zhang and daughter Audrey Zhang these years. Thanks for everything.

## TABLE OF CONTENTS

LIST OF FIGURES . . . . .	ix
CHAPTER 1 INTRODUCTION . . . . .	1
1.1 Heavy Ion Collisions . . . . .	2
1.2 Pions . . . . .	3
1.3 Transport theory . . . . .	4
1.3.1 Density functional method . . . . .	4
1.3.2 Transport models . . . . .	5
1.3.3 Details in the BUU model . . . . .	6
CHAPTER 2 CONSTRAINTS ON THE MOMENTUM DEPENDENCE OF NUCLEAR MEAN FIELD . . . . .	10
2.1 Momentum dependence of nuclear mean field . . . . .	10
2.1.1 Momentum-dependent mean field in pBUU model . . . . .	11
2.2 Pion observables . . . . .	12
2.3 Optical potential comparison . . . . .	16
2.4 Elliptic flow . . . . .	22
2.5 Conclusions . . . . .	32
CHAPTER 3 CONSTRAINTS ON NUCLEAR INCOMPRESSIBILITY . . . . .	33
3.1 Introduction . . . . .	33
3.2 Incompressibility and isoscalar Giant Monopole Resonance . . . . .	34
3.3 Elliptic flow . . . . .	34
3.3.1 Elliptic flow and impact parameter . . . . .	39
3.3.2 Elliptic flow and effective mass . . . . .	41
3.3.3 Elliptic flow and incompressibility . . . . .	43
3.4 Constraints on nuclear incompressibility from flow and pion observables . . . . .	45
3.5 Conclusion . . . . .	54
CHAPTER 4 CONSTRAINTS ON SYMMETRY ENERGY AT SUPRANORMAL DEN- SITIES . . . . .	55
4.1 Introduction to symmetry energy . . . . .	55
4.2 Motivation . . . . .	58
4.3 Charged pion ratios . . . . .	59
4.4 Pion potential . . . . .	63
4.5 Differential pion ratios . . . . .	65
4.6 Isospin fractionation . . . . .	71
4.7 Conclusions . . . . .	76
CHAPTER 5 GAUSSIAN QMC METHOD . . . . .	78

5.1	Introduction . . . . .	78
5.2	Phase space methods . . . . .	79
5.2.1	Classical phase-space representations . . . . .	79
5.2.2	Quantum phase-space representations . . . . .	79
5.3	Gaussian phase-space representation . . . . .	80
5.3.1	Gaussian phase-space representations for Bosons . . . . .	81
5.3.2	Gaussian phase-space representations for Fermions . . . . .	84
5.4	Properties of Gaussian phase-space method for Fermions . . . . .	85
5.4.1	Single-mode Gaussian operator . . . . .	85
5.4.2	Completeness . . . . .	86
5.5	Free gas . . . . .	87
5.6	Fermi-Bose modeling . . . . .	88
5.7	Conclusion . . . . .	93
CHAPTER 6 CONCLUSIONS . . . . .		95
BIBLIOGRAPHY . . . . .		97

## LIST OF FIGURES

Figure 1.1	The before and after sketch of an intermediate energy nuclear collision. . . . .	3
Figure 2.1	Pion multiplicity in central Au+Au collisions. Symbols represent data of the FOPI Collaboration [1]. The lines represent pBUU calculations when following either the momentum-independent MF (left panel) or the past flow-optimized momentum-dependent MF (right panel). Solid lines are predictions for $\pi^-$ , and dashed lines are predictions for $\pi^+$ . The experimental error bars are about the size of symbols. . . . .	14
Figure 2.2	Pion multiplicity in central Au+Au collisions, as a function of beam energy. Symbols represent data of the FOPI collaboration[1], , while lines represent the pBUU calculations with the $N_\pi$ -adjusted momentum-dependent MF. The experimental error bars are about the size of symbols. . . . .	15
Figure 2.3	Optical potential in nuclear matter at different indicated densities, as a function of momentum. Dashed and solid lines represent, respectively, the $v_2$ -optimized and $N_\pi$ -adjusted MFs. . . . .	17
Figure 2.4	Optical potential in nuclear matter at different indicated densities, as a function of nucleon energy. Dashed and solid lines represent, respectively, UV14+UVII variational calculations and our $N_\pi$ -adjusted MF. . . . .	18
Figure 2.5	Optical potential in nuclear matter at different indicated densities, as a function of nucleon energy. Dashed and solid lines represent, respectively, AV14+UVII variational calculations and our $N_\pi$ -adjusted MF. . . . .	19
Figure 2.6	Optical potential in nuclear matter at different indicated densities, as a function of nucleon momentum. Dashed and solid lines represent, respectively, Dirac-Brueckner-Hartree-Fock calculations and our $N_\pi$ -adjusted MF. . . . .	20
Figure 2.7	Optical potential in nuclear matter at different indicated densities, as a function of nucleon energy. Dashed and solid lines represent, respectively, UV14+TNI variational calculations and our $N_\pi$ -adjusted MF. . . . .	21
Figure 2.8	Schematic drawing of the geometry in a HIC. The beam line is along z axis, x axis is parallel to the impact parameter direction. x-z plane is defined as the reaction plane, and y axis is perpendicular to the reaction plane. . . . .	22
Figure 2.9	Particle emission processes are shown with respect to the reaction plane. The blockage of spectator particles leads to the out-of-plane emission in the early stage of the reactions. . . . .	23

Figure 2.10	Ratio of out of reaction plane to in-plane proton yields, as a function of transverse momentum. Symbol s represent data from the measurements of the KaoS Collaboration of mid-peripheral Bi+Bi collisions at the beam energy of 400A MeV ( $b \simeq 8.7\text{fm}$ ) [2]. Solid line represents pBUU calculations with the $N_\pi$ -adjusted momentum-dependent MF and dashed line represents calculations with $v_2$ -optimized momentum-dependent MF. The indicated theoretical errors are statistical, associated with the Monte-Carlo sampling in the transport calculations. . . . .	25
Figure 2.11	Elliptic flow of particle mass A=1 particles, as a function of transverse momentum. Symbols represent data from the measurements of the FOPI Collaboration of mid-peripheral Au+Au collisions at the beam energy of 400A MeV ( $b \sim 2.0 - 5.3\text{fm}$ ). The shaded region represents pBUU calculations with the $N_\pi$ -adjusted momentum-dependent MF. The indicated theoretical errors are statistical, associated with the Monte-Carlo sampling in the transport calculations. . . . .	26
Figure 2.12	Elliptic flow of proton, as a function of transverse momentum. Symbols represent data from the measurements of the FOPI Collaboration of mid-peripheral Au+Au collisions at the beam energy of 600A MeV ( $b \sim 2.0 - 5.3\text{fm}$ ). The shaded region represents pBUU calculations with the $N_\pi$ -adjusted momentum-dependent MF. The indicated theoretical errors are statistical, associated with the Monte-Carlo sampling in the transport calculations. . . . .	28
Figure 2.13	Transverse rapidity distribution of protons. Rapidity values $y_x$ are scaled with the projectile rapidity in the center-of-mass frame: $y_{x0} = y_x/y_p$ . The transverse rapidity distribution with respect to $y_{xm0}$ is obtained with a midrapidity cut of $ y_{z0}  < 0.5$ . Triangles represent data from the measurements of the FOPI Collaboration of central Au+Au collisions at the beam energy of 400A MeV ( $b=1\text{fm}$ ). The squares represent pBUU calculations with the $N_\pi$ -adjusted momentum-dependent MF. . . . .	29
Figure 2.14	Transverse rapidity distribution of tritons. Rapidity values $y_x$ are scaled with the projectile rapidity in the center-of-mass frame: $y_{x0} = y_x/y_p$ . The transverse rapidity distribution with respect to $y_{xm0}$ is obtained with a midrapidity cut of $ y_{z0}  < 0.5$ . Triangles represent data from the measurements of the FOPI Collaboration of central Au+Au collisions at the beam energy of 400A MeV ( $b=1\text{fm}$ ). The squares represent pBUU calculations with the $N_\pi$ -adjusted momentum-dependent MF. . . . .	30

- Figure 2.15 Transverse rapidity distribution of Helium 3. Rapidity values  $y_x$  are scaled with the projectile rapidity in the center-of-mass frame:  $y_{x0} = y_x/y_p$ . The transverse rapidity distribution with respect to  $y_{xm0}$  is obtained with a midrapidity cut of  $|y_{z0}| < 0.5$ . Triangles represent data from the measurements of the FOPI Collaboration of central Au+Au collisions at the beam energy of 400A MeV ( $b=1\text{fm}$ ). The squares represent pBUU calculations with the  $N_\pi$ -adjusted momentum-dependent MF. . . . . 31
- Figure 3.1 Elliptic flow of A=1 (proton) particles, as a function of scaled transverse momentum. Closed dots represent data from the measurements of the FOPI Collaboration of mid-peripheral Au+Au collisions at the beam energy of 400A MeV ( $b \sim 2.0 - 5.3\text{fm}$ ). The open squares represent pBUU calculations with the soft equation of state ( $K=210$  MeV), which was adjusted to KaoS flow data. The triangles represent pBUU calculations with stiff equation of state ( $K=380$  MeV) and no momentum dependence in MF. . . . . 36
- Figure 3.2 Elliptic flow of A=2 (deuteron) particles, as a function of scaled transverse momentum. Closed dots represent data from the measurements of the FOPI Collaboration of mid-peripheral Au+Au collisions at the beam energy of 400A MeV ( $b \sim 2.0 - 5.3\text{fm}$ ). The open squares represent pBUU calculations with the soft equation of state ( $K=210$  MeV), which was adjusted to KaoS flow data. The triangles represent pBUU calculations with stiff equation of state ( $K=380$  MeV) and no momentum dependence in MF. . . . . 37
- Figure 3.3 Elliptic flow of A=3 (triton and Helium 3) particles, as a function of scaled transverse momentum. Closed dots represent data from the measurements of the FOPI Collaboration of mid-peripheral Au+Au collisions at the beam energy of 400A MeV ( $b \sim 2.0 - 5.3\text{fm}$ ). The open squares represent pBUU calculations with the soft equation of state ( $K=210$  MeV), which was adjusted to KaoS flow data. The triangles represent pBUU calculations with stiff equation of state ( $K=380$  MeV) and no momentum dependence in MF. . . . 38
- Figure 3.4 Proton elliptic flow as a function of impact parameter, for Au+Au collisions at 1.2A GeV. Dots are calculation points for soft momentum dependent MF with  $m^*/m=0.782$  and  $K=270$  MeV, the line is for guidance purpose. In absence of deformation for colliding nuclei, due to symmetry, the elliptic flow needs to vanish at  $b=0$ . As geometry of the reaction becomes more asymmetric with increasing impact parameter, so does the magnitude of elliptic flow. At higher impact parameters, the flow saturates for a momentum-dependent MF. 40

Figure 3.5	Ratio of out-of-the-reaction-plane to in-plane proton yields, as a function of transverse momentum, in mid-peripheral Bi+Bi collisions at the beam energy of 400A MeV and impact parameter $b \sim 7.6\text{fm}$ . Symbols represent data from the measurements of the KaoS Collaboration[2]. Solid, dot-dashed and dashed lines represent pBUU calculations with MFs characterized by $K=270\text{MeV}$ and effective mass $m^*/m=0.8, 0.7$ and $0.6$ , respectively. . . . .	42
Figure 3.6	Ratio of out-of-the-reaction-plane to in-plane proton yields, as a function of transverse momentum, in mid-peripheral Bi+Bi collisions at the beam energy of 400A MeV and impact parameter $b \sim 7.6\text{fm}$ . Symbols represent data from the measurements of the KaoS Collaboration[2]. Dot-dashed, dashed, solid and dotted lines represent pBUU calculations with incompressibility $K=300, 270, 240$ and $210\text{MeV}$ , respectively, with effective mass $m^*=0.7m$ . . . . .	44
Figure 3.7	Ratio of out of reaction plane to in-plane proton yields, as a function of transverse momentum. Symbols represent data from the measurements of the KaoS Collaboration of mid-peripheral Bi+Bi collisions at the beam energies of 400A MeV and 700MeV ( $b=7.6\text{fm}$ )[2]. Shaded regions represent pBUU calculations with an optimal EOS for incompressibility between $K=240-300\text{MeV}$ . . . . .	47
Figure 3.8	Pion multiplicity in central Au+Au collisions vs beam energy. Symbols represent data of the FOPI Collaboration[1]. The shaded region represent pBUU calculations with the range of nuclear equation of state fitted to elliptic flow and pion yields simultaneously. . . . .	48
Figure 3.9	$\pi^+$ multiplicity in central Au+Au collisions vs beam energy. Symbols represent data of the FOPI Collaboration[1]. Solid and dashed lines represent calculations carried out with incompressibility $K=210$ and $270$ MeV, respectively, and the effective mass $m^*/m=0.75$ for both. . . . .	49
Figure 3.10	$\pi^-$ multiplicity in central Au+Au collisions. Symbols represent data of the FOPI Collaboration[1]. Solid and dashed lines represent calculations with incompressibility $K=210$ and $270$ MeV, respectively, both with the effective mass $m^*/m=0.75$ . . . . .	50
Figure 3.11	Ratio of out of reaction plane to in-plane proton yields, as a function of transverse momentum. Symbols represent data from the measurements of the KaoS Collaboration of mid-peripheral Bi+Bi collisions at the beam energy of 400A MeV ( $b=8.7$ fm)[2]. Dashed and solid lines represent pBUU calculations with incompressibility $K=210$ and $270$ MeV, respectively, both with the effective mass $m^*/m=0.75$ . . . . .	51

Figure 3.12	Energy per nucleon for symmetric nuclear matter as a function of scaled density. The solid lines represent constraints, upper and lower, on the energy arrived at by the FOPI-IQMD Partnership. The shaded region represents our conclusions, with the pion yields and elliptic flow testing the supranormal region. The vertical dashed lines show the rough density region that gets probed by the observables in the calculations. . . . .	52
Figure 3.13	Nuclear equation of state plotted as pressure in terms of scaled density. Patterned shaded areas represent constraints deduce by comparing transport theory to data on kaon multiplicity and on directed and elliptic flow. The solid line on the left represents the equation of state preferred by analysis of the recent giant monopole resonance (GMR) experiment. Dots represents the noninteracting Fermi gas and triangles represent the relativistic mean field (RMF) model NL3. The shaded regions, pink and blue, represent respective pressure constraints that can be deduced when relying on either an EOS with $K=240$ MeV or $K=300$ MeV within the pBUU transport model. The vertical dashed lines show the rough density region that gets probed by the observables in the calculations. . . . .	53
Figure 4.1	The multifaceted influence of the nuclear symmetry energy. [3] . . . . .	57
Figure 4.2	Density dependence of nuclear symmetry energy for 21 sets of Skyrme interaction parameters. Symbols represent momentum-dependent interactions in IBUU04 [4]. . . . .	58
Figure 4.3	(Color online) Pion ratios in central Au+Au collisions, as a function of beam energy. Data of the FOPI Collaboration are represented by filled triangles. The left panel compares predictions from IBUU and ImIQMD models to the data. The IBUU calculations employing stiff and soft symmetry energies are represented there by filled diamonds and filled circles, respectively. The ImIQMD employing stiff and soft symmetry energies are, on the other hand, represented there by filled squares and crosses, respectively. The right panel compares predictions from pBUU model to the data. Calculations employing $v_2$ -optimized MF and $N_\pi$ -adjusted MF are represented by filled circles and filled squares, respectively. In our calculations here, the potential part of the symmetry energy is linear in density. . . . .	61
Figure 4.4	(Color online) Ratio of net charged pion yields in central Au+Au collisions at 400A MeV and 200A MeV, as a function of the stiffness of symmetry energy $\gamma$ , from pBUU calculations using $N_\pi$ -adjusted MF. The dashed region represents the 400A MeV FOPI measurement. The theoretical errors are due to statistical sampling in the pBUU calculations. . . . .	62

Figure 4.5	(Color online) S-wave contribution to $\pi - {}^{197}\text{Au}$ optical potential. Solid line represents the work of Toki [5]. Short-dash, dotted and dash-dotted lines represent pion potentials from pBUU parameterization for $\gamma = 0.5, 1.0, 2.0$ , respectively, in the interaction part of the symmetry energy. Long dashed line represents the lack of corresponding potentials in the IBUU and ImIQMD models. . . . .	64
Figure 4.6	(Color online) Charged pion ratio in central Au+Au collisions at 200A MeV, as a function of kinetic energy in the center of mass frame, for different values of the stiffness $\gamma$ of the symmetry energy, from 0.5 to 2.0. The horizontal line represents the ratio of net charged pion yields. . . . .	66
Figure 4.7	(Color online) Charged pion ratio in central ${}^{124}\text{Sn} + {}^{132}\text{Sn}$ collisions at 300A MeV, as a function of kinetic energy in the center of mass frame, for different values of the stiffness $\gamma$ of the symmetry energy, from 0.5 to 2.0. . . . .	67
Figure 4.8	(Color online) Average center-of-mass kinetic energy of $\pi^+$ and $\pi^-$ in central Au+Au collisions at 200A MeV, plotted against stiffness $\gamma$ of the symmetry energy. . . . .	68
Figure 4.9	(Color online) Difference between average c.m. kinetic energy of $\pi^+$ and $\pi^-$ in central Au+Au collisions at 200A MeV, plotted against stiffness $\gamma$ of the symmetry energy. . . . .	70
Figure 4.10	(Color online) Ratio of neutron-to-proton numbers at supranormal net densities, $\rho > \rho_0$ , in central Au+Au collisions at 200A MeV, as a function of time. At early times, the numbers in the ratio are marginal, and the ratio, thus, not very meaningful. . . . .	71
Figure 4.11	Ratio of neutron-to-proton numbers, in central Au+Au collisions at the beam energy of 200A MeV and impact parameter $b=1\text{fm}$ , as a function of kinetic energy in center of mass frame. . . . .	72
Figure 4.12	Ratio of neutron-to-proton numbers, in central ${}^{132}\text{Sn} + {}^{124}\text{Sn}$ collisions at the beam energy of 200A MeV and impact parameter $b=1\text{fm}$ , as a function of kinetic energy in center of mass frame. . . . .	73
Figure 4.13	Ratio of neutron-to-proton numbers, in central ${}^{132}\text{Sn} + {}^{124}\text{Sn}$ collisions at the beam energy of 300A MeV and impact parameter $b=1\text{fm}$ , as a function of kinetic energy in center of mass frame. . . . .	74
Figure 4.14	Ratio of neutron-to-proton numbers, in central ${}^{132}\text{Sn} + {}^{124}\text{Sn}$ collisions at the beam energy of 300A MeV and impact parameter $b=3\text{fm}$ , as a function of kinetic energy in center of mass frame. . . . .	75

Figure 5.1 Average number of boson molecules as a function of time, in a system of single-mode boson molecules dissociating into two two-mode fermions, from a simulation within the Gaussian operator representation. Dashed line represent analytic solution using mean field approximation in Eq. 5.49. The system starts with 10 molecules and no fermions. In the specific case, the number bosonic molecules is calculated from the average 4000 trajectories. The sampling error is under control for a short time and then grows dramatically. 91

Figure 5.2 Average number of boson molecules as a function of time, in a system of single-mode boson molecules dissociating into two two-mode fermions, from a simulation within the Gaussian operator representation. Dashed line represent analytic solution using mean field approximation in Eq. 5.49. The system starts with 20 molecules and no fermions. In the specific case, the number bosonic molecules is calculated from the average 4000 trajectories. The sampling error is under control for a short time and then grows dramatically. 92

# CHAPTER 1

## INTRODUCTION

Exploration of bulk nuclear properties under a wide range of density and temperature is one of the central goals of nuclear physics. Nuclear equations of state (EOS) relate different thermodynamic characteristics of nuclear matter, such as energy or pressure with density and temperature. Nuclear matter itself stands for an infinite uniform nucleon system at some fixed ratio of neutron to proton density, with Coulomb interactions switched off. The EOS relations are relevant for many physical processes, e.g. excitation of giant collective resonances[6], the dynamics in heavy ion collision (HIC)[7], the properties of neutron stars[3], etc. In HIC, a wide range of density and temperature is achieved in the course of system evolution, providing study grounds to understand the EOS.

In astrophysical scenarios, pressure is one important macroscopic quantity that links to the data from HIC. For a system at net density  $\rho$ , proton-neutron asymmetry  $\alpha = (\rho_n - \rho_p)/(\rho_n + \rho_p)$ , and temperature  $T=0$ , the pressure  $P$  is related to energy per nucleon  $\frac{E}{A}(\rho, \alpha)$  with

$$P(\rho, \alpha) = \rho^2 \frac{\partial \frac{E}{A}(\rho, \alpha)}{\partial \rho}. \quad (1.1)$$

In many situations in nuclear physics, including various microscopic calculations, it is  $\frac{E}{A}(\rho, \alpha)$  that is arrived directly, and then the relation above is used to get the pressure.

Energy per nucleon in nuclear matter can be expanded in powers of the neutron-proton asymmetry  $\alpha$  of the system:

$$\frac{E}{A}(\rho, \alpha) = \frac{E}{A}(\rho, 0) + S(\rho)\alpha^2 + O(\alpha^4). \quad (1.2)$$

Only even powers survive in the above expression results from the fact that, nuclear interaction is symmetric for proton and neutron. The first term  $E/A(\rho, 0)$  represents the EOS for symmetric nuclear matter (SNM), which has been significantly constrained. At zero-temperature  $E/A = (\rho, 0)$  minimizes at -16MeV per nucleon, at normal density of  $\rho_0 = 0.16\text{fm}^{-3}$ . The nuclear incompress-

ibility  $K$  is the scaled curvature of energy at normal density, following is the relation between incompressibility and energy:

$$K = 9\rho^2 \frac{\partial^2 \frac{E}{A}}{\partial \rho^2}. \quad (1.3)$$

Nuclear incompressibility has been determined in nonrelativistic calculations to be  $240\text{MeV} \pm 20\text{MeV}$ , by studying excitations to the Giant Monopole Resonance (GMR). However, relativistic calculations claim a bit higher values, with  $K \approx 250\text{-}270\text{ MeV}$ [8]. Nuclear incompressibility conclusions impact research on collective motion in HIC and research on supernovae explosions and conversely. In this thesis, we reassess assumptions on incompressibility employed in transport for HIC, being inspired by the recent FOPI-IQMD analysis[9].

In the second term in the expansion of energy for asymmetric matter, the coefficient  $S(\rho)$  is called the symmetry energy. Different efforts have been undertaken, with moderate success at best, to constrain the density dependence of symmetry energy at  $\rho < \rho_0$ , such as using experimental data on isospin diffusion, Pygmy dipole resonances, giant dipole resonances, etc[10, 11, 12]. For  $\rho > \rho_0$ , our knowledge about the density dependence of  $S$  definitely remains poor[13, 4]. Therefore, EOS for asymmetric nuclear matter still has large uncertainties.

## 1.1 Heavy Ion Collisions

Intermediate energy ( $100A\text{ MeV} - 2A\text{ GeV}$ ) heavy ion collisions have been a powerful tool for extracting information on bulk properties of nuclear matter. Foremost, they remain an important testing ground in nuclear physics for studying the EOS at high temperature and high density. Heavy ion nominally refers to nuclei heavier than  ${}^4\text{He}$ , but significantly heavier nuclei are more suitable for EOS studies. Figure 1.1 shows the schematic sketch of before and after an intermediate-energy nuclear collision. The asymptotic distance between the centers of two nuclei about to collide, in direction transverse to the motion, is defined as the impact parameter  $b$ .

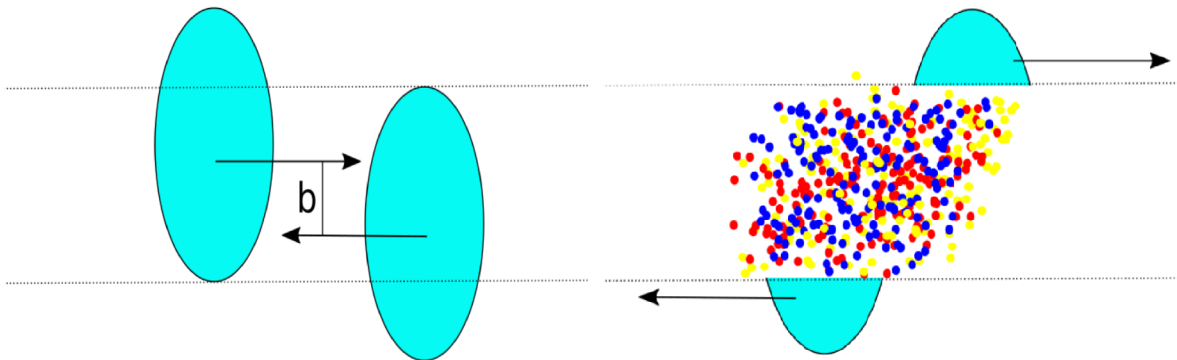


Figure 1.1 The before and after sketch of an intermediate energy nuclear collision.

During a collision, the region of overlap between the nuclei may reach density as high as two to three times the normal density, depending on the incident energy and impact parameter. The participants within that region go through complicated interactions that give rise to an excited, nearly equilibrated system. New particles are created if relative inter-particle energies are above the threshold; when the newly created particles travel through the medium, they further experience re-scattering and may get reabsorbed. As time progresses, elementary particles and heavier nuclear fragments order their motion towards a Hubble-type expansion, with a local cooling down, until they finally fly out of the reaction region.

## 1.2 Pions

In subatomic world, particles interact with each other by exchanging a force carrier. Pions act as the force carrier between nucleons (protons and neutrons). The attractive residual strong force holds the nucleus together. In 1930, the mass of pions were predicted by Hideki Yukawa, based

on the uncertainty principle, from measuring the range of the strong force between nucleons. He also predicted that pions have three charge states: positive, negative and neutral. Charged pions were discovered in 1947 in the cosmic ray interactions and the neutron pion wasn't discovered until accelerator experiments in 1950.

Pions are the lightest mesons and are composed of up and down quarks. The mass of charged pions is  $139.6 \text{ MeV}/c^2$ , and of neutron pion is  $135.0 \text{ MeV}/c^2$ . In intermediate energy HIC, they are the first mesons to be created as energy is raised. Charged pion ratio has been identified as a sensitive observable to symmetry energy, and it is further studied in this thesis.

## **1.3 Transport theory**

### **1.3.1 Density functional method**

To understand the measurements in HIC, theoretical models are needed to follow reaction process from contact to product detection, and to provide guidance to the underlying physics. The number of nucleons in intermediate energy HIC range from tens to hundreds; the degrees of freedom involved are too complicated to be treated in a full quantum mechanical manner. Transport model has been successful in characterizing the non-equilibrium dynamics in a nuclear reaction[14, 15, 16, 17, 18, 19, 20, 21, 22, 23].

Gross features of many body quantum systems are not likely to depend on details pertaining simultaneously to all particles in a system. Even the interaction of any individual particle with the rest is generally not likely to depend on such details. With that in mind, one can try to approximate the complicated many-body dynamics with a simplified one where the details of the many-body dynamics are averaged out. One primary example, where this is employed, is the Hartree-Fock method[24, 25]. In its basic form of the method, the two-body interactions are averaged out over positions of all particles. If more-particle effects matter within a system, a density functional is constructed dependent on single-particle orbitals. The characteristics of a specific ground state are found through a minimization of that functional. In the time-dependent case, equations of motion

are derived from a variational principle with the density functional.

In nuclear transport, the elementary dynamic quantity is the particle phase-space distribution. With this, the density functional theory becomes the Landau theory that historically has been put forward in the context of Fermi liquids. Within that theory simplifications in the direction of the Hartree-Fock practice are possible, yielding in particular the Skyrme-Hartree-Fock limit where the functional is presumed to depend on phase-space distributions only through simple spatial densities constructed from the phase-space distributions. Optical potentials in the single-particle description in terms of a wavefunction or a phase-space density have similar physics content and these descriptions formally merge in the nuclear matter limit.

A functional discussed above can be used to describe the energy and density profile for the ground state and, in a more general situation, the equation of state for an excited system. However, there is another average aspect of interactions, in that short-range encounters between particles[26] can abruptly change momenta of the particles and even particle existence. This obviously of utmost importance in a dynamic situation, even when it is of marginal impact on stationary quantities. In a description in terms of single-particle wave-function orbitals, those encounters are accounted for in terms of imaginary part of optical potential. In the Landau theory, the short-range encounters get described in terms of rates for processes occurring over short times and distances. Both approaches get generalized within nonequilibrium Green's function theory where single-particle equations contain terms that describe propagation as well as sink and source terms.

### **1.3.2 Transport models**

Early on, cascade model was developed to treat nucleon collisions in a fully microscopic manner, it is able to describe inclusive energy spectrums in intermediate energy HIC [27]. The limitation to cascade model is that it ignores the mean-field effects which are important for describing collective motions for nuclear matter. This inspires the development of more sophisticated semi-classical transport models later to take into account the nuclear mean field in the theories. Currently, there are two main types of transport models used in simulating HIC dynamics.

The Boltzmann-Uehling-Uhlenbeck (BUU) transport model utilizes Boltzmann equations to simulate HIC dynamics, it containing both mean field and hard nucleon-nucleon collisions. The Boltzmann equation can be derived from the Kadanoff-Baym equation [28] - it samples the quasi-particle distribution and describes the time evolution of the ensemble. It has been very successful in understanding the physics driving the HIC. Efforts were made to improve the model over the years. Bertsch *et al.* [22] introduced quasi-particle interactions in the Boltzmann equations. Danielewicz and Bertsch [23] introduced three-body interactions for particle formations. And the energy functional method for the mean field was introduced by Danielewicz [29].

Another important type of transport model is called quantum molecular dynamic (QMD), where individual particles are represented by a Gaussian wave packet with fixed width, the total wave function of the system is a product of all the Gaussian wave functions. The evolution of the coordinates and momenta for the wave packets are solved classically, following the Hamiltonian equations of motion. Both BUU and QMD models are semi-classical, and assign momentum and position to individual particles. The nucleon-nucleon interactions are accounted for in an effective mean field and in residual interaction. Particles travel through the mean field, and the residual interactions lead to collisions. Phenomenological expressions for effective nuclear interactions, yielding the EOS, are employed in the models.

In this thesis, we use the BUU transport model developed by Danielewicz et al. [23](often called pBUU) as our theoretical tool to study the EOS. We will elaborate on the methodology of the BUU transport model in the following subsection.

### **1.3.3 Details in the BUU model**

The Boltzmann equation was originally derived by L. Boltzmann in 1872 for a gas of classical particles with binary collisions[30], later Uehling and Uhlenbeck extended the equation to quantum gas[31]. The BUU model adopted the quasiparticle approximation from Landau theory, where quasiparticles are the excitations of the strongly interacting system. The system can be specified by obtaining the occupation of quasiparticle states, i.e. the phase-space distribution functions. The

model has been developed by many theorists with different variations[32, 33, 34, 35, 36, 37, 38, 39, 40].

In what follows, we give the formulas that underline dynamics in the pBUU model. In the energy range of interest, the species accounted for are nucleons, pions,  $\Delta$ ,  $N^*$  resonances, and light ( $A \leq 3$ ) clusters. More details on the production of particles can be found in Ref. [41]. The Boltzmann equation for stable particles has the following particular form:

$$\frac{\partial f_X}{\partial t} + \frac{\partial \varepsilon_X}{\partial \vec{p}} \frac{\partial f_X}{\partial \vec{r}} - \frac{\partial \varepsilon_X}{\partial \vec{r}} \frac{\partial f_X}{\partial \vec{p}} = \mathcal{K}_X^<(1 \mp f_X) - \mathcal{K}_X^> f_X. \quad (1.4)$$

The index X above is for different species of particles, and  $\varepsilon_X$  is the single particle energy. The single particle energy and momentum form a covariant vector  $p^\mu = (\varepsilon, \vec{p})$ . The factors  $\mathcal{K}^<$  and  $\mathcal{K}^>$ , are the feeding and removal rates, respectively, for specific momentum states, and the upper and lower signs in their expressions are for fermions and bosons.

The propagation of particles through the nuclear mean field is accounted for on the left hand side of the equation. On the right hand side of the equation, the elastic and inelastic interactions are included, where particles get deflected or absorbed, new particles are formed, etc. Note that in the collision terms, in-medium cross-sections for the nucleons are used. And Pauli blocking effects are taken into account by examining the phase space occupation of the final states.

The rate for removal in 2-body scattering in the equation is written as:

$$\begin{aligned} \mathcal{K}_X^>(\vec{p}_1) &= \frac{g_X}{\gamma_1} \int \frac{d\vec{p}_2}{(2\pi)^3 \gamma_2} \int \frac{d\vec{p}'_1}{(2\pi)^3 \gamma'_1} \int \frac{d\vec{p}'_2}{(2\pi)^3 \gamma'_2} \overline{|M_{2X \rightarrow 2X'}|^2} \\ &\quad \times (2\pi)^3 \delta(\vec{p}_1 + \vec{p}_2 - \vec{p}'_1 - \vec{p}'_2) \\ &\quad \times 2\pi \delta(\varepsilon_1 + \varepsilon_2 - \varepsilon'_1 - \varepsilon'_2) f_2 (1 - f'_1) (1 - f'_2) \\ &= \frac{g_X}{\gamma_1} \int \frac{d\vec{p}_2}{(2\pi)^3 \gamma_2} \int d\Omega^{*'} \frac{p^{*'}{}^2}{4\pi^2 \gamma_1^{*'} \gamma_2^{*'} v_{12}^{*'}} \overline{|M_{2X \rightarrow 2X'}|^2} \\ &\quad \times f_2 (1 - f'_1) (1 - f'_2) \\ &= g_X \int \frac{d\vec{p}_2}{(2\pi)^3} \int d\Omega^{*'} v_{12} \frac{d\sigma}{d\Omega^{*'}} f_2 (1 \mp f'_1) (1 \mp f'_2), \end{aligned} \quad (1.5)$$

where  $g_X$  is the spin degeneracy, and the stars refer to quantities in the center of mass frame. The covariant velocity is  $u^\mu = (\gamma, \gamma \vec{v})$ , and factors are  $\gamma = 1/\sqrt{1 - v^2}$ .  $v_{12}$  is the relative velocity

between the incoming particles, and it is obtained through the following expression:

$$\gamma_1 \gamma_2 v_{12} = \left[ -\frac{[(P \cdot u_2)u_1 - (P \cdot u_1)U_2]^2}{P^2} \right]^{1/2}, \quad (1.6)$$

where  $P$  is the 4-momentum of the 2-body system.

The cross sections in the formulas are

$$\frac{d\sigma}{d\Omega^{*'}} = \frac{p^{*'}^2}{4\pi^2 \gamma_1^* \gamma_2^* v_{12}^* \gamma_1'^* \gamma_2'^* v_{12}'^*} \overline{|M_{2x \rightarrow 2x'}|^2}. \quad (1.7)$$

$|M|^2$  in the cross section formula represents matrix element for scattering amplitude between initial and final states.

In pBUU model, pions are produced through the decay of  $\Delta$  or  $N^*$  resonances. The transport equations for the resonances have a more elaborate form:

$$\frac{\partial f_X A_X}{\partial t} + \frac{\partial \varepsilon_X}{\partial \vec{p}} \frac{\partial f_X A_X}{\partial \vec{r}} - \frac{\partial \varepsilon_X}{\partial \vec{r}} \frac{\partial f_X A_X}{\partial \vec{p}} = \mathcal{K}_X^< (1 \mp f_X) A_X - \mathcal{K}_X^> f_X A_X, \quad (1.8)$$

where  $A_X$  describes the mass distribution of the resonances, with a width of  $\Gamma_X$ :

$$A_X = \frac{\Gamma_X}{(m - m_X)^2 + 1/4\Gamma_X^2}. \quad (1.9)$$

The derivatives on the left hand side of the equation are taken at constant  $m - m_X$ .

In pBUU model, a density functional for the net energy (Hamiltonian) of the system is constructed to achieve energy and momentum conservations. The single-particle energy is related to the net energy  $E$  of the spin-symmetric system with:

$$\varepsilon_X(\vec{p}, \vec{r}, t) = \frac{(2\pi)^3}{g_X} \frac{\delta E}{\delta f_X(\vec{p}, \vec{r}, t)}. \quad (1.10)$$

The resulting single particle energy from Eq. (1.10) is used as the input on the left hand side of Eq. (1.4) and (1.8).

The four components of the net energy are: a volume, surface, isospin-dependent component and a Coulomb contribution:

$$E = \int e d\vec{r} + E_s + E_T + E_{coul}. \quad (1.11)$$

The surface term is

$$E_s = \frac{a_1}{2\rho_0} \int d\vec{r} (\nabla\rho)^2. \quad (1.12)$$

The isospin contribution is

$$E_T = \frac{a_T}{2\rho_0} \int d\vec{r} (\rho_T)^2, \quad (1.13)$$

where the isospin density is calculated through summing over the third isospin component of all particles:

$$\rho_T = \sum_X t_{3X} \rho_X \quad (1.14)$$

And the Coulomb term is

$$E_{coul} = \frac{1}{8\pi\epsilon_0} \int d\vec{r} \int d\vec{r}' \frac{\rho_{ch}(\vec{r})\rho_{ch}(\vec{r}')}{|\vec{r} - \vec{r}'|}. \quad (1.15)$$

To solve the non-linear integral-differential Boltzmann equations, test particle technique is often used to simulate the solution. The non-equilibrium time evolution of the system is simulated through a Monte-Carlo procedure. EOS at zero temperature and the ground state of the system are extrapolated from finite temperature behavior and the non-equilibrium states of the system through energy density functional. In the next chapter, we will discuss in more details the expression for the bulk energy density.

## CHAPTER 2

### CONSTRAINTS ON THE MOMENTUM DEPENDENCE OF NUCLEAR MEAN FIELD

#### 2.1 Momentum dependence of nuclear mean field

In transport theory, both momentum independent and momentum dependent mean field have been used to describe nucleon-nucleus interactions. With the momentum independent mean field, transport models were able to describe sideward flow in HIC. However, a simple density dependence in the mean field is not sufficient to explain the momentum dependence of the elliptic flow observable. Correspondingly a momentum dependent mean field was later implemented into the transport models[42]. On the other hand, a momentum dependence in the nuclear mean field has also been observed in nucleon-nucleus scattering experiments[43]. That is, a nucleon experiences different interaction strength when approaching the nucleus at different momenta. When the relative momentum is zero, the nucleon feels an attractive potential with the magnitude of about 50MeV. This attractive potential results from the sum of an attractive scalar potential and a repulsive vector potential. The mean field becomes less attractive when nucleon approaches at higher momenta, and finally repulsive at  $k > 3\text{-}4\text{fm}^{-1}$ .

The momentum dependence originates from the non-locality of individual nucleon-nucleon interactions[44, 45], from the exchange term in the optical potential, from intrinsic energy dependence in the nucleon-nucleon interactions (or time non-locality), etc. It impacts the dynamics of nucleons in HIC and ultimately the free nucleon emission and fragment production. We can investigate the momentum dependence by studying particle differential yields, collective motion of nucleons and stopping observables.

### 2.1.1 Momentum-dependent mean field in pBUU model

In pBUU model, with a momentum independent mean field, the single-particle energies are parameterized through following expression:

$$\varepsilon_X = \sqrt{p^2 + m_X^2(\rho)} + A_X U_1 + T_{3X} U_T + Z_X \Phi, \quad (2.1)$$

where  $m_X(\rho) = m_X + A_X U(\rho)$ ,  $A_X$  is the baryon number,  $t_{3X}$  is the third component of isospin and  $Z_X$  is the charge number, for particle species X.

We take

$$U(\xi) = \frac{-a\xi + b\xi^\nu}{1 + (\xi/2.5)^{\nu-1}}, \quad (2.2)$$

where  $\xi = \rho/\rho_0$ , and a, b,  $\nu$  are parameters that will be determined by finding the right minimum of EOS in nuclear matter at normal density, and also by requiring the incompressibility to be certain value. We have  $U_1 = -a_1 \nabla^2(\rho/\rho_0)$ ,  $U_T = a_T \rho_T/\rho_0$ , and  $\Phi$  is the Coulomb potential.  $\rho_T$  is the density of the third component of isospin. The coefficients  $a_1$  and  $a_T$  are the strength of the gradient and isospin interactions. Note that in pBUU, the bulk of mean field  $U(\rho)$  only acts on baryons. Pions are infrequent in the intermediate energy HIC, therefore are assumed to only be subjected to isospin dependent part of the mean field interaction.

In the case of momentum dependent mean field, the single particle energy is parameterized in a different form:

$$\varepsilon_X = m_X + \int_0^p dp' v_X^* + A_X \left[ \rho \left\langle \int_0^{p_1} dp' \frac{\partial v}{\partial \rho} + U(\rho) \right\rangle \right] + A_X U_1 + T_{3X} U_T + Z_X \Phi. \quad (2.3)$$

Here, the momentum dependence has been implemented for symmetric nuclear matter, through the parametrization of local particle velocity, in the following form[29]:

$$v_X^*(p, \xi) = \frac{p}{\sqrt{p^2 + m_X^2 / \left(1 + C \frac{m_N}{m_X} \frac{A_X \xi}{(1 + \lambda p^2/m_X^2)}\right)^2}}. \quad (2.4)$$

The two free parameters C and  $\lambda$  are also to be fixed in calculating the minimum of the EOS.

Stable particles contribute to the total density through the following expression:

$$\rho_X = g_X \int \frac{d\vec{P}}{(2\pi)^3} \frac{m_{X0}}{e(\vec{P})} f_X(\vec{P}), \quad (2.5)$$

and the density associated with resonances are

$$\rho_X = g_X \int \frac{d\vec{P}}{(2\pi)^3} \int \frac{dE}{2\pi} \frac{m_{X0}}{m} f_X(\vec{p}, E) A_X. \quad (2.6)$$

When particle travels through the medium and is affected by a momentum-dependent mean field, it appears to have a different mass than when moving in free space. This 'apparent mass', relating momentum and velocity, is called the effective mass, defined by:

$$m^* = p/v, \quad (2.7)$$

where  $p = |\vec{p}|$ , and  $v = |\vec{v}|$ . The effective mass is a convenient way to represent the momentum dependence of the mean field and, in compare different MFs, it is common to specify the effective mass at Fermi momentum in cold normal matter.

With the above parametrization of the momentum dependent mean field, pBUU has been successful in describing various experimental data[23, 46]. However the model has not been tested against measurements of pion multiplicity at incident energies near NN pion production threshold (e.g. 400A MeV). In the following, we examine the momentum dependence on the pion production and pion spectra in central HIC.

## 2.2 Pion observables

Within pBUU model, pions are produced through the decay of  $\Delta$  or  $N^*$  resonances in intermediate energy HIC (100A MeV - 2A GeV). The charge of the produced pions follows from representing  $\Delta$  isospin as a superposition of nucleon and pion isospin states.

$$n + n \leftrightarrow n + \Delta/N^*, \quad (2.8)$$

$$\Delta/N^* \leftrightarrow n + \pi. \quad (2.9)$$

To remind readers, we show here again the transport equations for  $\Delta$  or  $N^*$  resonances:

$$\frac{\partial f_X A_X}{\partial t} + \frac{\partial \varepsilon_X}{\partial \vec{p}} \frac{\partial f_X A_X}{\partial \vec{r}} - \frac{\partial \varepsilon_X}{\partial \vec{r}} \frac{\partial f_X A_X}{\partial \vec{p}} = \mathcal{K}_X^< (1 \mp f_X) A_X - \mathcal{K}_X^> f_X A_X, \quad (2.10)$$

where subscript X represent different particle species, and  $A_X$  describes the mass distribution of the resonances, with a width of  $\Gamma_X$ :

$$A_X = \frac{\Gamma_X}{(m - m_X)^2 + 1/4\Gamma_X^2}. \quad (2.11)$$

In the above,  $m_X$  is the vacuum mass for resonance particles,  $m_\Delta=1232 \text{ MeV}/c^2$ ,  $m_{N^*}=1440 \text{ MeV}/c^2$ .

The production and absorption of pions are described through decay of the resonances and a sequence of inverse processes. Fig. 2.1 shows net pion multiplicity obtained when using the momentum-independent and momentum-dependent mean field in pBUU, adjusted previously to different nuclear characteristics and data[29]. Specifically Fig. 2.1(a) shows calculations done with momentum-independent mean field and Fig. 2.1(b) with the previous flow-optimized momentum-dependent mean field. The data represented in the figure are from the FOPI measurements of Au+Au central collisions (impact parameter  $b < 2\text{fm}$ ) at 400A MeV, 800A MeV and 1.5A GeV[1]. As can be seen, pBUU with momentum-independent mean field overestimates, by a factor of two, the measured multiplicities at all energies. With momentum-dependent mean field, the calculations are consistent with data at the two higher energies, but at 400A MeV, the predicted yields are only about half of those measured. The results of the calculations suggest that some weakening of the momentum dependence is required in order to arrive at an agreement between the pBUU results and FOPI data at the lowest of the beam energies. Other than momentum dependence, we explored potential impact of in-medium changes in the  $\pi$  and  $\Delta$  production rates[23, 29] consistent with detailed balance, but we found the impact of such changes, within plausible range, to be negligible on the final yields. Further on, the parametrization used on the right panel of Fig. 2.1 will be referred to as  $v_2$ -optimized MF.

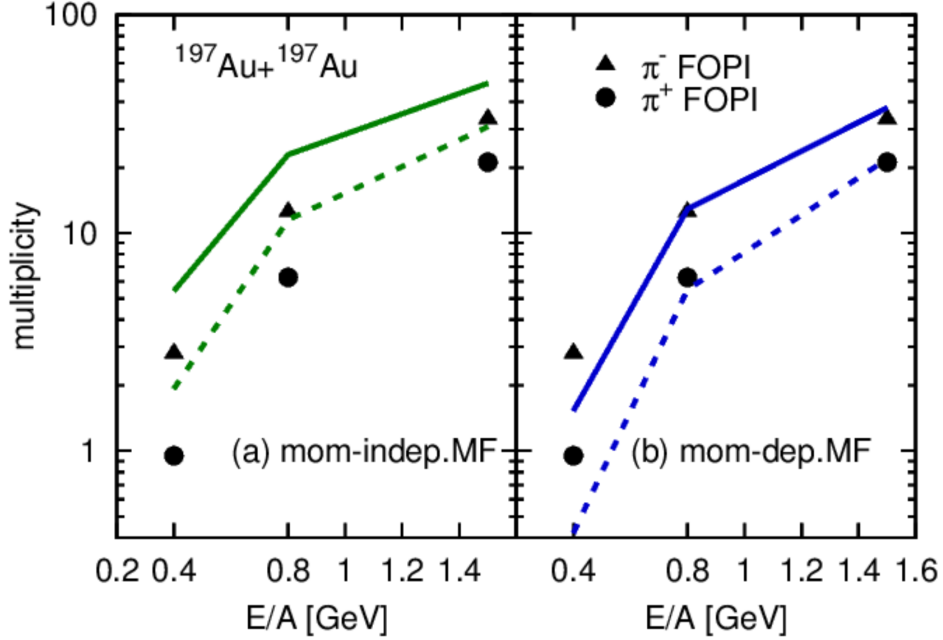


Figure 2.1 Pion multiplicity in central Au+Au collisions. Symbols represent data of the FOPI Collaboration [1]. The lines represent pBUU calculations when following either the momentum-independent MF (left panel) or the past flow-optimized momentum-dependent MF (right panel). Solid lines are predictions for  $\pi^-$ , and dashed lines are predictions for  $\pi^+$ . The experimental error bars are about the size of symbols.

	previous parameteriza- tion ( $v_2$ -optimized MF)	new parameterization ( $N_\pi$ -adjusted MF)
C	0.643	0.300
$\lambda [1/c^2]$	0.948	0.400
a [MeV]	203.92	173.71
b [MeV]	65.18	68.23
$\nu$	1.4838	1.6541
K [MeV]	210	230
$m^*/m$	0.7	0.75

Table 2.1 Parameters used in the previous and new momentum dependent MFs. In either case, the parameters were adjusted to yield sensible nuclear incompressibility K and nucleon effective mass  $m^*$ .

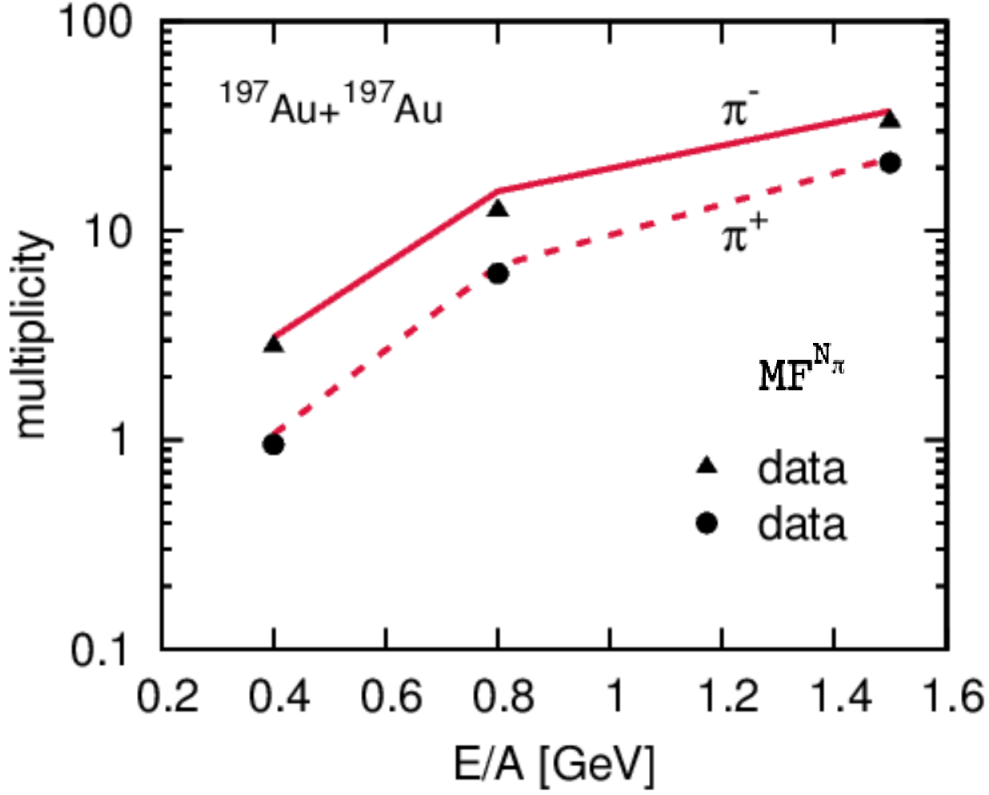


Figure 2.2 Pion multiplicity in central Au+Au collisions, as a function of beam energy. Symbols represent data of the FOPI collaboration[1], , while lines represent the pBUU calculations with the  $N_\pi$ -adjusted momentum-dependent MF. The experimental error bars are about the size of symbols.

In the context of the discrepancy, we explored different possibilities for the momentum dependence of the mean field by modifying the underlying parametrization for the local particle velocity. We tested different density-dependencies of momentum-dependencies for the mean field, by replacing the factor in Eq.(2.4), linear in  $\xi$ , by different functions of  $\xi$  that reduced to 1 at saturation density, i.e. at  $\xi \equiv \frac{\rho}{\rho_0} = 1$ . However, we found the sensitivity of pion yields to that replacement to be too meager to eliminate the discrepancy between the measured and calculated pion yields. On the other hand, we found that a mere adjustment of the parameter values in the original parametrization of Eq.(2.4) could reduce substantially the discrepancy between the calculated and measured net pion yields, without overly compromising the description of measured baryonic flow

by the model.

In what follows, we refer to the momentum-dependent mean field with the new parameters as  $N_\pi$ -adjusted MF. Parameter values for the  $N_\pi$ -adjusted and previous  $v_2$ -optimized MF are listed in Table 2.1. In the table, nucleon effective mass is used conventionally to represent the momentum-dependent mean field;  $C$  and  $\lambda$  are the parameters that dictate the momentum dependence. The net pion yields for the  $N_\pi$ -adjusted MF are displayed, together with the data, in Fig. 2.2.

### 2.3 Optical potential comparison

Properties of nuclear matter and nucleon optical potentials have been also a focus for microscopic calculations starting with elementary nucleon-nucleon interactions. Various theories such as variational method of Friedman and Pandharipande[47] and Bruckner approach[48, 49, 50, 51, 52], have been developed to explain, in particular, the microscopic origin of the momentum dependence in nuclear mean field. In data analysis, the momentum dependence has been reflected in the need to readjust the optical potential needed to describe nucleon-nucleus scattering at different incident energies. In testing the characteristics of the  $N_\pi$ -adjusted MF, we examine the momentum dependence of optical potentials in zero-temperature matter. For the optical potential  $U^{opt}(p)$ , we employ, in the relativistic context, the following operational definition:

$$U^{opt}(\rho, p) = \varepsilon(\rho, p) - \sqrt{p^2 + m^2}. \quad (2.12)$$

In the equation,  $\varepsilon(p)$  is the single particle energy corresponding to momentum  $p$ . Other definitions have been proposed in the literature. Once adopted, they just need to be used consistently.

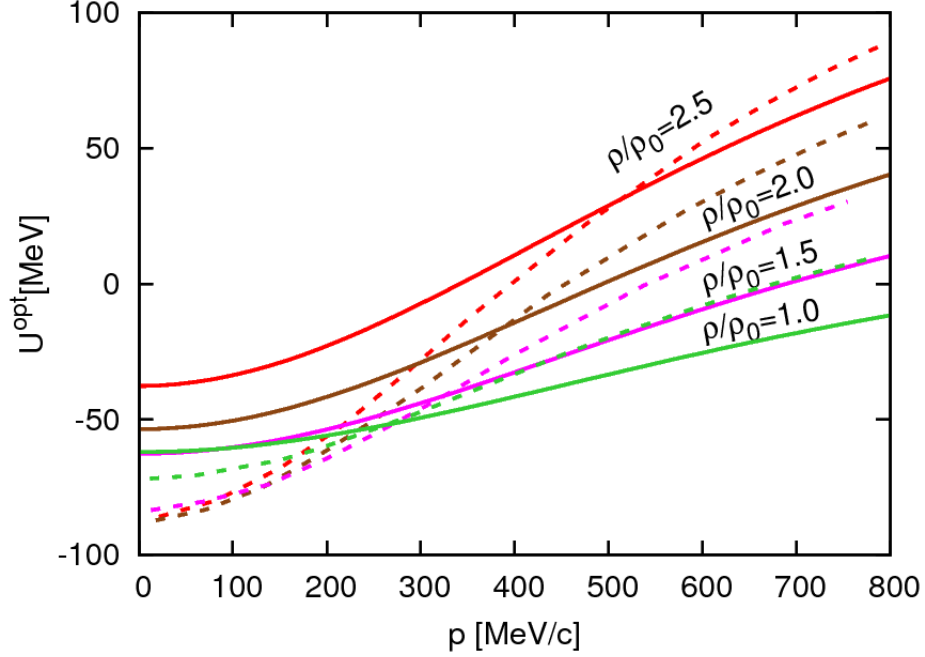


Figure 2.3 Optical potential in nuclear matter at different indicated densities, as a function of momentum. Dashed and solid lines represent, respectively, the  $v_2$ -optimized and  $N_\pi$ -adjusted MFs.

In Fig. 2.3 we plot the optical potentials for our two parametrizations, as a function of momentum, with different lines representing different indicated densities. The dashed and solid lines represent, respectively, optical potentials from the  $v_2$ -optimized and  $N_\pi$ -adjusted MFs. The momentum dependence in  $N_\pi$ -adjusted MF is indeed softened, consistent with the expectation developed on the basis of Fig. 2.3.

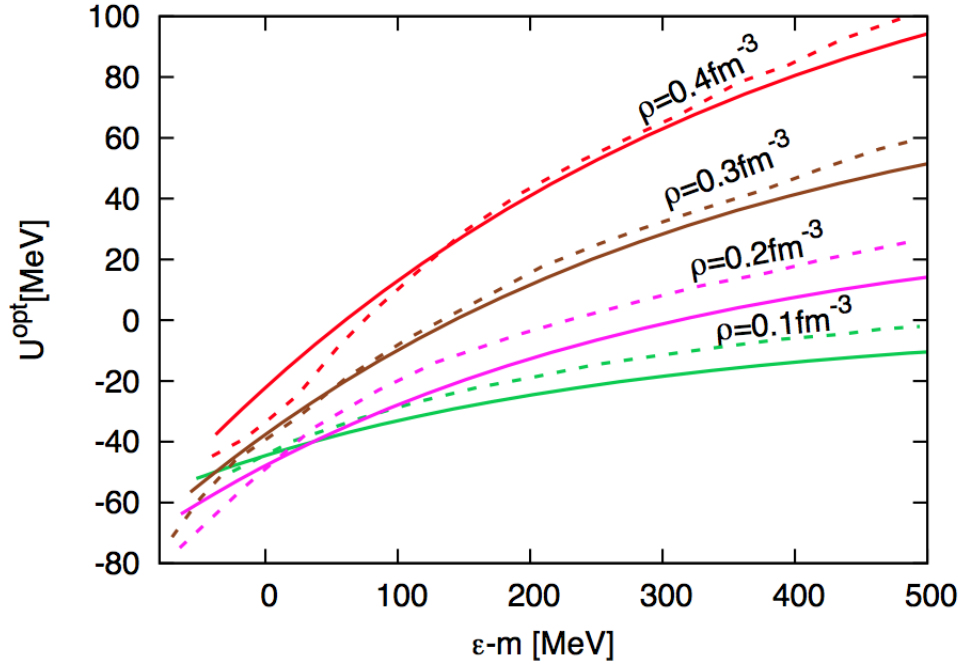


Figure 2.4 Optical potential in nuclear matter at different indicated densities, as a function of nucleon energy. Dashed and solid lines represent, respectively, UV14+UVII variational calculations and our  $N_\pi$ -adjusted MF.

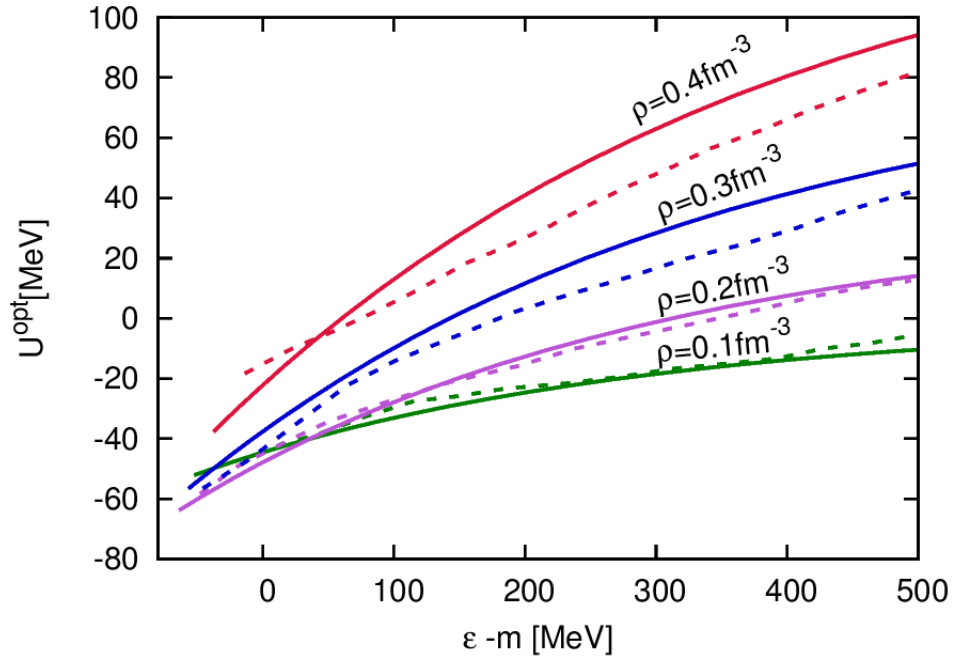


Figure 2.5 Optical potential in nuclear matter at different indicated densities, as a function of nucleon energy. Dashed and solid lines represent, respectively, AV14+UVII variational calculations and our  $N_\pi$ -adjusted MF.

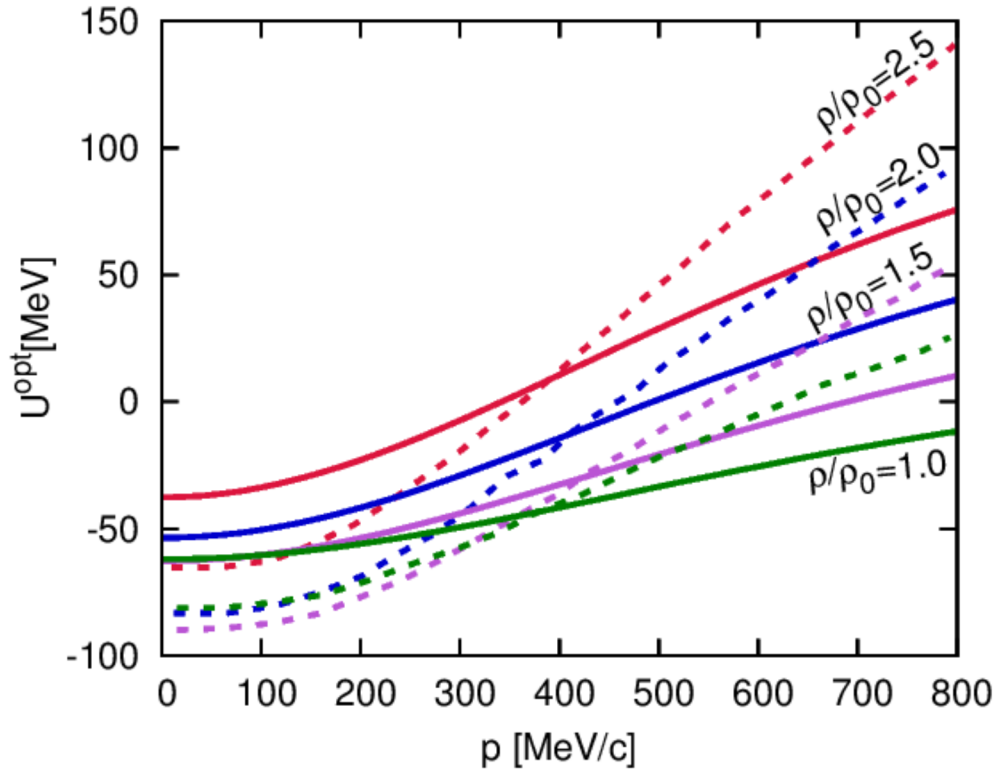


Figure 2.6 Optical potential in nuclear matter at different indicated densities, as a function of nucleon momentum. Dashed and solid lines represent, respectively, Dirac-Brueckner-Hartree-Fock calculations and our  $N_\pi$ -adjusted MF.

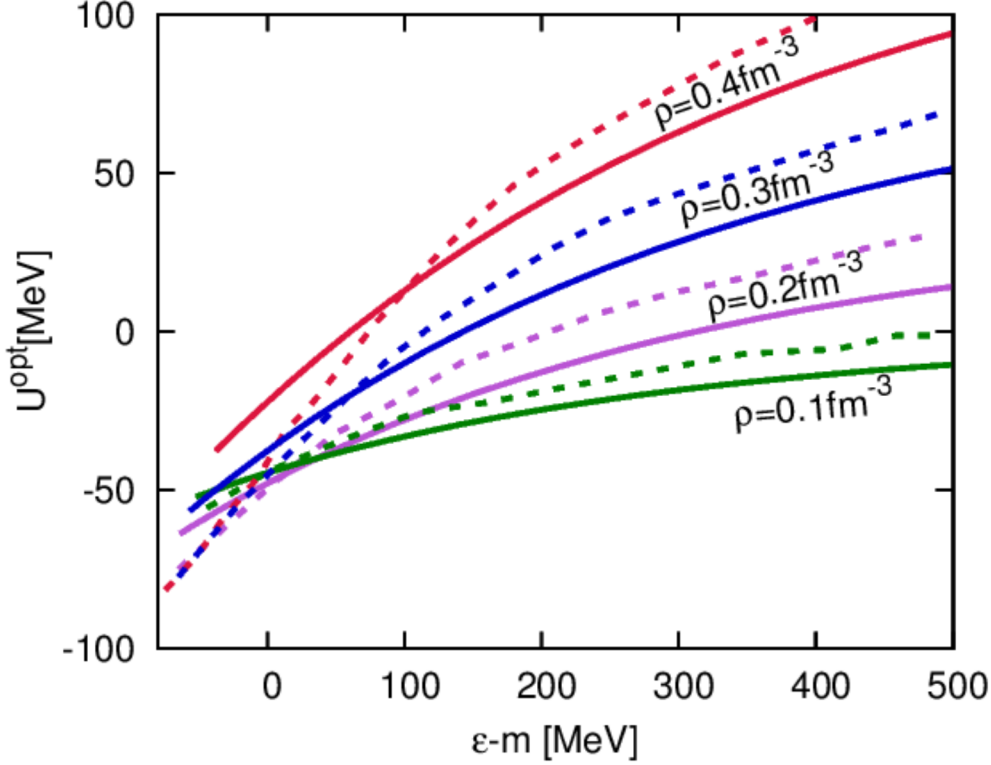


Figure 2.7 Optical potential in nuclear matter at different indicated densities, as a function of nucleon energy. Dashed and solid lines represent, respectively, UV14+TNI variational calculations and our  $N_\pi$ -adjusted MF.

In [29], the momentum dependence of the optical potential from  $v_2$ -optimized mean field was compared to that found for potentials from microscopic calculations including those relying on the Urbana V14 two-body interaction combined with model VII three-body interaction, i.e. UV14+UVII[47], AV14+UVII[47], as well as DBHF[50, 52], BBG and UV14+TNI[53, 54]. The  $N_\pi$ -adjusted MF produces optical potentials that are closest in the form and values to UV14+UVII [47], with the respective comparison illustrated in Fig. 2.4. Similar comparisons to the other microscopic calculations can be found in figures 2.5- 2.7. In Fig. 2.4, we compare the single-particle energy,  $\varepsilon(p, \rho) - m$ , to UV14. The momentum dependence in this representation is implicit.

## 2.4 Elliptic flow

Flow signals the multiple interactions that particles experience throughout the reaction. A larger number of interactions leads the system closer to thermal equilibrium. Elliptic flow is a measure of anisotropy of particle emission in HIC in azimuthal directions around the beam-line. In the past, anisotropies of collective flow and, in particular, the elliptic flow, were used to test the characteristics of MF momentum-dependence in collisions[55, 56]. .

Fig. 2.8 shows the basic geometry for a HIC[57]. The projectile beam is directed along z axis, x axis is parallel to the impact parameter direction, x-z plane is defined as the reaction plane. The y axis is perpendicular to the reaction plane, or points out of the reaction plane. When the impact parameter b is not zero, there will be an almond shaped region formed where the two nuclei overlap with each other when passing by and where violent interactions take place. This anisotropy in the space will translate to the anisotropy in momentum space for emitted particles.

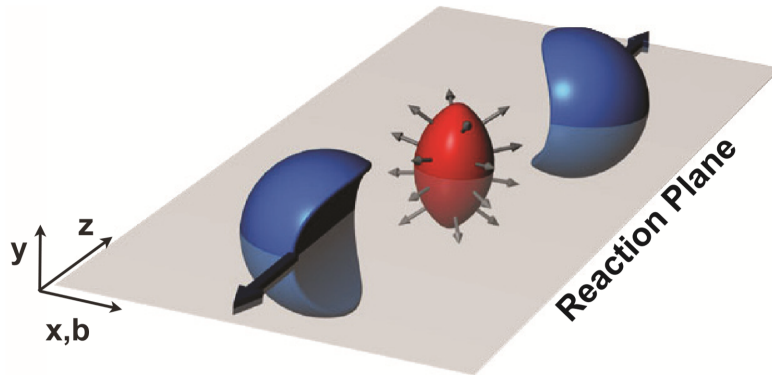


Figure 2.8 Schematic drawing of the geometry in a HIC. The beam line is along z axis, x axis is parallel to the impact parameter direction. x-z plane is defined as the reaction plane, and y axis is perpendicular to the reaction plane.

In experiments, the anisotropies can be observed through studying how correlated is particle

emission in azimuthal directions. A schematic description of the particle emission process is shown in figure 2.9. Particles within the almond shaped region are called participants, and the rest of the particles are spectators, as they mostly continue along the beam axis, without experiencing collisions with particles from the opposing nucleus.

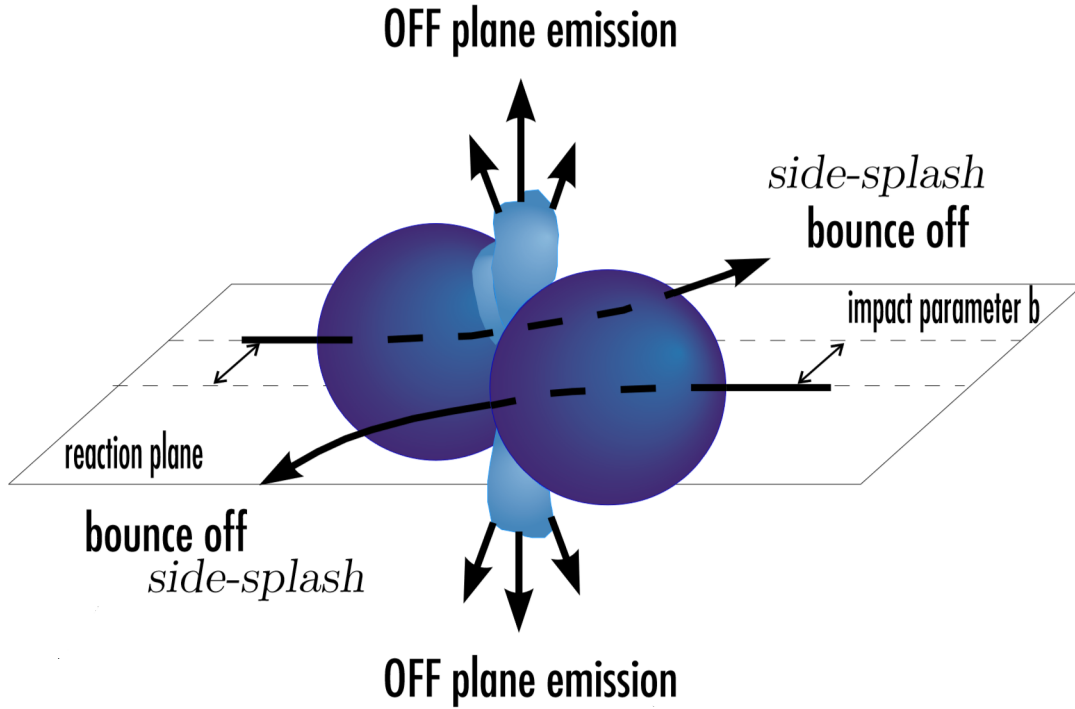


Figure 2.9 Particle emission processes are shown with respect to the reaction plane. The blockage of spectator particles leads to the out-of-plane emission in the early stage of the reactions.

A convenient way of quantifying the emission anisotropies in the theory and experiment is to use a Fourier expansion of the particle distributions with respect to azimuthal angle:

$$\frac{dN}{d\phi} \sim [1 + 2v_1 \cos(\phi) + 2v_2 \cos(2\phi) + \dots], \quad (2.13)$$

where  $v_1$  and  $v_2$  are known as coefficients of directed flow and elliptic flow, respectively. The value of directed flow and elliptic flow coefficients are obtained using the following expressions:

$$v_1 = \langle \cos(\phi) \rangle = \left\langle \frac{p_x}{p_y} \right\rangle, \quad (2.14)$$

$$v_2 = \langle \cos(2\phi) \rangle = \left\langle \frac{p_x^2 - p_y^2}{p_x^2 + p_y^2} \right\rangle. \quad (2.15)$$

Most commonly, the elliptic flow  $v_2$  is studied at midrapidity, i.e.  $y=0$ . Non-relativistically, the rapidity  $y$  reduces to particle speed in units of  $c$ , but is more convenient in relativistic context. The rapidity is defined with

$$y = \frac{1}{2} \ln \frac{E + p_z c}{E - p_z c}, \quad (2.16)$$

where  $E$  and  $p_x$  are in the system c.m. The coefficient  $v_2 > 0$  corresponds to in plane particle emission and  $v_2 < 0$  corresponds to out of reaction plane emission.

Obviously when more demands are placed on the nuclear mean field, such as the proper description of total pion yields, the description of the measured elliptic flow cannot generally stay as good as that achievable without those additional constraints. Fig. 2.10 shows the out-of to in-reaction-plane ratio,  $R = \frac{1-v_2}{1+v_2}$ , for protons emitted at midrapidity from mid-peripheral Bi+Bi collisions at 400A MeV, as a function of proton transverse momentum. The stronger the elliptic flow, the larger the deviation of  $R$  from 1. The filled triangles in Fig. 2.10 represent the data of the KaoS collaboration[2], while the dashed and solid lines represent, respectively, the pBUU calculations with  $v_2$ -optimized and  $N_\pi$ -adjusted MF (denoted as MF $^{v_2}$  and MF $^{N_\pi}$ , respectively, in the figures). The two calculations describe about equally well the KaoS data at intermediate momenta, but the  $v_2$ -optimized MF is far superior at high momenta.

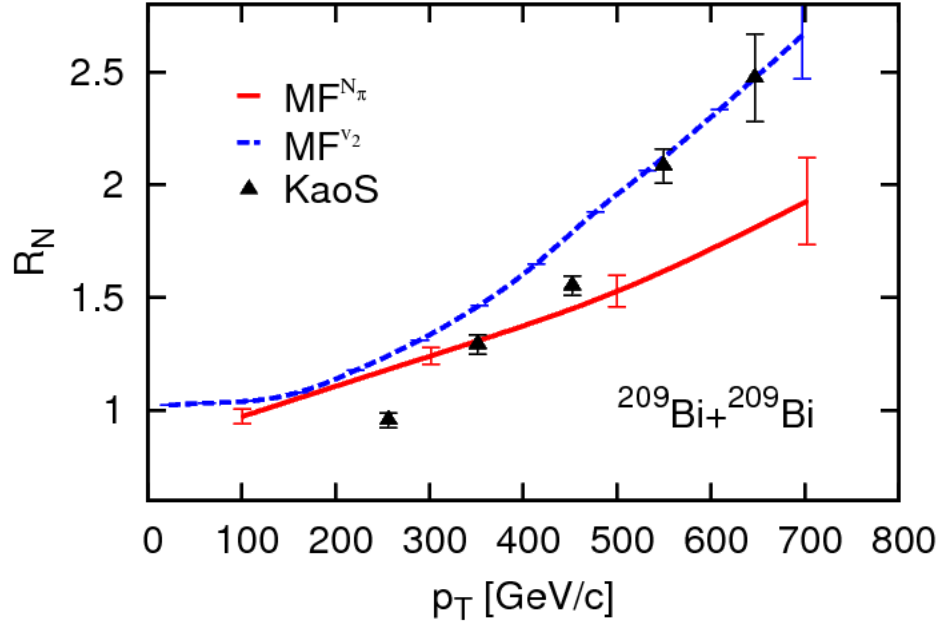


Figure 2.10 Ratio of out of reaction plane to in-plane proton yields, as a function of transverse momentum. Symbols represent data from the measurements of the KaoS Collaboration of mid-peripheral Bi+Bi collisions at the beam energy of 400A MeV ( $b \simeq 8.7\text{fm}$ ) [2]. Solid line represents pBUU calculations with the  $N_\pi$ -adjusted momentum-dependent MF and dashed line represents calculations with  $v_2$ -optimized momentum-dependent MF. The indicated theoretical errors are statistical, associated with the Monte-Carlo sampling in the transport calculations.

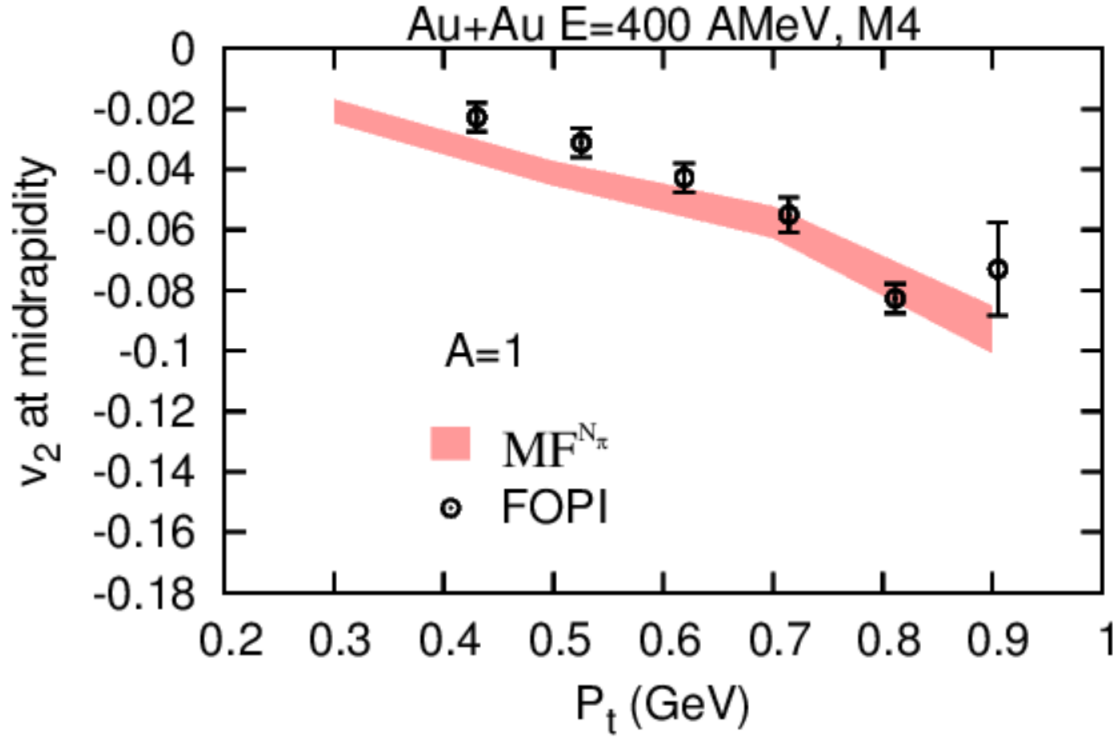


Figure 2.11 Elliptic flow of particle mass  $A=1$  particles, as a function of transverse momentum. Symbols represent data from the measurements of the FOPI Collaboration of mid-peripheral Au+Au collisions at the beam energy of  $400A$  MeV ( $b \sim 2.0 - 5.3$ fm). The shaded region represents pBUU calculations with the  $N_\pi$ -adjusted momentum-dependent MF. The indicated theoretical errors are statistical, associated with the Monte-Carlo sampling in the transport calculations.

Further comparisons were made with more recent experimental data from FOPI collaboration displayed in Fig. 2.11-12[58]. Elliptic flow is plotted there against the transverse momentum of the particles for Au+Au collisions at energies  $400A$  MeV and  $600A$  MeV. In the experiment, the centrality of the nuclear reactions is determined through multiplicity measurements of charged particles, and M4 in the figures corresponds to the impact parameter within the range of 2.0-5.3fm. The transverse momentum is obtained from  $p_t = \sqrt{p_x^2 + p_y^2}$ . It is apparent that the pBUU simulations fail to reproduce the experimental data for elliptic flow at  $600A$  MeV. The difficulty in the

simultaneous description of high-momentum  $v_2$  and near-threshold pion yields shows that changing the momentum dependence in such a simple fashion is not enough to describe various observables. One possibility is e.g. the lack of anisotropy in the momentum dependence, for anisotropic momentum distributions  $f$ , when employing Eq. (2.4)-(2.6). While our implementation Eq. (2.4)-(2.6) of the mean field momentum dependence, without anisotropy, allows in practice for a higher precision of calculations than other mean field parametrizations [59], that implementation may turn out to be a handicap here. We already undertook steps, cf. the work of Simon and Danielewicz [59], towards implementing anisotropy without compromising calculational precision or speed. However, in chapter 3, we will show another resolution, which instead of only focusing on the momentum dependence of the mean field, we investigate the competing effects of the momentum and the density dependence. We are able to resolve the puzzle by studying a wider range of the momentum and density dependence of the mean field, and using pion and flow observable to constrain the EOS.

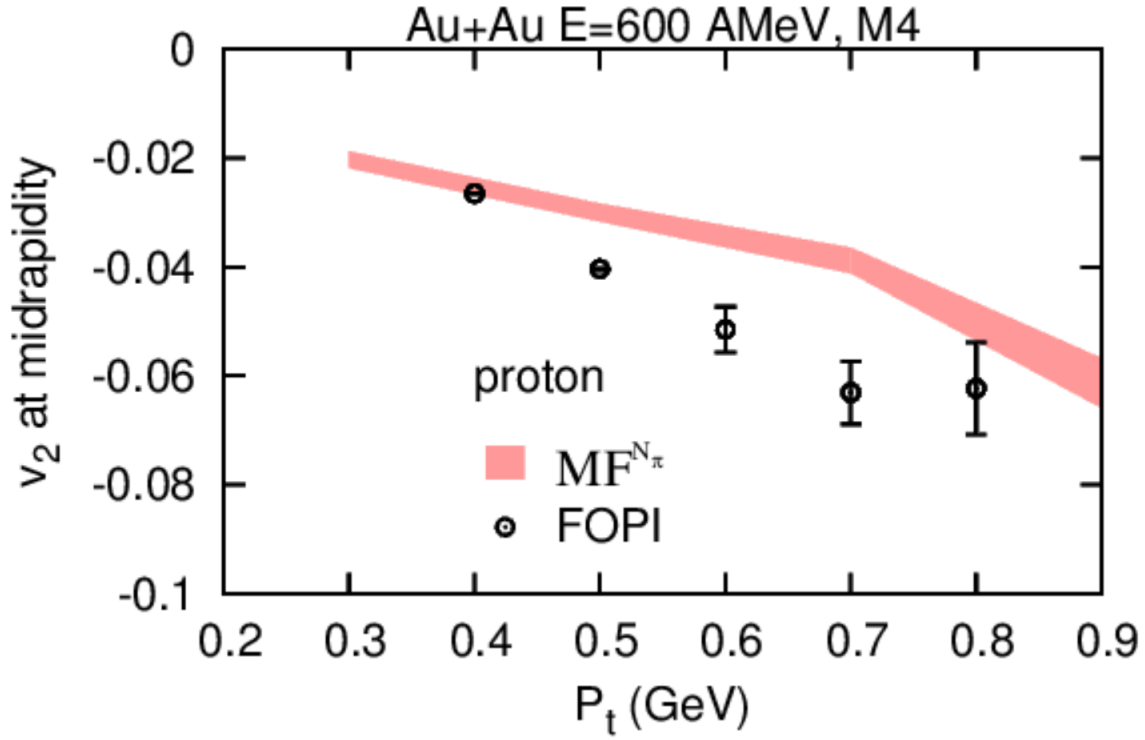


Figure 2.12 Elliptic flow of proton, as a function of transverse momentum. Symbols represent data from the measurements of the FOPI Collaboration of mid-peripheral Au+Au collisions at the beam energy of 600A MeV ( $b \sim 2.0 - 5.3$ fm). The shaded region represents pBUU calculations with the  $N_\pi$ -adjusted momentum-dependent MF. The indicated theoretical errors are statistical, associated with the Monte-Carlo sampling in the transport calculations.

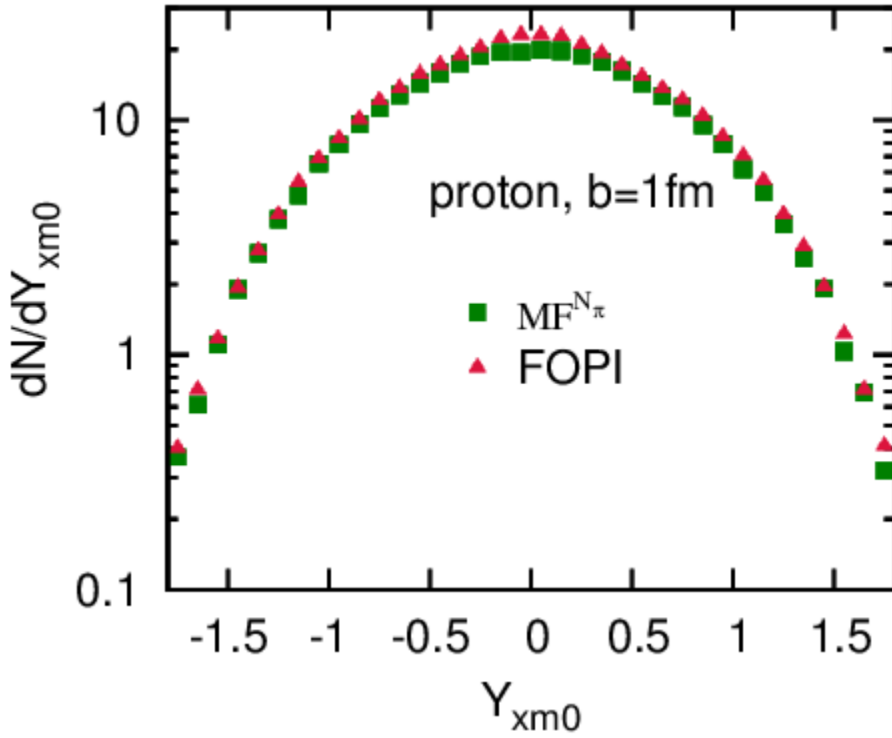


Figure 2.13 Transverse rapidity distribution of protons. Rapidity values  $y_x$  are scaled with the projectile rapidity in the center-of-mass frame:  $y_{x0} = y_x/y_p$ . The transverse rapidity distribution with respect to  $y_{xm0}$  is obtained with a midrapidity cut of  $|y_{z0}| < 0.5$ . Triangles represent data from the measurements of the FOPI Collaboration of central Au+Au collisions at the beam energy of 400A MeV ( $b=1\text{fm}$ ). The squares represent pBUU calculations with the  $N_{\pi}$ -adjusted momentum-dependent MF.

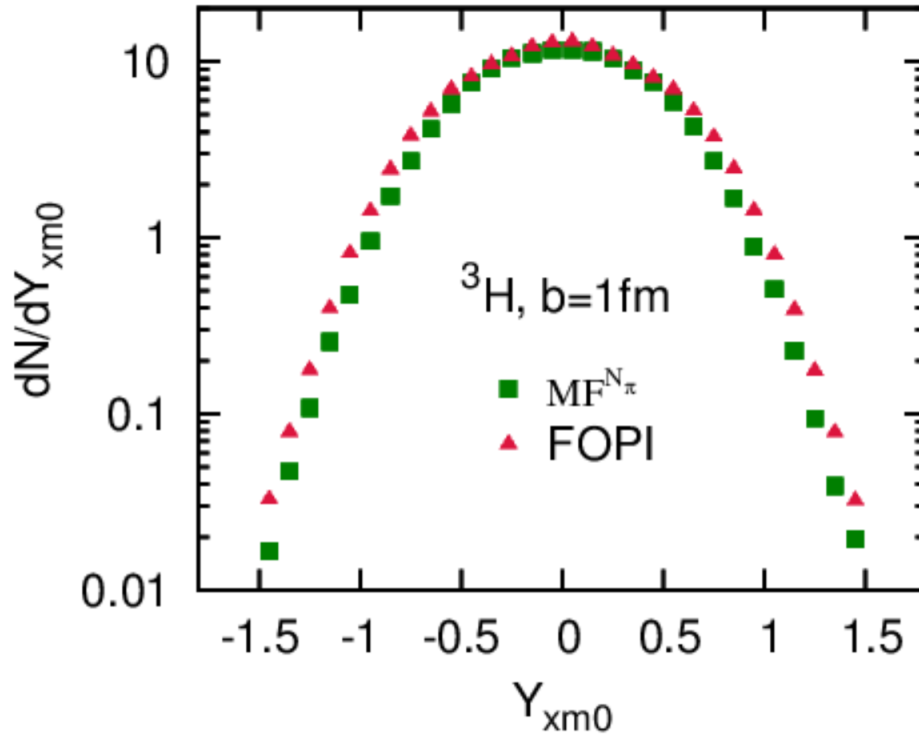


Figure 2.14 Transverse rapidity distribution of tritons. Rapidity values  $y_x$  are scaled with the projectile rapidity in the center-of-mass frame:  $y_{x0} = y_x/y_p$ . The transverse rapidity distribution with respect to  $y_{xm0}$  is obtained with a midrapidity cut of  $|y_{z0}| < 0.5$ . Triangles represent data from the measurements of the FOPI Collaboration of central Au+Au collisions at the beam energy of 400A MeV ( $b=1\text{fm}$ ). The squares represent pBUU calculations with the  $N_\pi$ -adjusted momentum-dependent MF.

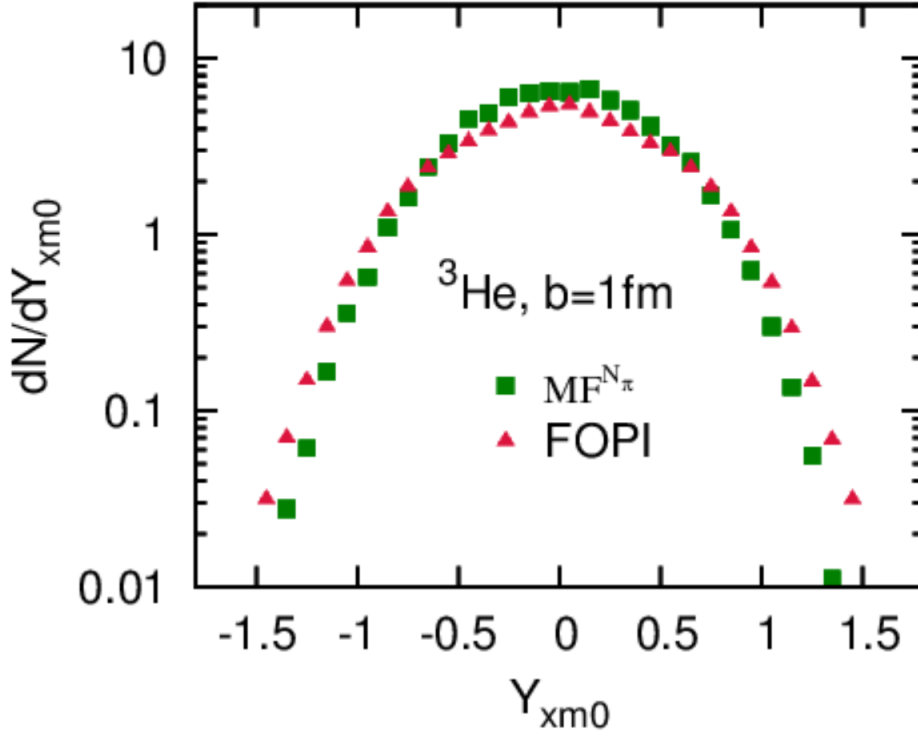


Figure 2.15 Transverse rapidity distribution of Helium 3. Rapidity values  $y_x$  are scaled with the projectile rapidity in the center-of-mass frame:  $y_{x0} = y_x/y_p$ . The transverse rapidity distribution with respect to  $y_{xm0}$  is obtained with a midrapidity cut of  $|y_{z0}| < 0.5$ . Triangles represent data from the measurements of the FOPI Collaboration of central Au+Au collisions at the beam energy of 400A MeV ( $b=1\text{fm}$ ). The squares represent pBUU calculations with the  $N_{\pi}$ -adjusted momentum-dependent MF.

As a complement to elliptic flow, we have examined the transverse rapidity distributions of different particles. Calculations were carried out for Au+Au central collision at 400A MeV, with the  $N_{\pi}$ -adjusted momentum-dependent MF. Figs. 2.13-2.15 show the transverse rapidity distribution for proton, triton and Helium 3, respectively. Triangles represent measurements from FOPI Collaboration[1], and squares represent theoretical predictions. Rapidity values  $y_x$  and  $y_z$  are scaled with the projectile rapidity in the center-of-mass frame:  $y_{x0} = y_x/y_p, y_{z0} = y_z/y_p$ , where subscript

p stands for projectile. The transverse rapidity distribution with respect to  $y_{xm0}$  are obtained with a midrapidity cut of  $|y_{z0}| < 0.5$ . We found a good agreement between pBUU calculations and data on transverse rapidity distributions for all the particles.

## 2.5 Conclusions

In this chapter, we revisited the momentum-dependence of the nuclear mean field. Previously, the mean field implemented in pBUU model has been tested against flow data only. We found here that the momentum dependence deduced from flow alone failed to describe the pion multiplicities near pion production threshold energies. We modified the momentum dependence to resolve the discrepancy between theoretical prediction and experimental measurements. The improvement in pion multiplicities, however, gave rise to a significantly inferior description of elliptic flow, and inspired further study of both momentum and density dependence of the nuclear mean field presented in the next chapter.

## CHAPTER 3

### CONSTRAINTS ON NUCLEAR INCOMPRESSIBILITY

#### 3.1 Introduction

Equation of state (EOS) of infinite symmetric nuclear matter, typically considered at zero temperature and expressed in terms of energy per nucleon as a function of density,  $E(\rho)$ , is one of the most important characteristics of nuclear matter. As the energy at the saturation density reaches a local minimum, the first derivative there is zero:  $\frac{dE}{d\rho}|_{\rho_0} = 0$ . In consequence, in order to describe the equation of state when moving away from saturation point, information on the curvature of  $E(\rho)$  is desired.

Expanding the energy around saturation density, one gets

$$E(\rho) = E(\rho_0) + \frac{1}{18}K_\infty\left(\frac{\rho - \rho_0}{\rho_0}\right)^2 + \dots \quad (3.1)$$

Here, the incompressibility coefficient  $K_\infty$  of symmetric nuclear matter is defined as the scaled curvature of  $\frac{E}{A}(\rho)$ :

$$K_\infty = 9\rho^2 \frac{\partial^2 E/A}{\partial \rho^2} \Big|_{\rho_0}. \quad (3.2)$$

HIC dynamics, giant collective oscillations of nuclei and supernovae explosions are all sensitive, directly or indirectly, to the nuclear incompressibility. A comparison of data on isoscalar giant monopole and dipole resonances to nonrelativistic random-phase-approximation calculations suggested the incompressibility  $K$  value in the range of 220-233MeV[60, 61, 62] while comparisons to relativistic calculations produced a stiffer EOS with  $K$  value in the range 250-270MeV[8]. The summary conclusion from those comparisons, given some limitations in both types of calculations, was of value for  $K = 240 \pm 20$ MeV [63].

However, a recent reanalysis of comparisons to giant monopole resonance energies shifted the range  $K_\infty$  to  $250 < K_\infty < 315 \text{ MeV}$  [64]. With this, the question about the value of  $K_\infty$  remains somewhat open. Interestingly, if one forced a parabolic fit to energy to pass through zero energy at zero density, the resulting incompressibility would have been  $K_\infty = 18 \times 16 \text{ MeV} = 288 \text{ MeV}$ . Later in this chapter we arrive at constraints on nuclear incompressibility based on analysis of elliptic flow in heavy-ion collisions.

### 3.2 Incompressibility and isoscalar Giant Monopole Resonance

The compressional mode that is most directly related to the nuclear incompressibility is the isoscalar giant monopole resonance (IGMR). The first observation of IGMR was made in 1970s, establishing the centroid excitation energy of  $^{208}\text{Pb}$  at 13.7 MeV [65]. It was subsequently found that for heavy nuclei, such as Sn and Pb, the IGMR strength is peaked around  $80A^{-1/3} \text{ MeV}$  [66]. Incompressibility for a specific nucleus can be deduced from the IGMR energy following the relation [66, 67]:

$$E_{IGMR} = \sqrt{\frac{\hbar^2 K_A}{m \langle r^2 \rangle}}. \quad (3.3)$$

Analogous to the energy for a finite nucleus, the incompressibility  $K_A$  may be represented in terms of four main contributions: the volume term  $K_\infty$ , the surface term  $K_{surf}$ , the symmetry term  $K_{sym}$  and the Coulomb term  $K_{Coul}$  [68]:

$$K_A = K_\infty + K_{surf}A^{-1/3} + K_{sym}(N - Z)^2/A^2 + K_{Coul}Z^2A^{-4/3}, \quad (3.4)$$

One can use the above relation to arrive at the incompressibility for infinite nuclear matter. In the following context, we omit the subscript  $\infty$  in  $K_\infty$  when there is no ambiguity.

### 3.3 Elliptic flow

In intermediate-energy HIC, mid-rapidity particles are preferentially emitted out-of rather than in the reaction plane. This is termed squeeze-out and is tied to negative elliptic flow. The magni-

tude of that elliptic flow tests the momentum dependence of MF acting on the particles in the collision as was demonstrated in the previous chapter. Besides, it is also an important observable probing the density dependence of the nuclear MF, which is tied to nuclear incompressibility. Figs. 3.1-3.3 demonstrate the effects of emphasized momentum-dependence and density-dependence of nuclear mean field on elliptic flow  $v_2$  at midrapidity. The midrapidity window is chosen as  $|y^{(0)}| < 0.1$ , where the particle rapidity is scaled with projectile rapidity at center of mass frame:  $y^{(0)} = (y/y_p)^{cm}$ .  $v_2$  is plotted there against the scaled transverse momentum per nucleon  $p_t^{(0)} = (p_t/A)/(p_p^{cm}/A_p)$ , where  $p_t = \sqrt{p_x^2 + p_y^2}$ . Data used for reference, in the figures, are from the FOPI measurements of the mid-peripheral Au+Au collisions at 400A MeV [58], with the impact parameters ranging from 2.0 to 5.3fm. As the detection system does not provide isotope determination, the cluster mass number was assumed to be  $A=2Z$  for all elements heavier than H. Theoretical results were calculated with either  $v_2$ -optimized MF or momentum independent MF, and the corresponding incompressibility of, either 210MeV or 380 MeV. In particular, the  $v_2$ -optimized MF has been optimized to the impact parameter dependence of directed flow [69, 42] and to momentum dependence of elliptic flow [29]. The two mean fields [70] yield about the same directed flow in semicentral collisions, when that flow is integrated over transverse momenta. However, elliptic flow comparisons of simulation and data for  $A=1-3$  particles, in Figs. 3.1-3.3 shows a clear preference for the  $v_2$ -optimized MF, with a lower incompressibility in pBUU model, than momentum-independent MF with  $K=380$  MeV. Still, the figures demonstrate that a strong density dependence in EOS and MF may have a significant impact on the elliptic flow. Even with no momentum dependence in MF, the stiff EOS yields elliptic flow about twice as large in magnitude as the soft EOS.

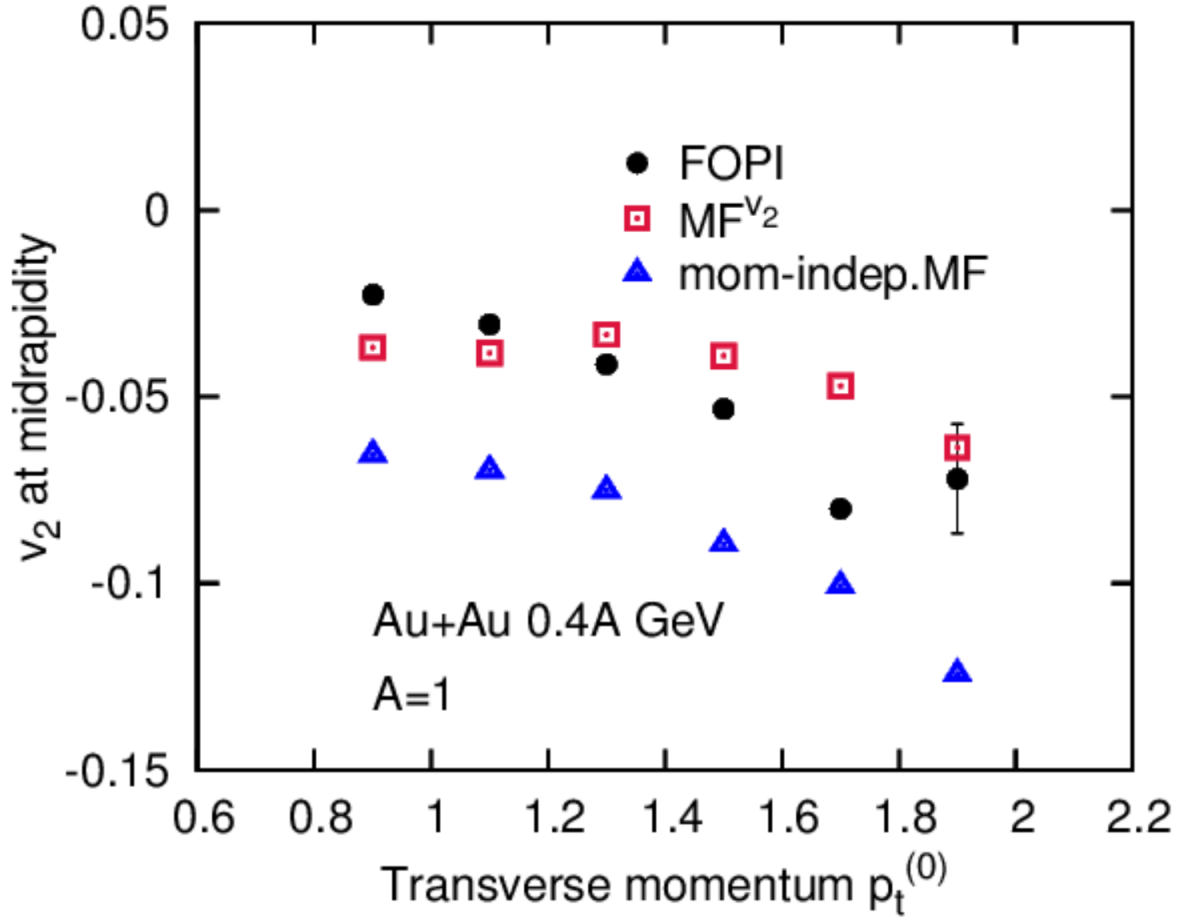


Figure 3.1 Elliptic flow of  $A=1$  (proton) particles, as a function of scaled transverse momentum. Closed dots represent data from the measurements of the FOPI Collaboration of mid-peripheral Au+Au collisions at the beam energy of  $400A$  MeV ( $b \sim 2.0 - 5.3$ fm). The open squares represent pBUU calculations with the soft equation of state ( $K=210$  MeV), which was adjusted to KaoS flow data. The triangles represent pBUU calculations with stiff equation of state ( $K=380$  MeV) and no momentum dependence in MF.

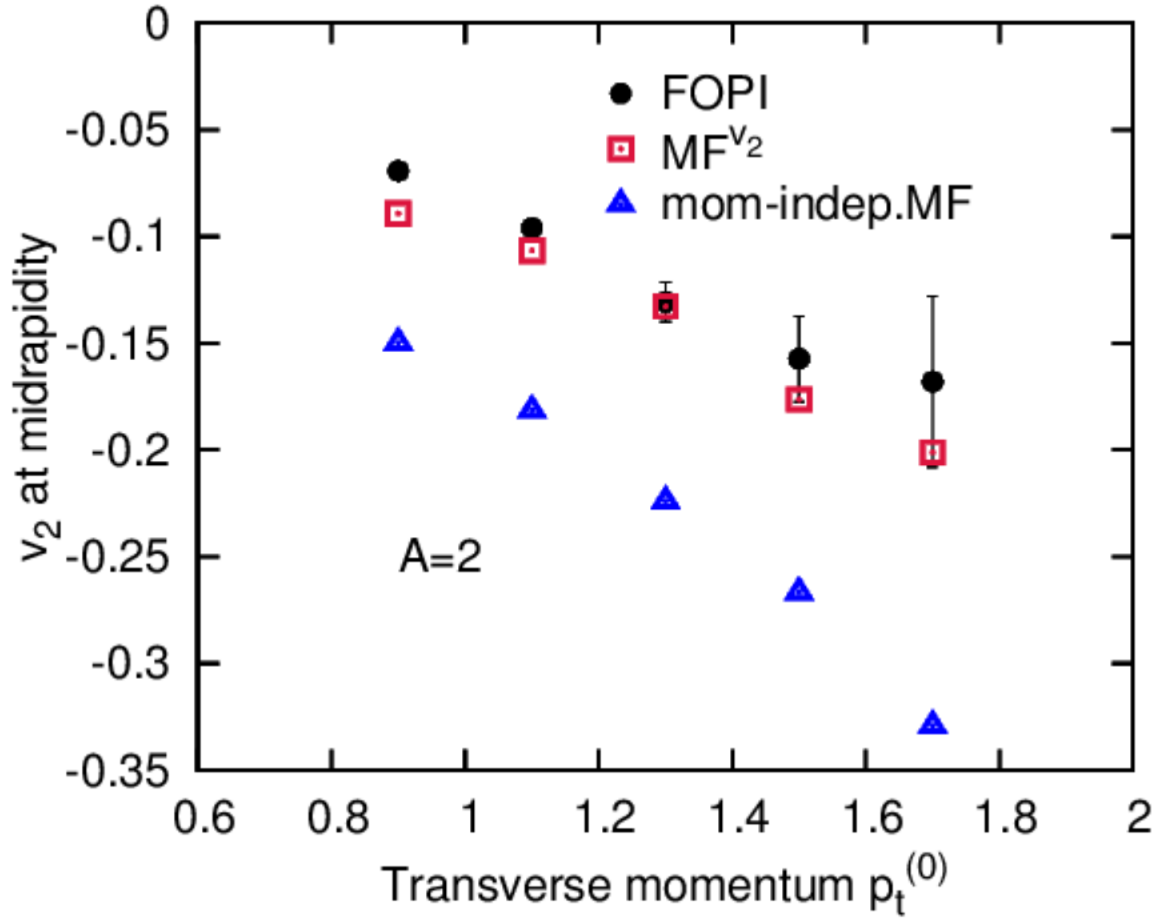


Figure 3.2 Elliptic flow of  $A=2$  (deuteron) particles, as a function of scaled transverse momentum. Closed dots represent data from the measurements of the FOPI Collaboration of mid-peripheral Au+Au collisions at the beam energy of  $400A$  MeV ( $b \sim 2.0 - 5.3$ fm). The open squares represent pBUU calculations with the soft equation of state ( $K=210$  MeV), which was adjusted to KaoS flow data. The triangles represent pBUU calculations with stiff equation of state ( $K=380$  MeV) and no momentum dependence in MF.

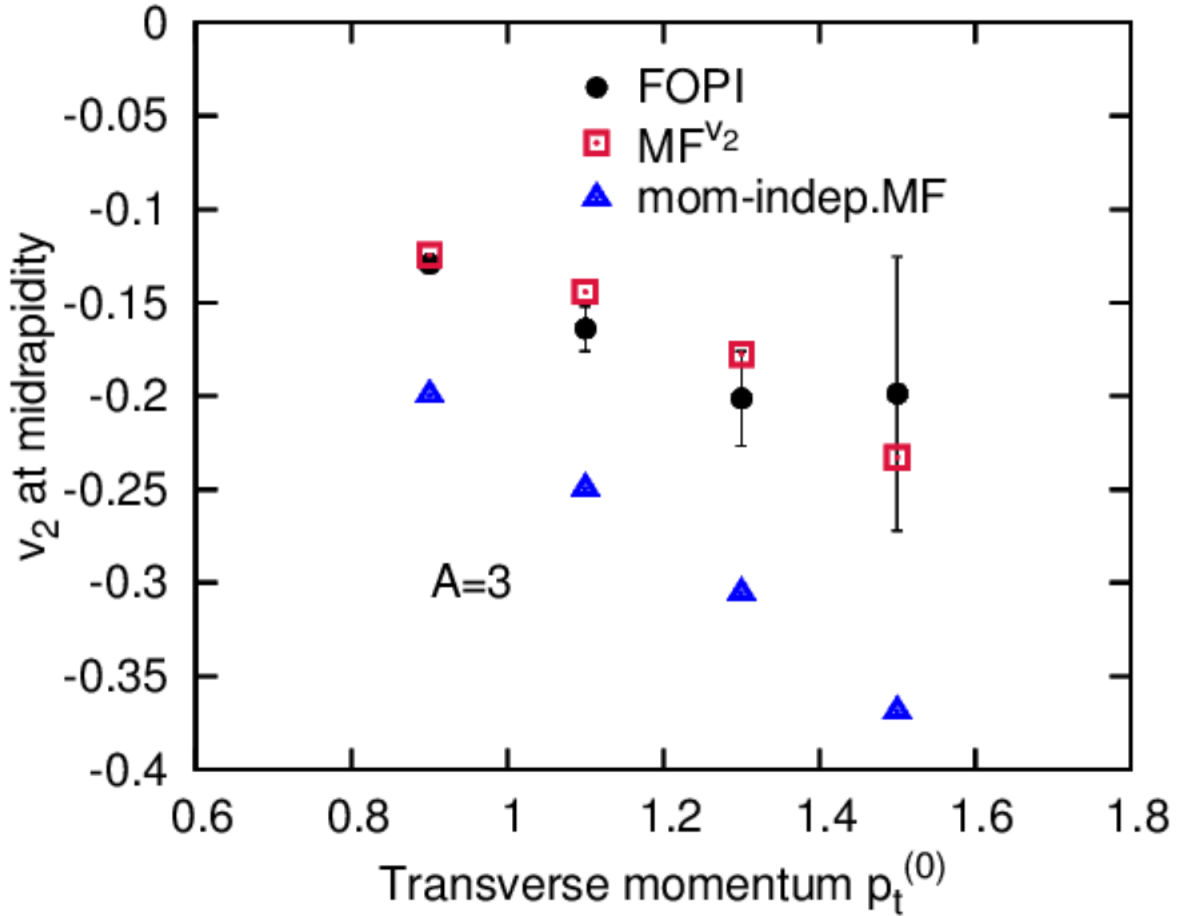


Figure 3.3 Elliptic flow of  $A=3$  (triton and Helium 3) particles, as a function of scaled transverse momentum. Closed dots represent data from the measurements of the FOPI Collaboration of mid-peripheral Au+Au collisions at the beam energy of  $400A$  MeV ( $b \sim 2.0 - 5.3$  fm). The open squares represent pBUU calculations with the soft equation of state ( $K=210$  MeV), which was adjusted to KaoS flow data. The triangles represent pBUU calculations with stiff equation of state ( $K=380$  MeV) and no momentum dependence in MF.

Fig. 2.10-2.12 in the preceding chapter compared the elliptic flow from FOPI measurements to the flow from pBUU simulations utilizing the new momentum-dependent mean field ( $K=230$  MeV), which was fitted to observed pion multiplicities. After including the momentum dependence, the  $K=230$  MeV simulations could not reproduce anymore adequately the elliptic flow

data. However, observations from Figs. 3.1-3.3 suggest that further investigations of the density-dependence and momentum-dependence of the nuclear MF, might result in some reasonable combination of those dependencies that would allow for a simultaneous description of pion and elliptic flow.

### **3.3.1 Elliptic flow and impact parameter**

Before turning to optimization of any potential details in density and momentum dependence of MF, we examine the effect of impact parameter on elliptic flow at mid-rapidity, to understand the potential source of uncertainties in drawn conclusions. Different impact parameters lead to different geometries in nuclear reactions. In a central nuclear collision, the overlapping region of the two nuclei is close to a sphere, while in mid-peripheral collisions, the overlapping region has an almond shape. On the other hand, larger impact parameter imply fewer participant nucleons and reduced maximal densities compared to more central collisions. These factors contribute to producing different elliptic flows under various conditions. In Fig. 3.4, we plot the elliptic flow from pBUU calculations, with effective mass  $m^*/m=0.782$  and incompressibility  $K=270$  MeV, as a function of impact parameter, for Au+Au collisions at 1.2A GeV. The smooth line approximating the results serves to guide the eye. The magnitude of elliptic flow rises from 0 at  $b=0$  and it saturates at higher impact parameters.

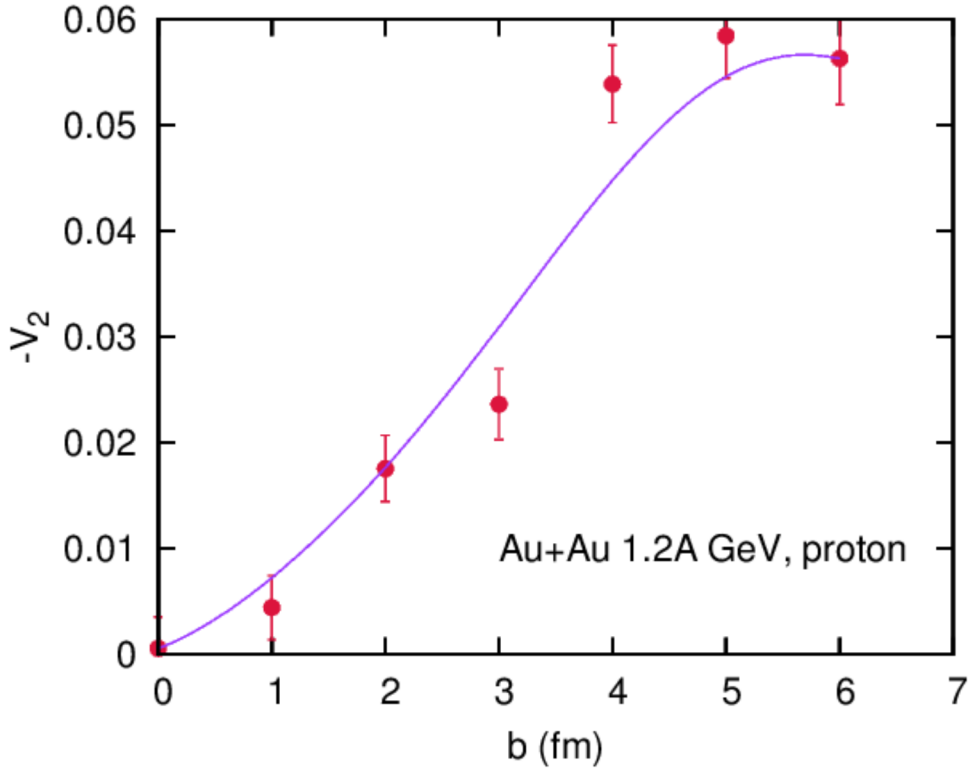


Figure 3.4 Proton elliptic flow as a function of impact parameter, for Au+Au collisions at 1.2A GeV. Dots are calculation points for soft momentum dependent MF with  $m^*/m=0.782$  and  $K=270$  MeV, the line is for guidance purpose. In absence of deformation for colliding nuclei, due to symmetry, the elliptic flow needs to vanish at  $b=0$ . As geometry of the reaction becomes more asymmetric with increasing impact parameter, so does the magnitude of elliptic flow. At higher impact parameters, the flow saturates for a momentum-dependent MF.

In an experiment, the impact parameter is determined through a correlation of reaction observables, such as net particle multiplicity, with reaction centrality. Since such a correlation always has a finite width, the experiment ends up selecting a range of impact parameters. Given that cross section for selecting an impact parameter shrinks to 0 as impact parameter approaches 0, the experiment is never capable of selecting very low impact parameters. Guided by cross section considerations, for a given range of impact parameters, we select the impact parameter equal to the quadratic mean of the largest and smallest value of impact parameter in experiment for simulations.

This approach is assumed to be generally valid. However, we approach the issue with more caution when a particular observable, such as elliptic flow, changes rapidly, particularly nonlinearly, within the considered region of impact parameters and we test the sensitivity of the conclusions to the decisions on the impact parameter in our calculations.

### 3.3.2 Elliptic flow and effective mass

It is believed that the momentum dependence of nuclear mean field plays a dominant role in determination of the flow observables. It has been mentioned in Chapter 2 that effective mass at the Fermi surface is usually calculated to label the different momentum dependent mean field. To illustrate the impact of effective mass on squeeze-out, we show in Fig. 3.5 the anisotropy of proton transverse momentum distribution at midrapidity calculated with different effective mass values. Specifically shown there are for the ratio of out of the reaction plane to in-plane proton yields calculated for Bi+Bi collision at the beam energy of 400A MeV and impact parameter of  $b=7.6\text{fm}$ . The solid, dot-dashed and dashed lines represent pBUU calculations with effective mass  $m^*/m=0.8$ , 0.7 and 0.6, respectively. The incompressibility  $K$  for those calculations was set to 270MeV. The filled triangles in Fig. 3.5 represent, for reference, the data of the KaoS Collaboration[2]. Calculation with  $m^*=0.7m$  produces a stronger elliptic flow than other effective mass values, and it is preferred by the experimental data. The momentum-dependence with  $m^*/m=0.8$  yields similar elliptic flow as the momentum-dependence with  $m^*/m=0.6$ . The non-monotonic behavior of elliptic flow with changes in effective mass can be understood as a result of competing effects of the momentum- and density-dependence of MF. For strong momentum dependence (e.g.  $m^*/m=0.6$ ), the density dependence in MF, from adjusting parameters to the same nuclear incompressibility, is weaker. During the reaction, moreover, on account of the enhanced repulsion between nucleons with large relative momenta, nuclear matter gets less compressed. Lower maximal densities imply fewer collisions between nucleons and slower equilibration. With less equilibration at maximal compression, the squeeze-out signal may drop rather than increase, against naive expectations for dropping effective mass.

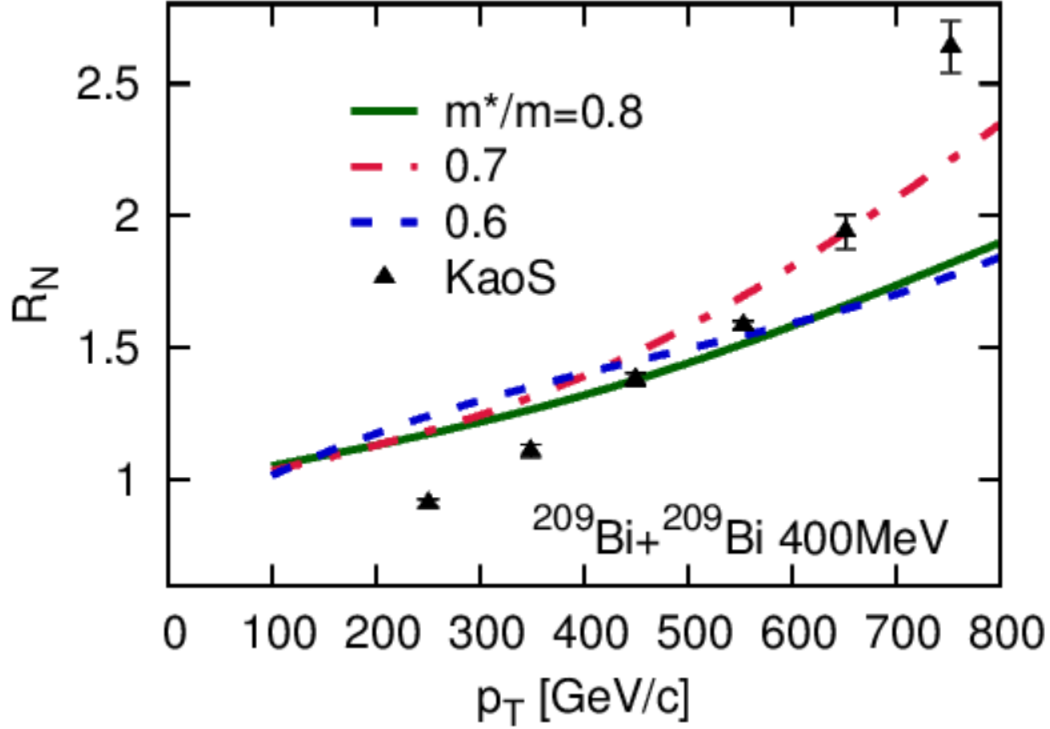


Figure 3.5 Ratio of out-of-the-reaction-plane to in-plane proton yields, as a function of transverse momentum, in mid-peripheral Bi+Bi collisions at the beam energy of 400A MeV and impact parameter  $b \sim 7.6$ fm. Symbols represent data from the measurements of the KaoS Collaboration[2]. Solid, dot-dashed and dashed lines represent pBUU calculations with MFs characterized by  $K=270$ MeV and effective mass  $m^*/m=0.8, 0.7$  and  $0.6$ , respectively.

Within the analysis of the preceding chapter, we found a specific momentum-dependent MF that best described the pion production in HIC, for  $K=210$  MeV, but not flow. In order to seek a MF within pBUU model that optimally describes a variety of observables, we have subsequently engaged in extensive investigations of the impact of the momentum dependence in the MF.

### 3.3.3 Elliptic flow and incompressibility

In this subsection we explore the dependence of the elliptic flow on nuclear incompressibility. In Fig. 3.6 we present again the ratio of out of the reaction plane to in-plane proton yields for Bi+Bi collision at 400A MeV, but now emphasizing sensitivity to incompressibility. The filled triangles represent the data of the KaoS Collaboration[2]. The lines represent pBUU calculations carried out with an effective mass of  $m^*/m=0.7$ . The dot-dashed, dashed, solid and dotted lines have been obtained for the incompressibility values of  $K=300, 270, 240$  and  $210$  MeV, respectively. We can see quite a strong impact of incompressibility on the elliptic flow.

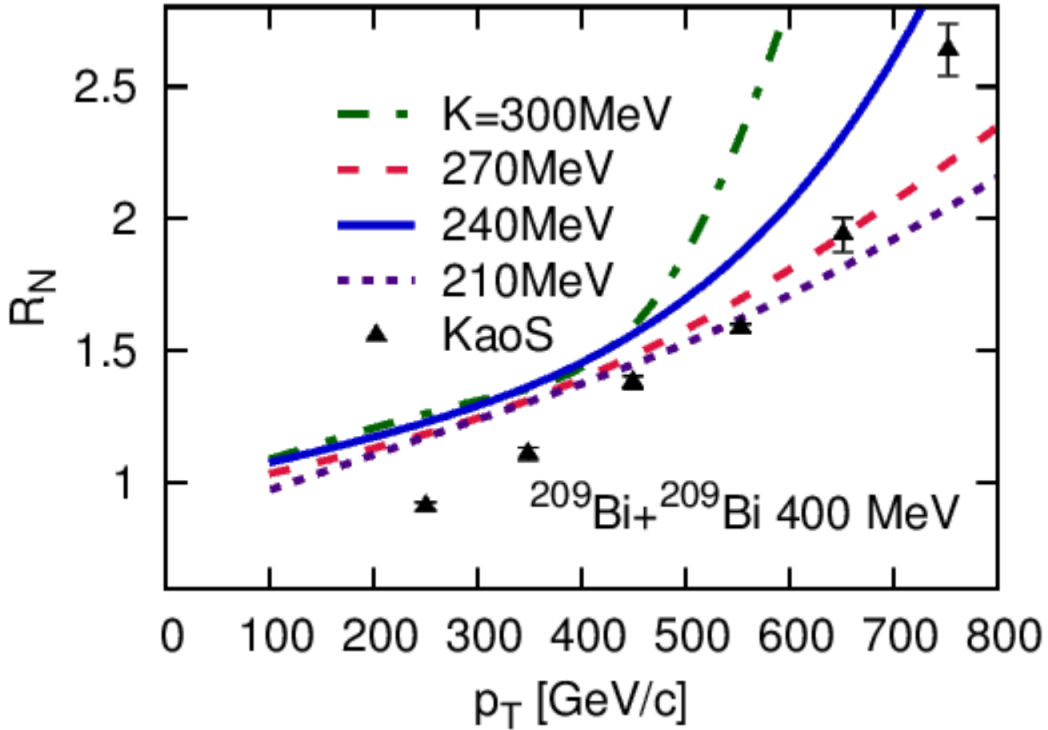


Figure 3.6 Ratio of out-of-the-reaction-plane to in-plane proton yields, as a function of transverse momentum, in mid-peripheral Bi+Bi collisions at the beam energy of 400A MeV and impact parameter  $b \sim 7.6\text{fm}$ . Symbols represent data from the measurements of the KaoS Collaboration[2]. Dot-dashed, dashed, solid and dotted lines represent pBUU calculations with incompressibility  $K=300, 270, 240$  and  $210\text{MeV}$ , respectively, with effective mass  $m^*=0.7m$ .

The calculation with the highest employed incompressibility of  $K=300\text{ MeV}$  gives the strongest flow as expected and the one with the lowest incompressibility of  $K=210\text{ MeV}$  gives the weakest. However, similarly to the situation when changing the effective mass only, we observe a non-monotonic behavior when changing incompressibility only within the range of values  $K=240\text{-}270\text{ MeV}$ . That behavior can again be attributed to the competing effects of momentum and density dependence in the nuclear MF. Specifically, for a lower incompressibility such as  $K=240\text{ MeV}$ , the nuclear matter is compressed to higher density during collisions, than for a higher incom-

compressibility, such as  $K=270$  MeV. The effective mass generally drops with increasing density. At higher density the nucleons move at higher speeds and undergo more collisions that lead to a faster equilibration. In the end, the lower incompressibility may lead to a stronger squeeze-out signal, particularly at high momenta. We have tested that, for incompressibility higher than 300 MeV and lower than 210 MeV, the elliptic flow monotonically increases with increasing  $K$ .

Fig. 3.6 demonstrated the sensitivity of the elliptic flow to the nuclear incompressibility, i.e. density-dependence of nuclear MF. Observation of the significant sensitivity is important for us as opening the possibility of simultaneously describing pion production and elliptic flow in HIC. Clearly the density-dependence of nuclear MF can impact the collective motion of particles emerging at high transverse momenta. In the past, the collective motion was considered with a coarse insertion or removal of momentum dependence into MF, but more subtle points of the interplay between the momentum and density dependencies in MF were not studied.

### **3.4 Constraints on nuclear incompressibility from flow and pion observables**

Given the strong effect of incompressibility on elliptic flow, we revisited the unsolved problem, formulated at the end of chapter 2, of difficulty in simultaneously describing observed pion multiplicities and elliptic flow within nuclear transport theory. The sensitivity of pion yields to the momentum dependence of nuclear MF was demonstrated in chapter 2. There we focused on adjusting the momentum-dependence to reproduce the experimental data. In the following, we explore the consequences of momentum-dependence and density-dependence of MF at the same time, simultaneously varying the parametrization of local particle velocity and value of nuclear incompressibility.

Given limits on how accurate a semiclassical transport theory can be, the variety of challenges before experiments studying multiparticle final states and a general experience in the field, it is not going to make sense to require more than  $\sim 20\%$  in accuracy of describing data with the transport

theory. When allowing for up to 20% difference between elliptic flow and pion multiplicity predictions compared to experimental data, and allowing for simultaneous variations in effective mass and incompressibility, we arrived at a range of MF and EOS parametrizations meeting the conditions. In Fig. 3.7, we show results for proton elliptic flow from the two sets of calculations that bracket the range of EOS as far as incompressibility is concerned,  $K=240$  MeV with  $m^*/m=0.782$ , and  $K=300$  MeV with  $m^*/m=0.582$ . The theoretical results are displayed as a function of transverse momentum and compared to data from the KaoS Collaboration from Bi+Bi collisions at  $b=7.6$ fm and either beam energy of  $400A$  MeV (triangles) or  $700A$  MeV (circles). Within the 20% accuracy either EOS describes adequately data at higher  $p_t$ , where elliptic flow is significant.

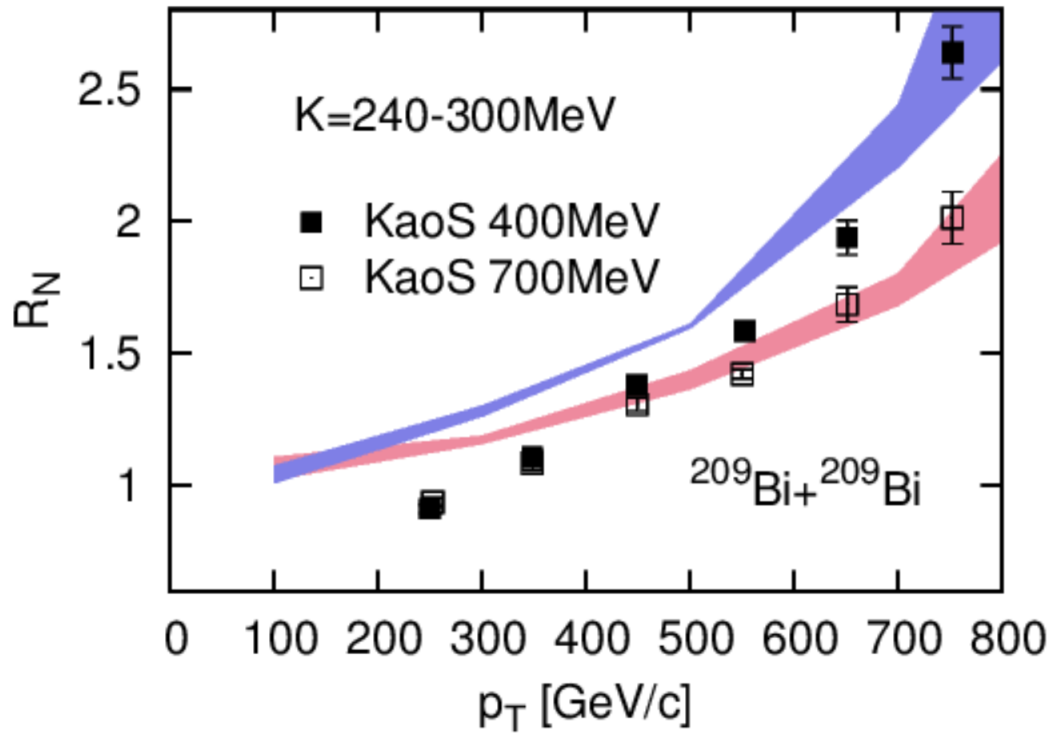


Figure 3.7 Ratio of out of reaction plane to in-plane proton yields, as a function of transverse momentum. Symbols represent data from the measurements of the KaoS Collaboration of mid-peripheral Bi+Bi collisions at the beam energies of 400A MeV and 700MeV ( $b=7.6\text{fm}$ )[2]. Shaded regions represent pBUU calculations with an optimal EOS for incompressibility between  $K=240-300\text{MeV}$ .

Next, in Fig. 3.8 we compare the pBUU predictions for yields of pions, positive and negative, respectively, in Au+Au collisions at  $b=1.4\text{fm}$ , obtained for different MFs, to the measurements of the FOPI Collaboration at 400A MeV and 800A MeV. The data are represented there with filled circles. The optimal range of EOS, as far as reproducing both pion multiplicity and elliptic flow, is represented with shadowed regions. Subsequently, we show in Figs. 3.9-3.11 calculations from two EOS, one with  $K=210\text{ MeV}$  and another with  $K=270\text{ MeV}$  ( $m^*/m=0.75$  in both cases). The former EOS is able to reproduce only pion multiplicities but not elliptic flow; the latter EOS

reasonably describes the elliptic flow but not pion multiplicities. These are two examples showing that outside of our constrained range, one can describe only one of the observables at the best.

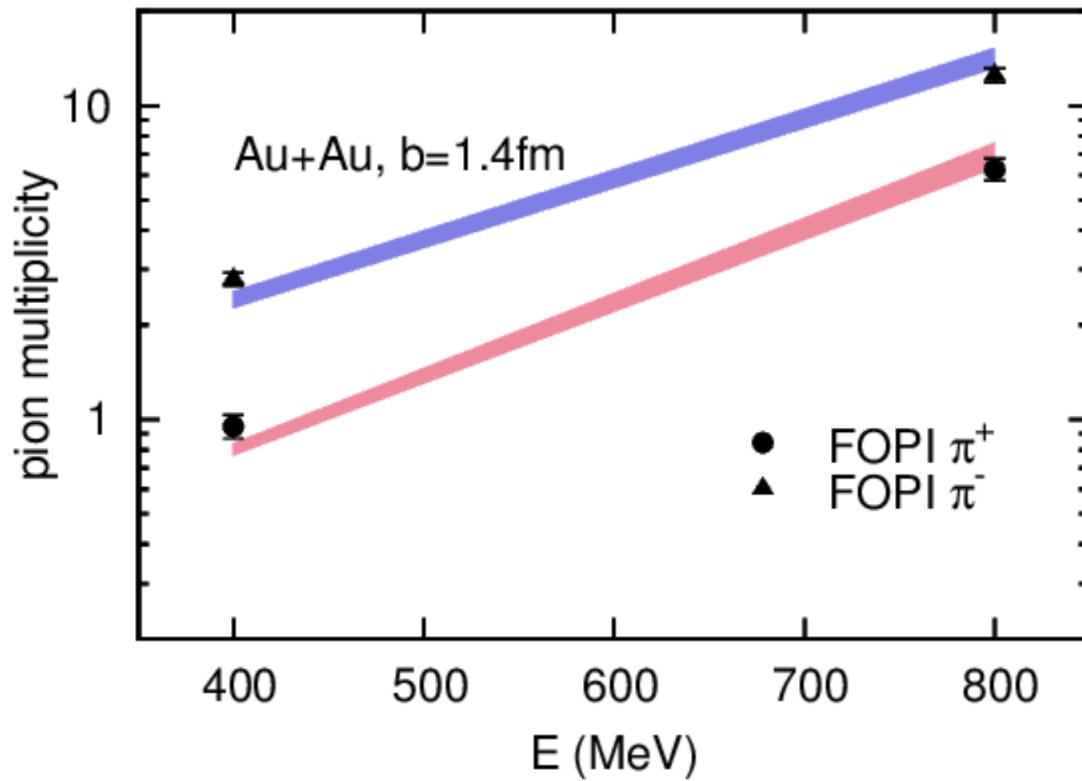


Figure 3.8 Pion multiplicity in central Au+Au collisions vs beam energy. Symbols represent data of the FOPI Collaboration[1]. The shaded region represent pBUU calculations with the range of nuclear equation of state fitted to elliptic flow and pion yields simultaneously.

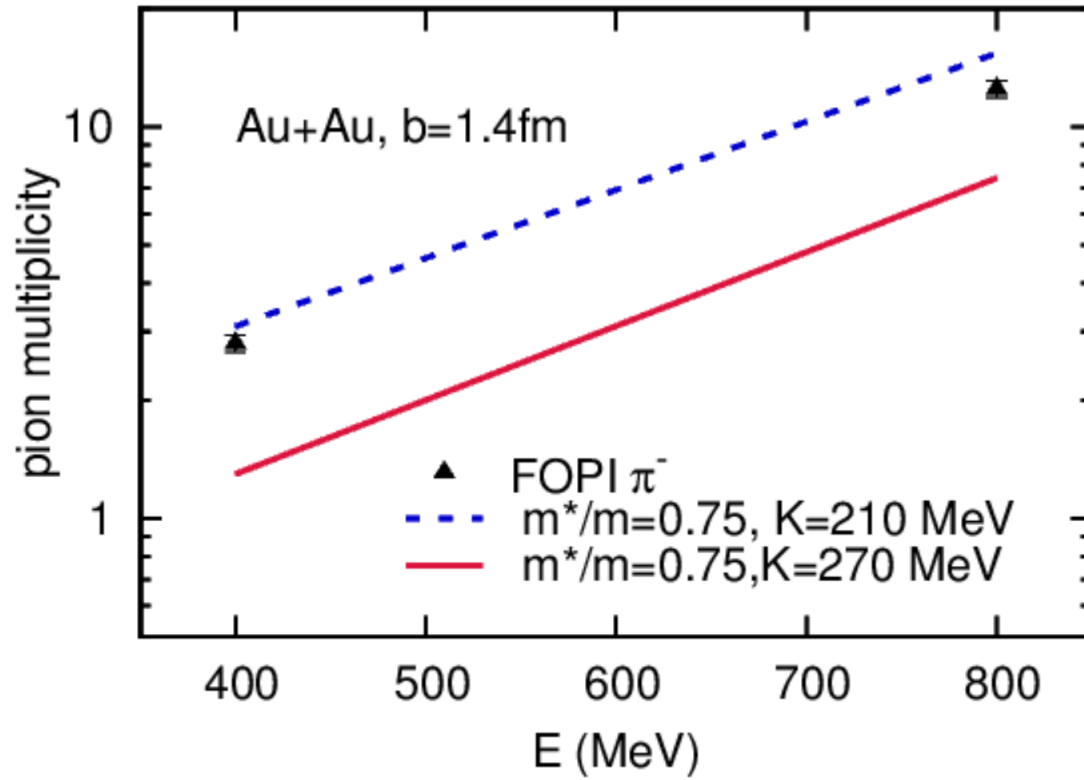


Figure 3.9  $\pi^+$  multiplicity in central Au+Au collisions vs beam energy. Symbols represent data of the FOPI Collaboration[1]. Solid and dashed lines represent calculations carried out with incompressibility  $K=210$  and  $270$  MeV, respectively, and the effective mass  $m^*/m=0.75$  for both.

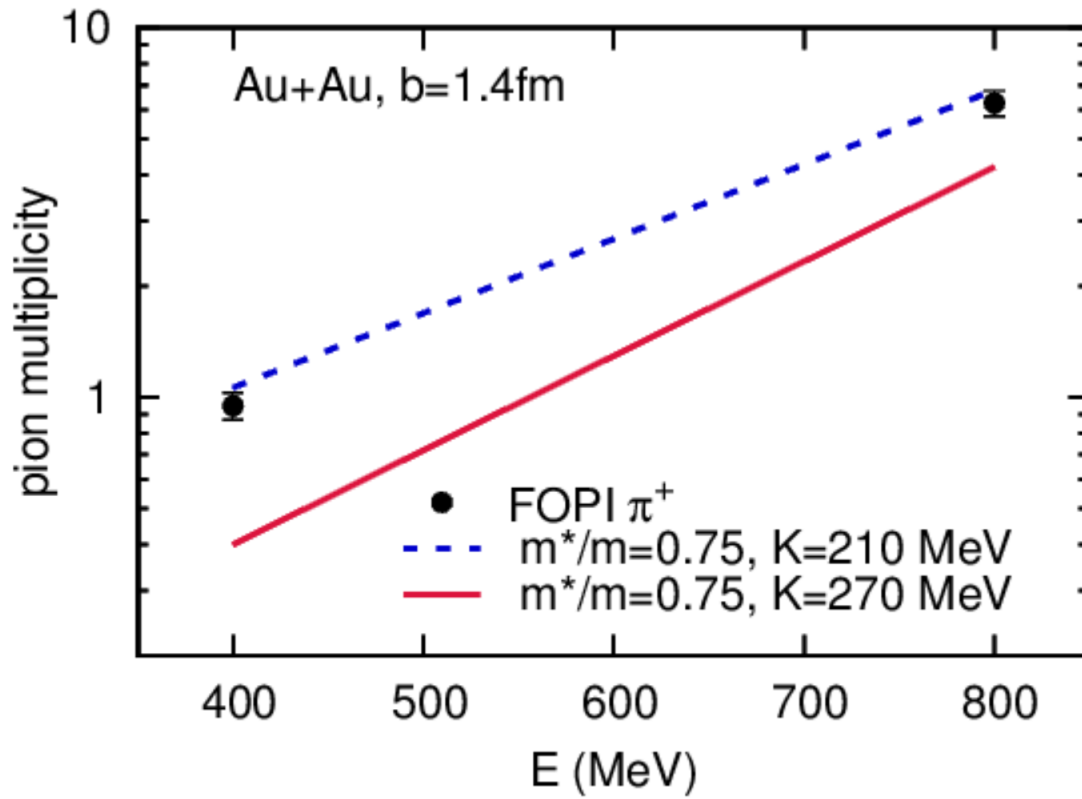


Figure 3.10  $\pi^-$  multiplicity in central Au+Au collisions. Symbols represent data of the FOPI Collaboration[1]. Solid and dashed lines represent calculations with incompressibility  $K=210$  and  $270\text{ MeV}$ , respectively, both with the effective mass  $m^*/m=0.75$ .

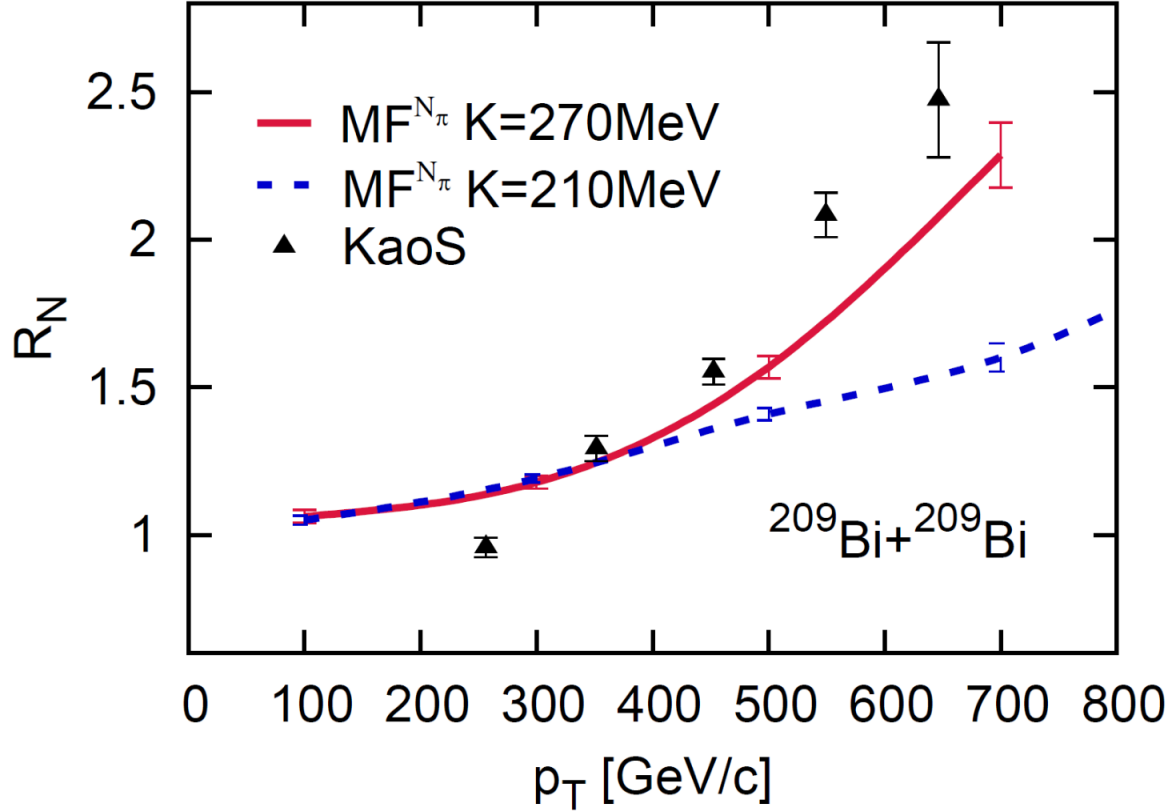


Figure 3.11 Ratio of out of reaction plane to in-plane proton yields, as a function of transverse momentum. Symbols represent data from the measurements of the KaoS Collaboration of mid-peripheral Bi+Bi collisions at the beam energy of 400A MeV ( $b=8.7$  fm)[2]. Dashed and solid lines represent pBUU calculations with incompressibility  $K=210$  and  $270$  MeV, respectively, both with the effective mass  $m^*/m=0.75$ .

Next we turn to constraints on EOS that follow from requiring that the associated MFs produce a sensible simultaneous agreement of theoretical predictions with both data on pion multiplicity in central collisions and on proton elliptic flow. In the plane of energy per nucleon in cold matter vs density we cross out the region covered by the EOS that yield simultaneous acceptable agreement with both pion and elliptic flow data. In collisions to which the data pertain, the matter is excited. Since we need to extrapolate to zero temperature, we broaden the region by uncertainty in extrapolation. We complement that uncertainty by one due to the fact that impact of different densities is

averaged over space and time. Our final constraints are shown in Fig. 3.12 and are compared there to the constraints arrived recently by the FOPI-IQMD Partnership analyzing elliptic flow from the FOPI measurements. As is apparent, our constraints yield a somewhat stiffer EOS in the region of  $\rho > 1.5\rho_0$  than the FOPI-IQMD Partnership.

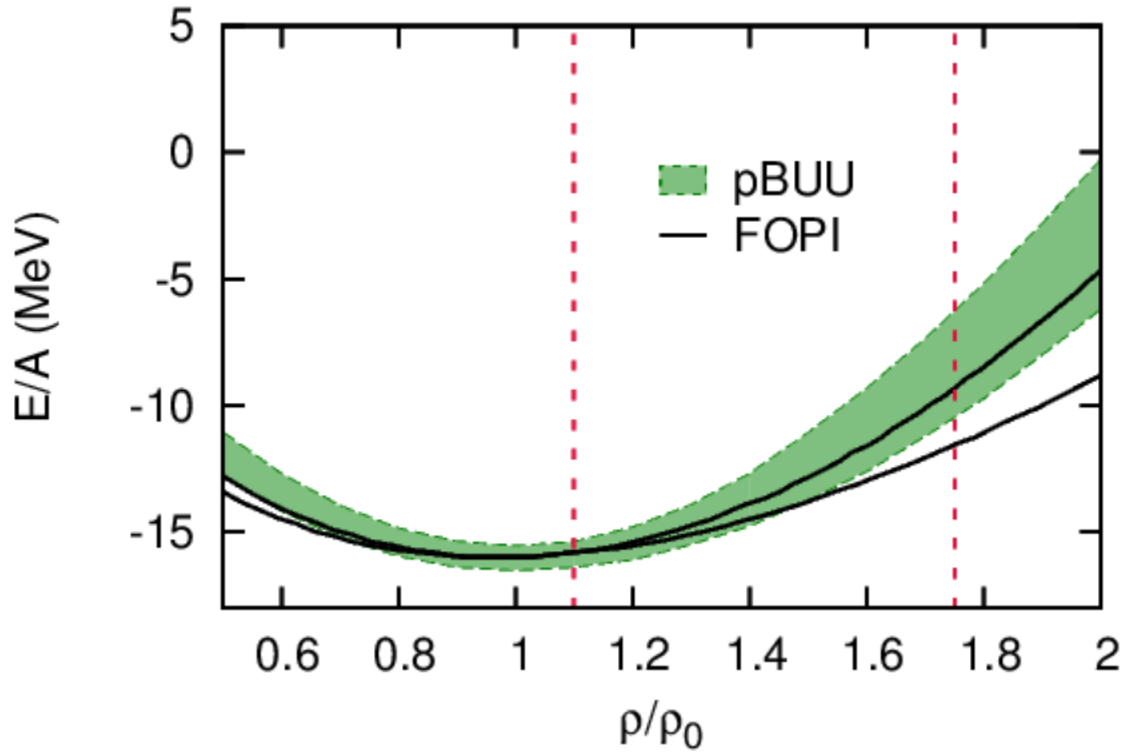


Figure 3.12 Energy per nucleon for symmetric nuclear matter as a function of scaled density. The solid lines represent constraints, upper and lower, on the energy arrived at by the FOPI-IQMD Partnership. The shaded region represents our conclusions, with the pion yields and elliptic flow testing the supranormal region. The vertical dashed lines show the rough density region that gets probed by the observables in the calculations.

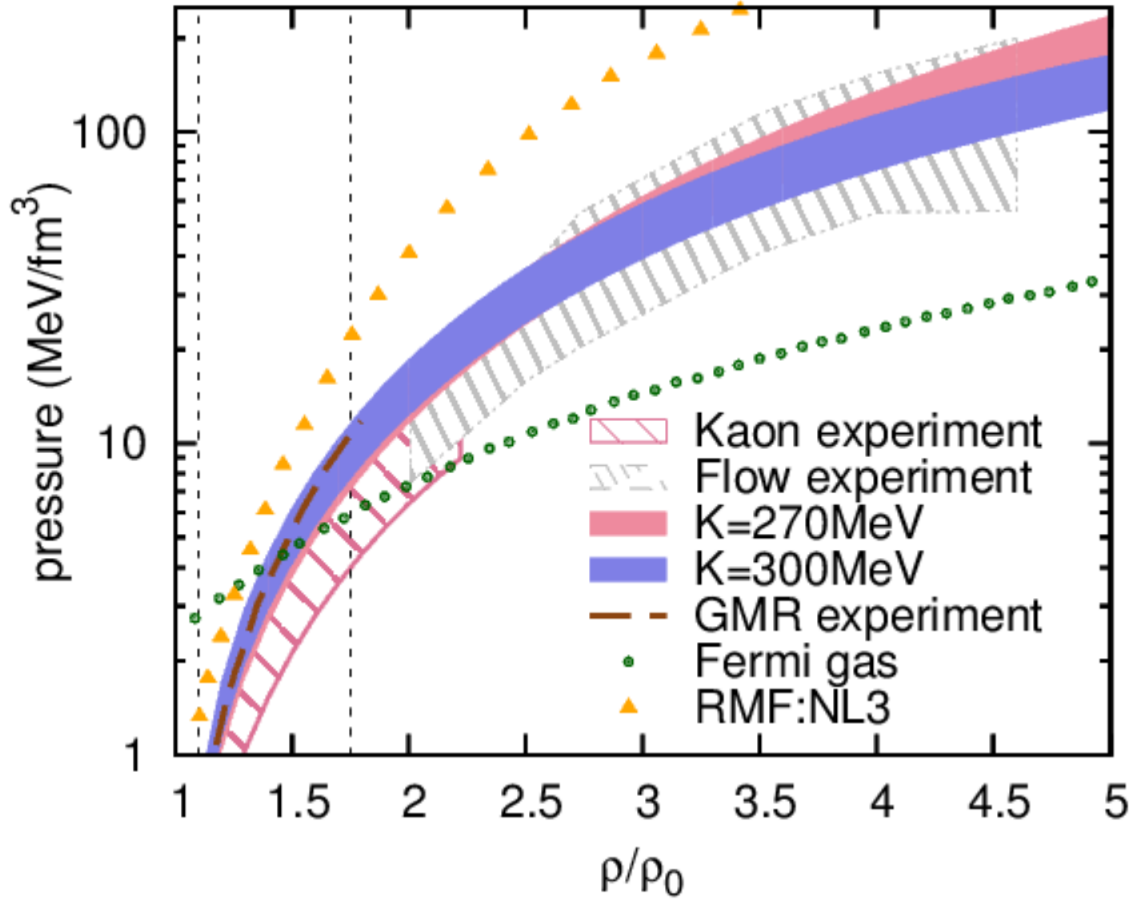


Figure 3.13 Nuclear equation of state plotted as pressure in terms of scaled density. Patterned shaded areas represent constraints deduce by comparing transport theory to data on kaon multiplicity and on directed and elliptic flow. The solid line on the left represents the equation of state preferred by analysis of the recent giant monopole resonance (GMR) experiment. Dots represents the noninteracting Fermi gas and triangles represent the relativistic mean field (RMF) model NL3. The shaded regions, pink and blue, represent respective pressure constraints that can be deduced when relying on either an EOS with  $K=240$  MeV or  $K=300$  MeV within the pBUU transport model. The vertical dashed lines show the rough density region that gets probed by the observables in the calculations.

In a similar manner as in extracting energy per nucleon, we extract pressure as a function of density in nuclear matter. Our conclusions on pressure are represented in Fig. 3.13 and compared

there to other conclusions drawn in the literature. Each of our boundary EOS yields an uncertainty region tied to the extrapolation to zero temperature. By comparing pressure density along beam axis and transverse directions, we estimated the error in the pressure from the difference. The net uncertainty, when varying  $K$ , roughly corresponds to the combination of the two regions. If eventually an independent preference emerges for one or another end of the incompressibility range, the uncertainty region for the EOS may shrink. In addition to our own constraints, we show, with patterned regions, the constraints arrive in the past in the literature when analyzing combined directed and elliptic flow data and when analyzing kaon yields. The solid line represents the EOS preferred by a recent GMR analysis. For reference we show further the pressure for the relativistic mean field model NL3 and the pressure for a noninteracting Fermi gas, with filled triangles and circles, respectively. The vertical dashed lines indicate the densities, from simulations, that get probed by the observables we concentrate on. As one can see, there is good degree of overlap between different constraints. Our constraints seem consistent with those from combined directed and elliptic flow analysis, when extrapolated to higher densities.

### **3.5 Conclusion**

In this chapter we tested the sensitivity of elliptic flow to nuclear incompressibility, in addition to the sensitivity to the momentum dependence of MF. We reexamined the parametrizations of EOS and MF in pBUU model aiming at a simultaneous description of pion yields and proton elliptic flow, at 20% level. We have demonstrated that it is possible to describe both sets of data when assuming the incompressibility to be within the range  $K=(240-300)$  MeV. Even though the range of incompressibilities is wide, the range of energies per nucleon and pressures is relatively narrow for higher densities, even when accounting for various uncertainties in drawing the conclusions.

## CHAPTER 4

### CONSTRAINTS ON SYMMETRY ENERGY AT SUPRANORMAL DENSITIES

#### 4.1 Introduction to symmetry energy

Isospin is a quantum number introduced to provide mathematical framework for the symmetry of strong interactions associated with the fact that up and down quark have nearly the same mass on the scale of energies relevant for strongly interacting systems. Proton ( $p$ ) and neutron ( $n$ ) are considered to be different directions for the same particle in isospin space. For two nucleons, the existence of stable deuteron demonstrates that net isospin  $T = 0$   $np$  interaction is stronger than the  $T = 1$   $nn$  and  $pp$  interactions. Properties of strongly interacting nuclear matter are largely affected by the isospin structure of the system. Therefore, the symmetry energy, which is related to the n-p imbalance in a nuclear system, has been extensively studied by nuclear physicists.

As we showed in the previous chapter, energy per nucleon in a nuclear matter can be expanded in powers of the neutron-proton asymmetry  $\alpha$  of the system:

$$\frac{E}{A}(\rho, \alpha) = \frac{E}{A}(\rho, 0) + S(\rho)\alpha^2 + O(\alpha^4). \quad (4.1)$$

The coefficient  $S(\rho)$  is termed as the symmetry energy. It is usually assumed that contributions from fourth-order term are small.

It is easy to see the effect of symmetry energy in the Bethe-Weizsacker formula as well. This semi-empirical mass formula gives a good prediction for the nuclear binding energies. Liquid drop concepts are used for justification of the formula, and the binding energy is expressed in terms of five main terms:

$$E_B = a_V A - a_{surf} A^{2/3} - a_{sym} (N - Z)^2 / A - a_C Z^2 / A^{1/3} + E_{pair}. \quad (4.2)$$

Above,  $A$  is the total number of nucleons,  $N$  is the number of neutrons and  $Z$  is the number of protons. The coefficients  $a_V$ ,  $a_{surf}$ ,  $a_{sym}$ ,  $a_C$  represents the strength of the volume term, surface term, symmetry term, and Coulomb term, respectively. The last term represents the empirically parametrized pairing interaction. The symmetry energy term accounts for the imbalance of the proton and neutron numbers in a nucleus. Due to its density dependence, the symmetry energy pushes the excess protons and neutrons to the surface of the nucleus, while helping to bring the system to the lowest energy state. Such effect is observed in the existence of neutron skin in asymmetric nuclei[71]. The neutron skin thickness is directly correlated to the slope of symmetry energy with density[13, 72, 73, 74]. Other physical properties, for instance, nuclear masses, isovector Giant Dipole Resonance[12], and multi-fragmentation in heavy ion collisions are all affected by the nuclear symmetry energy[75, 7, 76, 77, 78, 79, 80, 81]. In astrophysical scenarios, supernova dynamics, proton-neutron star evolution, neutron star stability against gravitational impulsion, stellar radii, moment of inertia, ect. are dependent on the symmetry energy as well[3, 82, 83].

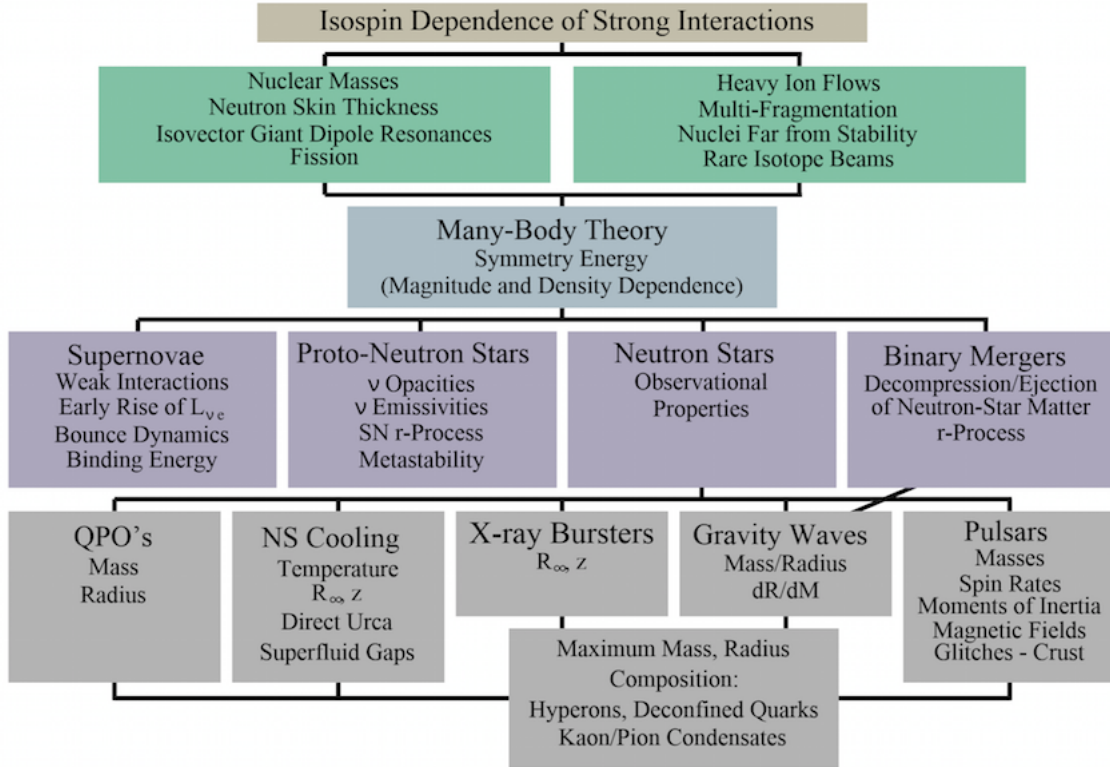


Figure 4.1 The multifaceted influence of the nuclear symmetry energy. [3]

In stable nuclei, the density in the center is about the normal density  $\rho=0.16\text{fm}^{-3}$  and it decreases to zero within the surface. The temperature of ground state nuclei is by definition zero. In intermediate energy heavy ion collisions, we are probing the density region around twice the normal density and the nuclear systems are at high temperatures. In neutron star case, the density in the center can reach as high as nine times the normal density, while the temperature is relatively low. To describe properties of nuclear systems in such different regions of the phase diagram, the behavior of symmetry energy as a function of density is much needed in order to understand the properties of various nuclear systems. Figure 4.1 is taken from ref.[3]. It lists the physics observables and theoretical methods that are important for extracting and studying the information about the density dependence of the symmetry energy as well as its magnitude. In this chapter, we explore sensitive observables to constrain the high density behavior of the symmetry energy.

## 4.2 Motivation

As we pointed out, nuclear symmetry energy is an important quantity that directly relates to most of the physical properties of neutron stars, isospin dynamics in HIC, etc. However, to date, density dependence of symmetry energy at higher than normal density is not well constrained. Figure 4.2 shows a variety of theoretical expectations regarding the nuclear symmetry energy [4]. Among the 21 sets of Skyrme interactions shown, all have been chosen to fit to the basic nuclear properties at saturation density. However, they predict very different behavior of symmetry energy beyond the saturation density. For some of the interactions the symmetry energy monotonically increases with density (stiff symmetry energy), while for some interactions the symmetry energy starts to decrease at higher densities (soft symmetry energy).

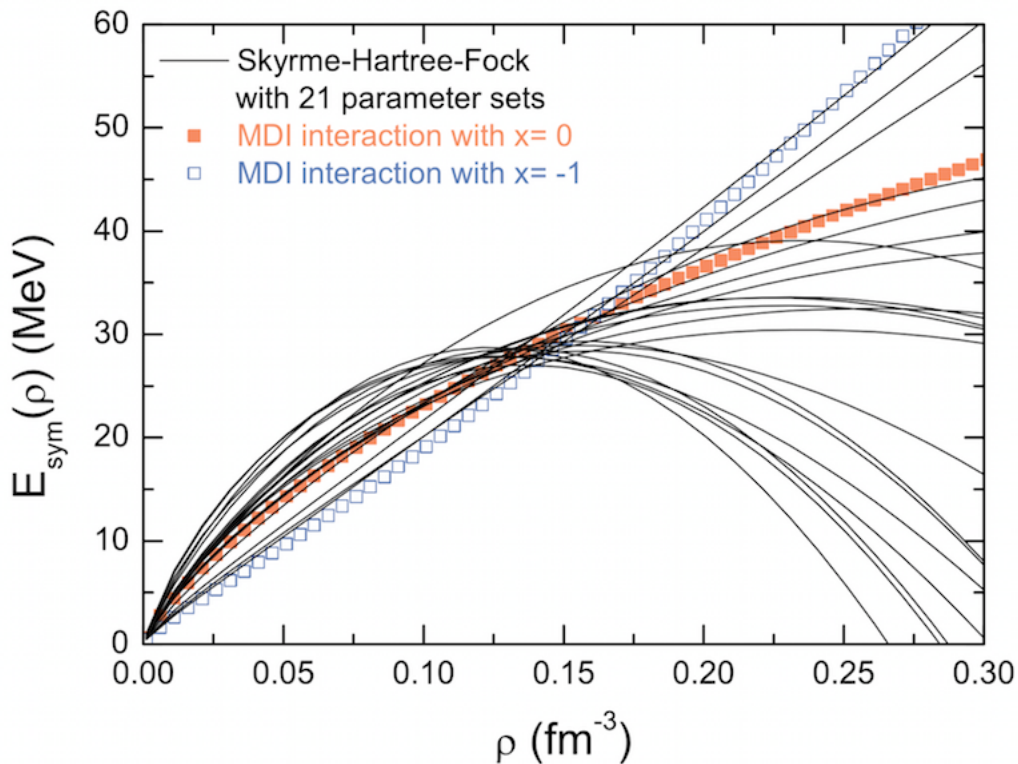


Figure 4.2 Density dependence of nuclear symmetry energy for 21 sets of Skyrme interaction parameters. Symbols represent momentum-dependent interactions in IBUU04 [4].

With such large uncertainties in the theoretical expectations, it is important to find a sensitive observable for experiments to constrain the behavior of symmetry energy at supranormal densities. Pions produced in HIC generally originate from higher than normal density regions, so pions might serve as a good probe of the high density behavior of symmetry energy.

### 4.3 Charged pion ratios

During intermediate stages of heavy-ion collisions, density in the overlap region of the two nuclei can easily reach values twice as high as the saturation density. Pions are produced in that region through production and decay of delta resonances, when the inter-nucleon energy exceeds the pion threshold. In the pBUU transport model parametrization, apart from Coulomb interactions, pions also feel a pion potential that depends on isospin and symmetry energy.

The isospin contribution to the energy  $E_T$  in the parametrization of total energy for pBUU is

$$E_T = 4 \int d\vec{r} S(\rho) \frac{\rho_T^2}{\rho}, \quad (4.3)$$

where  $\rho_T = \sum_X \rho_X t_{3X}$  and  $t_{3X}$  is the third component of isospin for species X. The symmetry-energy factor S above can be conveniently decomposed as

$$S(\rho) = S_{kin0} \left( \frac{\rho}{\rho_0} \right)^{\frac{2}{3}} + S_{int}(\rho), \quad (4.4)$$

where the first r.h.s. term, with  $S_{kin0} \simeq 12.3\text{MeV}$ , represents the symmetry energy in absence of interactions, due to Pauli principle, and the second term represents interaction contribution. In [29] and the calculations here so far, the interaction contribution was of the simplest possible linear form

$$S_{int0}(\rho) = S_{int0} \left( \frac{\rho}{\rho_0} \right). \quad (4.5)$$

However, this can be modified to a power parametrization

$$S_{int0}(\rho) = S_{int0} \left( \frac{\rho}{\rho_0} \right)^\gamma, \quad (4.6)$$

for more generality. Larger values of  $\gamma$  produce symmetry energies rising quickly with density around  $\rho_0$ . Such symmetry energies are generally termed stiff. Low values of  $\gamma$  yield symmetry energies changing slowly around  $\rho_0$ . These are termed soft. Description of nuclear masses requires  $S_{int0} \sim 20\text{MeV}$  [84, 85], best accompanied by a positive correlation between  $S_{int0}$  and  $\gamma$ .

The pion potential, as a result, is

$$U_{\pi\pm} = \mp 8 S_{int0} \rho_T \frac{\rho^{\gamma-1}}{\rho_0^\gamma}. \quad (4.7)$$

Consistently with the  $\Delta/N^* \leftrightarrow n + \pi$  decay, the optical potential for  $\Delta$  resonances satisfies  $U_\Delta = U_N + U_\pi$ , where  $U_N$  is the optical potential for nucleons. Pion production yields consistent with Clebsch-Gordan coefficients lead to a simple relation between primordial charged pion ratio and neutron-proton ratio of the participants follows from consideration of the chain of processes [86]:

$$\pi^-/\pi^+ \equiv \frac{5N^2 + NZ}{5Z^2 + NZ} \approx (N/Z)^2. \quad (4.8)$$

Above relation shows a direct correlation between charged pion ratio and the isospin content in the systems. Hence, pion observables in HIC are also very important for constraining the stiffness of symmetry energy. Li was first to propose that charged pion ratio is a sensitive observable for high density behavior of symmetry energy [81]. The link between the pion yield ratio and symmetry energy turned out subsequently to be less straight forward than first proposed [81], though, with different transport models contradicting each other, as is in particular illustrated in Fig. 4.3.

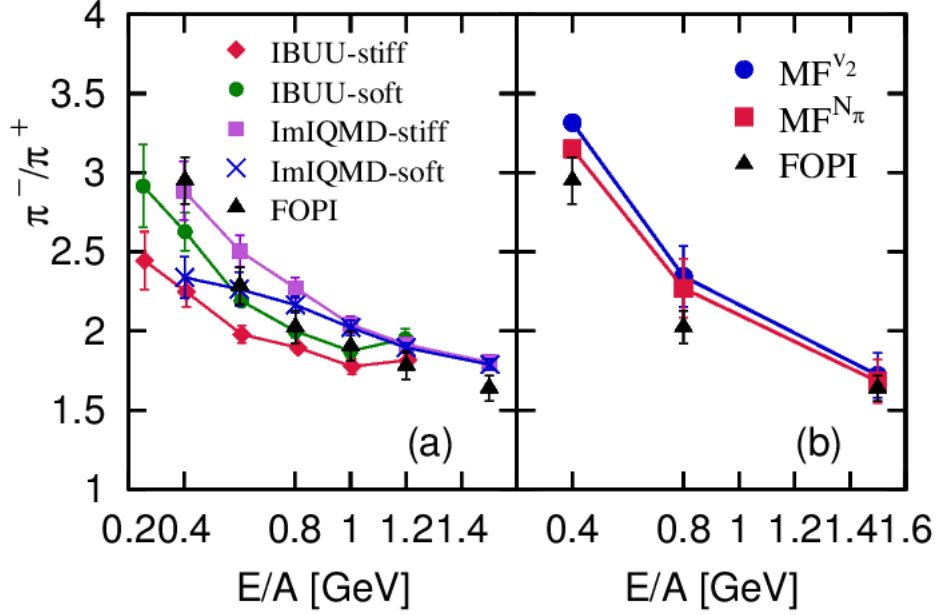


Figure 4.3 (Color online) Pion ratios in central Au+Au collisions, as a function of beam energy. Data of the FOPI Collaboration are represented by filled triangles. The left panel compares predictions from IBUU and ImIQMD models to the data. The IBUU calculations employing stiff and soft symmetry energies are represented there by filled diamonds and filled circles, respectively. The ImIQMD employing stiff and soft symmetry energies are, on the other hand, represented there by filled squares and crosses, respectively. The right panel compares predictions from pBUU model to the data. Calculations employing  $v_2$ -optimized MF and  $N_\pi$ -adjusted MF are represented by filled circles and filled squares, respectively. In our calculations here, the potential part of the symmetry energy is linear in density.

Figure 4.3 displays ratios of net yields of charged pions stemming from central Au+Au collisions at different beam energies. The filled triangles represent measurements of the FOPI Collaboration [87]. Other symbols represent results of different transport calculations. In the panel (a) of Fig. 4.3, it is seen that, within IBUU calculations [88], a stiff symmetry energy gives rise to a lower  $\pi^-/\pi^+$  ratio than does a soft energy. However, the opposite is true for the ImIQMD calculations [89], as seen in the same panel, which is one of the current contradictions in the literature,

mentioned before.

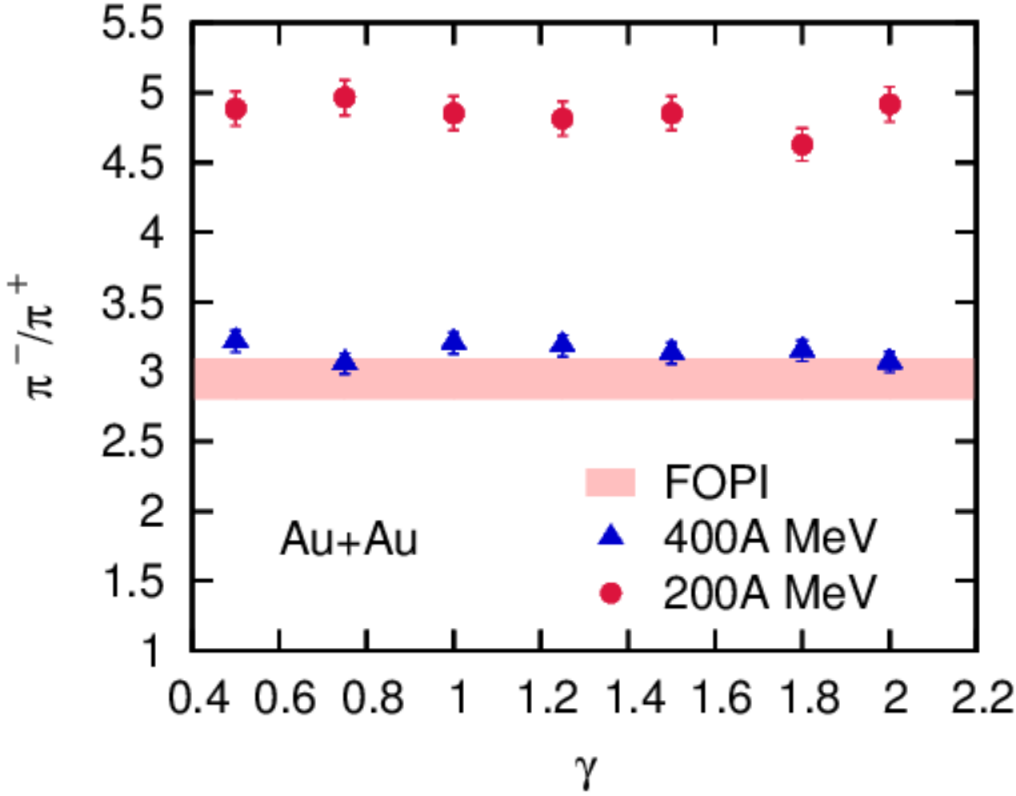


Figure 4.4 (Color online) Ratio of net charged pion yields in central Au+Au collisions at 400A MeV and 200A MeV, as a function of the stiffness of symmetry energy  $\gamma$ , from pBUU calculations using  $N_\pi$ -adjusted MF. The dashed region represents the 400A MeV FOPI measurement. The theoretical errors are due to statistical sampling in the pBUU calculations.

In our own calculations, the  $\pi^-/\pi^+$  net yield ratio is practically independent of the details in the momentum dependence of MF, as illustrated in panel (b) of Fig. 4.3, where we show results utilizing both  $v_2$ -optimized and  $N_\pi$ -adjusted MF. The results are obtained for Au+Au collisions at  $b < 2\text{fm}$ . We use here the linear  $S_{int}$ , Eq. (4.6), and either set of results agrees, within statistical uncertainty, with the FOPI measurements. Importantly, we further find that the net charged pion ratio and the agreement with the measurements remain largely independent of the stiffness of symmetry energy. That is illustrated in Fig. 4.4, where we show pBUU results obtained in

calculations of central Au+Au collisions at 200 and 400A MeV, when changing  $\gamma$  in the symmetry energy Eq.(4.7).

#### 4.4 Pion potential

One detail in pBUU that may give rise to different sensitivity to the symmetry energy for net pion yields, than in other transport calculations, is the presence of a strong interaction potential acting on pions and driven by isospin imbalance. The non-zero pion potential is given in Eq. 4.7. In IBUU and ImIQMD, such strong-interaction potentials acting on pions have been lacking.

Pion-nucleus optical potential has been used to explain the existence of pionic atoms. Pionic atoms are systems consisting of a negatively charged pion and positively charged atomic nucleus. Because of the heavier mass, pion has smaller Bohr radius than that of the electron, providing better tool for testing nuclear properties. While the Coulomb interaction attracts the pion to the nucleus, the strong interaction repels the pions when the nucleus has more neutrons than protons.

Toki et al., in particular, constructed a pion potential that successfully described the deeply bound states of pionic atoms [5]. In Fig. 4.5, the potential in pBUU, for three values of  $\gamma$ , is compared to that of Toki, for  $^{197}\text{Au}$ . Given that our potential in the form (4.8) can only represent the so called s-wave contribution to the  $\pi$ -nucleus potential, we drop, in the comparison, the small p-wave contribution to the potential of [5]. The tails are different in our potentials compared to Toki, due to excessively abrupt changes of density in the semiclassical Thomas-Fermi model (the  $T=0$  limit of our transport model) in the surface region. For pions moving across a HIC zone, however, the most important is the magnitude of the potential over regions where density changes slowly, including nuclear interior in the ground state. In the interior, our potentials for  $\gamma$  from 1 to 2 are within 30% from the Toki's potential.

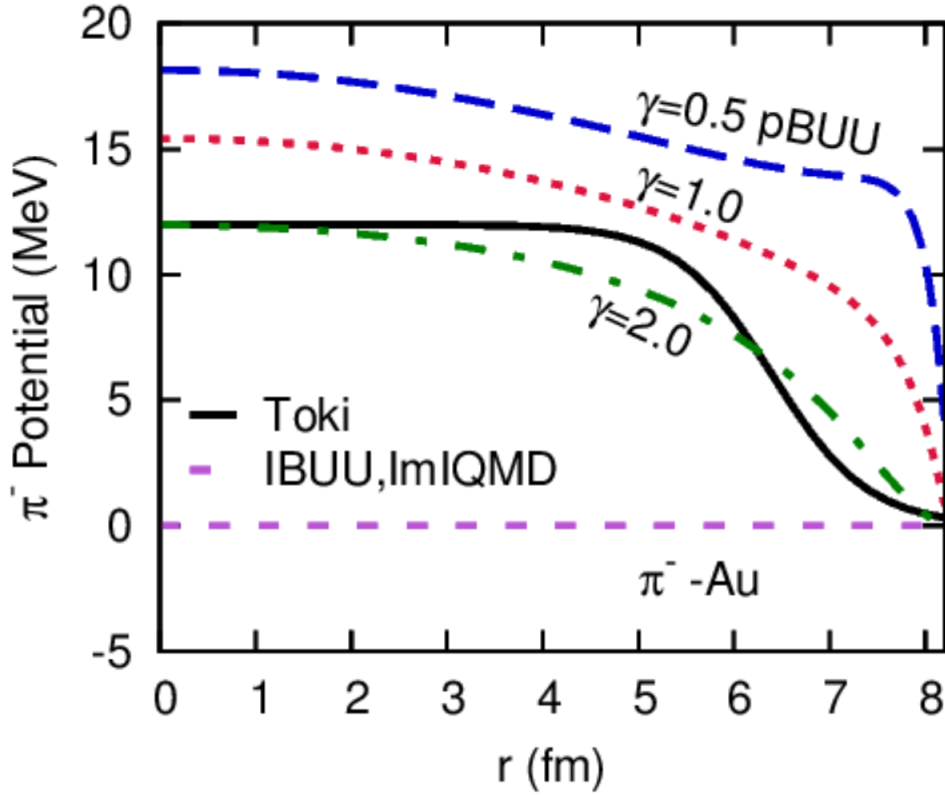


Figure 4.5 (Color online) S-wave contribution to  $\pi^- - {}^{197}\text{Au}$  optical potential. Solid line represents the work of Toki [5]. Short-dash, dotted and dash-dotted lines represent pion potentials from pBUU parameterization for  $\gamma = 0.5, 1.0, 2.0$ , respectively, in the interaction part of the symmetry energy. Long dashed line represents the lack of corresponding potentials in the IBUU and ImIQMD models.

The potentials of different sign for  $\pi^+$  and  $\pi^-$ , each equal in magnitude to the difference between neutron and proton mean fields, and also a difference in the potentials for  $\Delta$ , may produce enough difference in the propagation of charged pions in the pBUU relative to other models to affect predictions.

## 4.5 Differential pion ratios

While we found no sensitivity in pBUU of net charged pion yield ratios, around threshold, to  $S(\rho)$ , still the general idea [81] contains convincing elements. Potentially, more differential ratios of charged pion yields could provide access to  $S(\rho)$  at supranormal densities. In Fig. 4.6-4.8, we explore the sensitivity of charged-pion spectra to the stiffness of symmetry energy. The first two figures illustrate the  $\pi^-/\pi^+$  ratio as a function of pion c.m. energy and the third illustrates the average c.m. energies for the charged pions. Difference in the average c.m. energies, between  $\pi^+$  and  $\pi^-$ , is additionally plotted in Fig. 4.8, as a function of the stiffness  $\gamma$  of the symmetry energy, for Au+Au at 200A MeV.

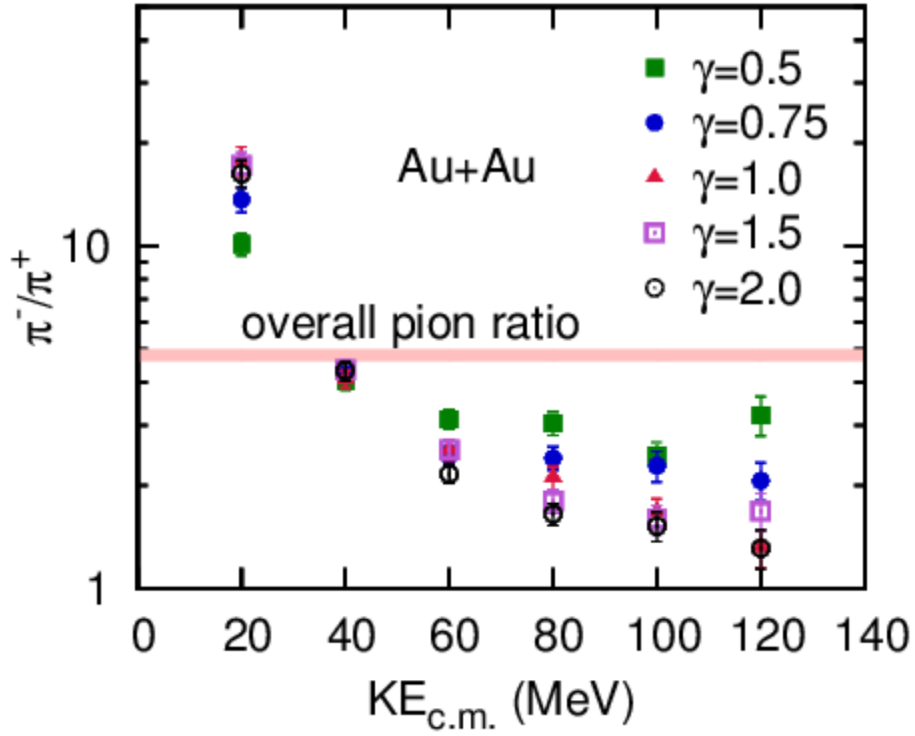


Figure 4.6 (Color online) Charged pion ratio in central Au+Au collisions at 200A MeV, as a function of kinetic energy in the center of mass frame, for different values of the stiffness  $\gamma$  of the symmetry energy, from 0.5 to 2.0. The horizontal line represents the ratio of net charged pion yields.

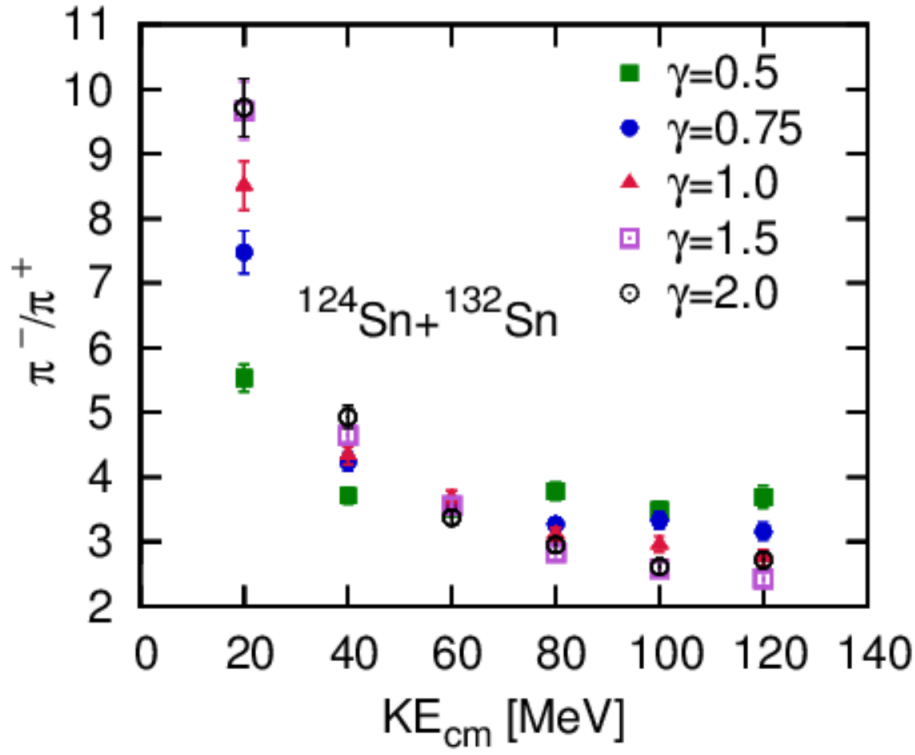


Figure 4.7 (Color online) Charged pion ratio in central  $^{124}\text{Sn}+^{132}\text{Sn}$  collisions at 300A MeV, as a function of kinetic energy in the center of mass frame, for different values of the stiffness  $\gamma$  of the symmetry energy, from 0.5 to 2.0.

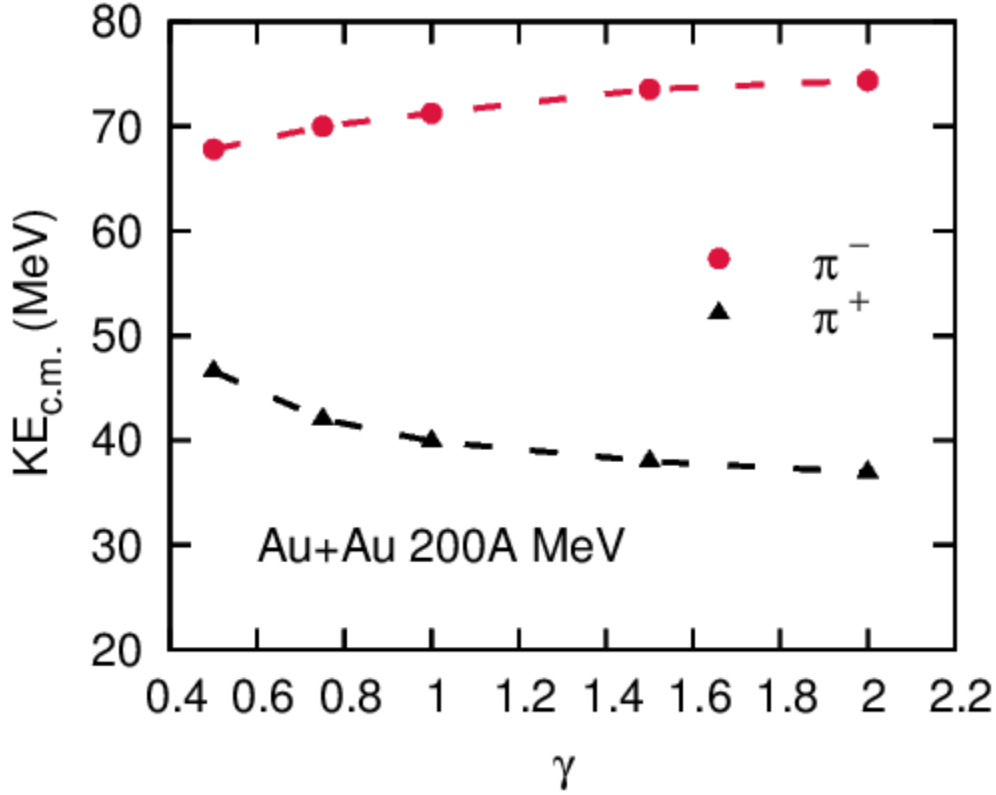


Figure 4.8 (Color online) Average center-of-mass kinetic energy of  $\pi^+$  and  $\pi^-$  in central Au+Au collisions at 200A MeV, plotted against stiffness  $\gamma$  of the symmetry energy.

The figures display competing effects of the isospin content of the system, of Coulomb interactions and of the symmetry energy. Obviously, the neutron excess generally makes negative pions more abundant than positive, with the effect amplified by larger isospin magnitude for the pions than for the nucleons. The long-range Coulomb interactions play the primary role in making the  $\pi^-/\pi^+$  ratio dependent on the energy of the emitted pions. Thus, after the pions cease to interact strongly and move out from the reaction region, described then by primordial spectra sharing to a degree characteristics between  $\pi^+$  and  $\pi^-$  (and  $\pi^0$ ), the Coulomb interactions accelerate  $\pi^+$  and decelerate  $\pi^-$ . The relative Coulomb push boosts the  $\pi^-/\pi^+$  ratios at low c.m. energies, above the overall ratio for the reactions, and lowers the ratios at high c.m. energies, see Figs. 4.6 and 4.7. The push also gives rise to substantially higher average c.m. energies for  $\pi^+$  than  $\pi^-$ , see Figs.

4.8.

Contributions to mean-field potentials associated with the symmetry energy principally act opposite to Coulomb interactions, but they act while pions continue to rescatter, in fact with large cross-sections due to the formation of  $\Delta$ -resonance, down to low densities. The scattering tends to erase the impact of different accelerations for  $\pi^+$  and  $\pi^-$  (and for nucleons and  $\Delta$ 's with different isospin as well) due to the isospin-dependence of mean fields. With the scattering rates being linear in density, the mean fields can win over the rescattering, in the low density region, if their dependence on density is slower than linear. The low-energy part of the spectrum is generally dominated by particles emitted from lower density regions, late in the history of the reactions. In Figs. 4.6 and 4.7, we can see that the symmetry energy is indeed effective in countering the effects of Coulomb enhancement of the low-energy  $\pi^-/\pi^+$  ratio, when  $\gamma < 1$  and the interaction symmetry energy is large at low densities. At  $\gamma > 1$ , the effect fizzles out. Notably excitation of the medium suppresses the role of Pauli principle and of the associated kinetic contribution to the symmetry energy. In Fig. 4.9, we can see that the impact of the stiffness of symmetry energy, on  $\pi^+ - \pi^-$  average-energy difference, weakens past  $\gamma \approx 1$ .

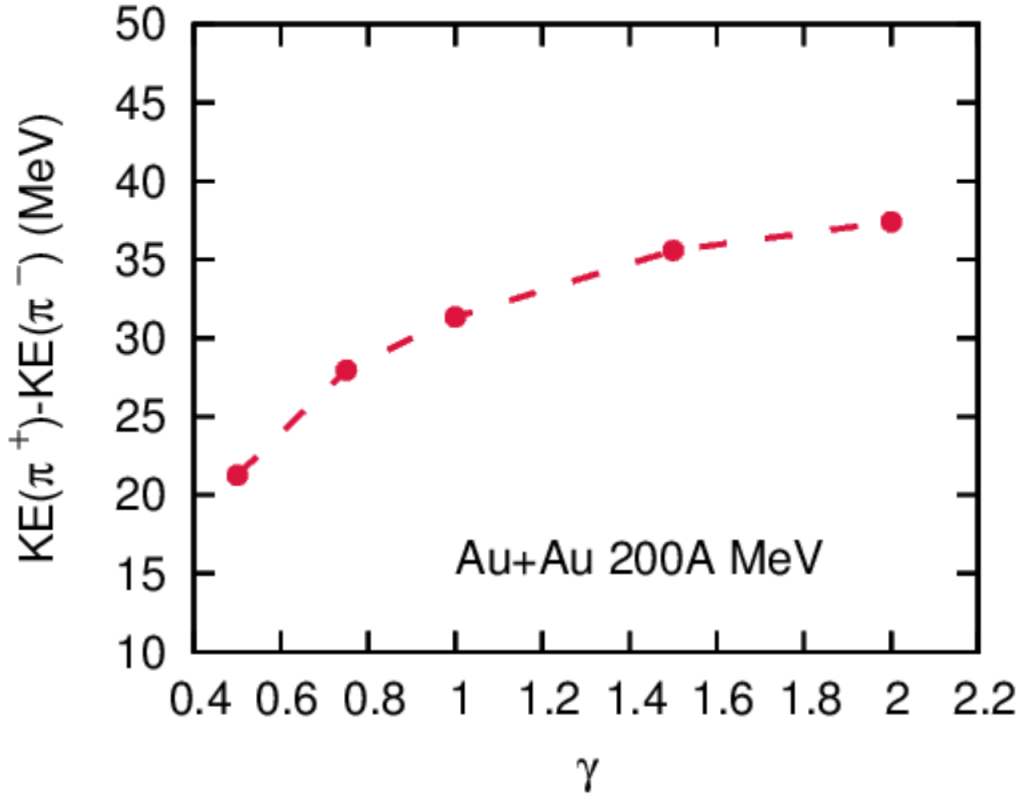


Figure 4.9 (Color online) Difference between average c.m. kinetic energy of  $\pi^+$  and  $\pi^-$  in central Au+Au collisions at 200A MeV, plotted against stiffness  $\gamma$  of the symmetry energy.

With regard to the particles emitted at higher c.m. energies, that tend to stem from early stages of the reaction and higher densities, another high-density effect of the symmetry energy comes into play. Namely, a stiff symmetry energy pushes away the neutron-proton asymmetry from the high-density region [25], see Fig. 4.10. With the reduction in the high-density asymmetry, the  $\pi^-/\pi^+$  ratio gets reduced at high c.m. energies. Thus, qualitatively a stiff symmetry energy acts in this energy region as the relative Coulomb boost, cf. Figs. 4.6 and 4.7. With this, it becomes possible to access the stiffness of high-density symmetry-energy through the high-energy  $\pi^-/\pi^+$  yield ratio.

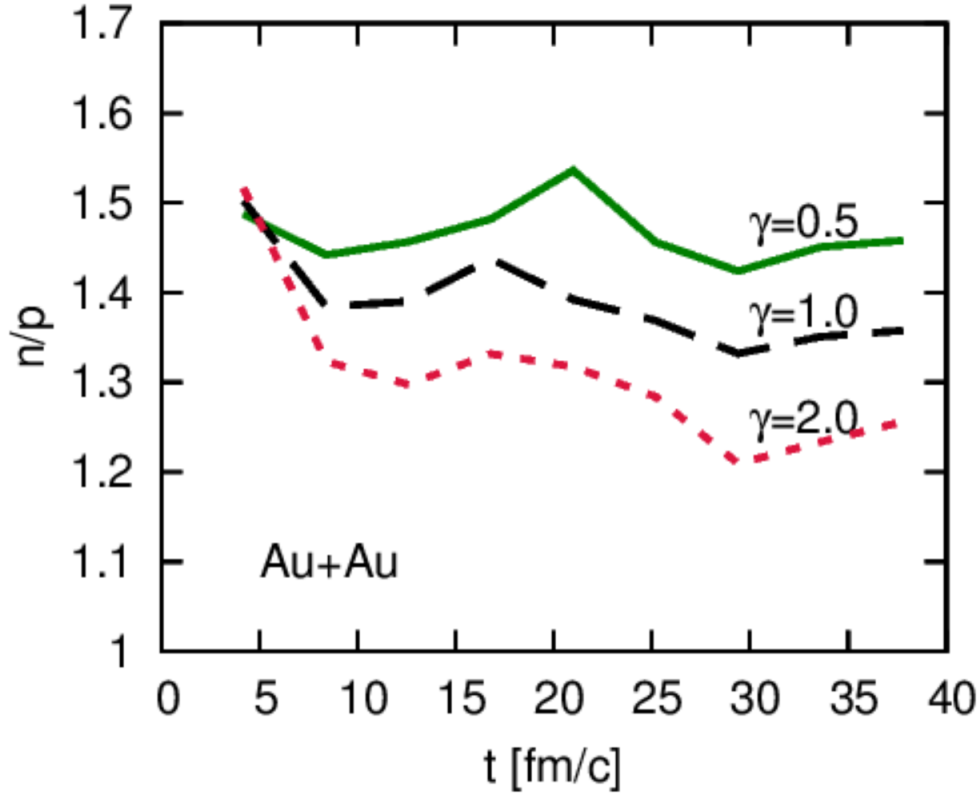


Figure 4.10 (Color online) Ratio of neutron-to-proton numbers at supranormal net densities,  $\rho > \rho_0$ , in central Au+Au collisions at 200A MeV, as a function of time. At early times, the numbers in the ratio are marginal, and the ratio, thus, not very meaningful.

In the earlier version[90] of this work, we also explored the  $\pi^-/\pi^+$  yield ratio in the direction out of the reaction plane as a probe of the symmetry energy at supranormal densities. In that direction the high-density matter is directly exposed to the vacuum. However, with a higher statistics in the calculations, our directional signal[90] for the symmetry energy has weakened.

## 4.6 Isospin fractionation

As to the symmetry energy below saturation density, and comparing the symmetry energy at low and high density, one useful probe is the isospin fractionation. Just as in nuclear ground state,

the neutron-proton imbalance in a reaction is likely to migrate in correlation with the behavior of the symmetry energy with density. At low density, a soft symmetry energy is higher than a stiff symmetry energy, and at high density, the stiff symmetry energy is higher. With this, in a system simulated with a soft symmetry energy, more of the neutron-proton imbalance is expected to be pushed to higher density and less to lower, as compared to a system simulated with a stiff energy. The regions of high density are more likely to contribute to emission of particles with high energy and those of low density to emission of particles with low energy. Thus, by studying relative yields of neutrons and protons as a function of particle energy, one may assess how symmetry energy changes with density. In the following, we examine the n/p ratios from pBUU simulations as a function of particle kinetic energy .

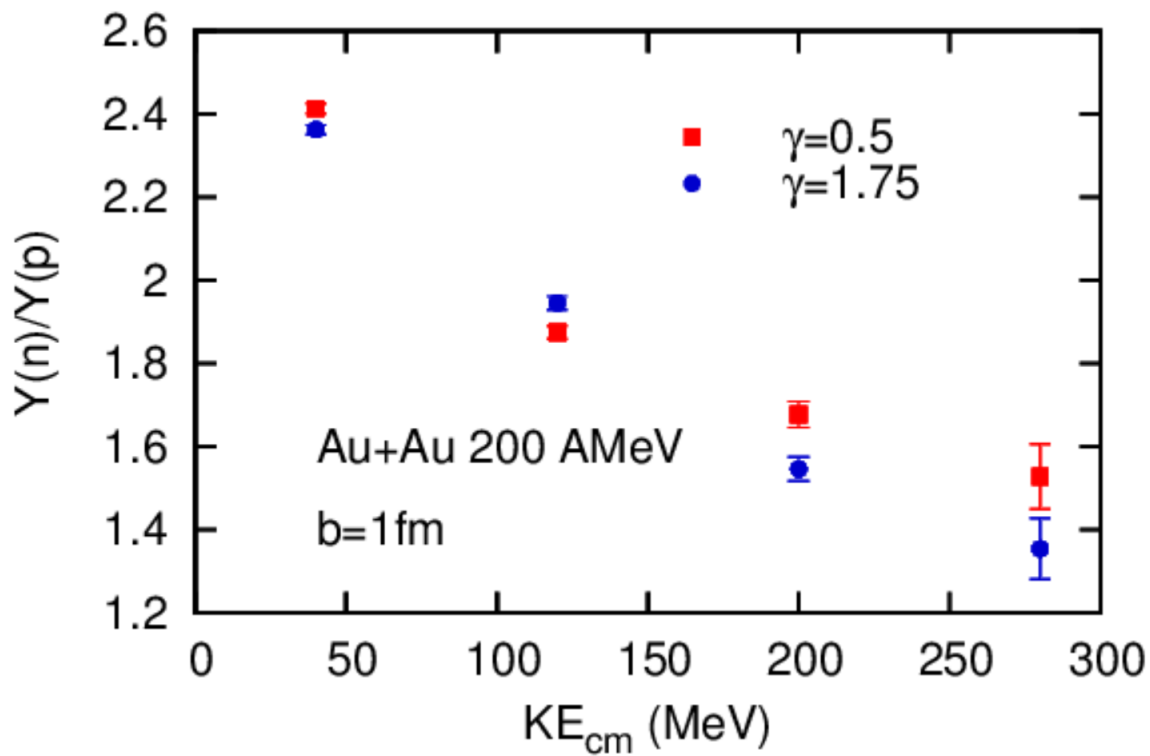


Figure 4.11 Ratio of neutron-to-proton numbers, in central Au+Au collisions at the beam energy of 200A MeV and impact parameter  $b=1$  fm, as a function of kinetic energy in center of mass frame.

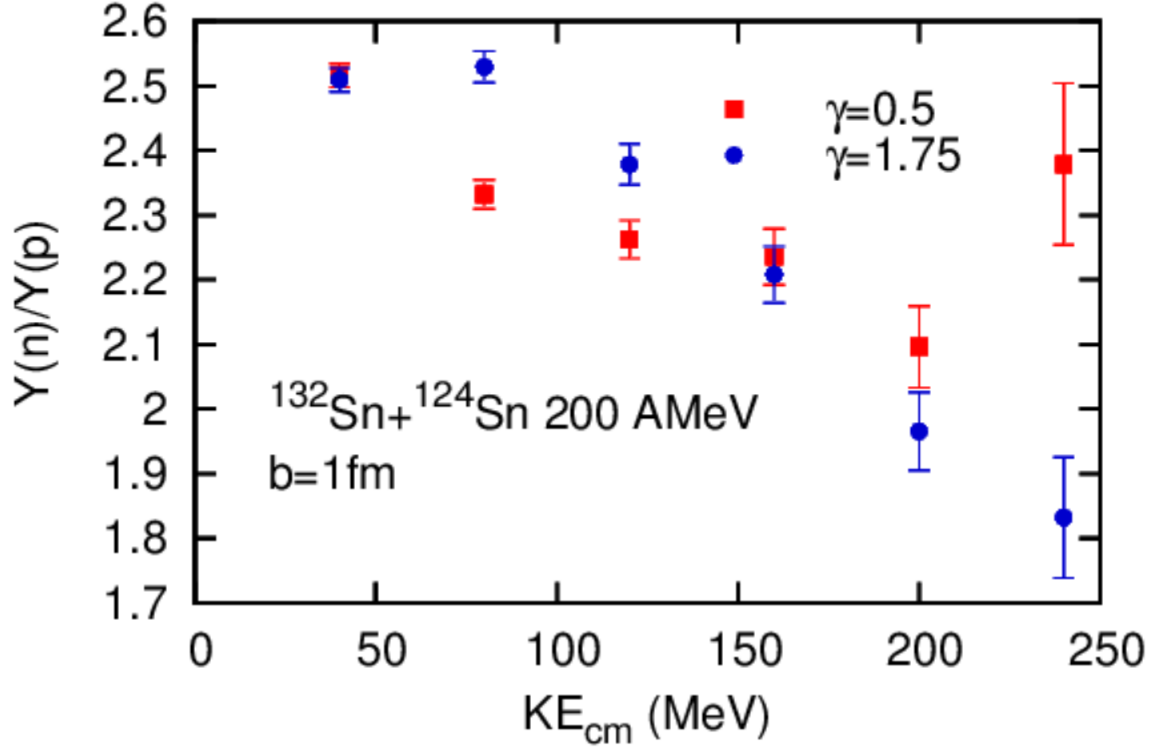


Figure 4.12 Ratio of neutron-to-proton numbers, in central  $^{132}\text{Sn}+^{124}\text{Sn}$  collisions at the beam energy of 200A MeV and impact parameter  $b=1\text{fm}$ , as a function of kinetic energy in center of mass frame.

We simulated the central nuclear collisions of Au+Au, as well as of  $^{132}\text{Sn}+^{124}\text{Sn}$ , at 200A MeV and impact parameter of  $b=1\text{fm}$ . A soft symmetry energy with parameter  $\gamma = 0.5$  and a stiff symmetry energy with parameter  $\gamma = 1.75$  have been chosen to test the sensitivity of n/p ratios to the stiffness of symmetry energy. The neutron-proton ratios as a function of the kinetic energy in center of mass frame are plotted in Fig. 4.11 for the Au+Au reactions and in Fig 4.12 for  $^{132}\text{Sn}+^{124}\text{Sn}$ . We see a definite system dependence of the n/p ratios when comparing the two figures. The net neutron-proton asymmetry  $\alpha$  at the start of the reaction is  $\approx 0.20$  for Au, and  $\approx 0.22$  for  $^{124}\text{Sn}+^{132}\text{Sn}$  system. The n-p ratios are indeed higher for the second system, but also they are higher than naively expected from the overall neutron-proton imbalance. This is because

of residual regions remaining at the end of a reaction simulation, persisting at moderate subnormal density that are going over time scales that are long compared to those for which semiclassical transport theory is appropriate. Those regions tend to trap protons to a larger extent than neutrons when the imbalance is present, enhancing the n-p ratio for free nucleons. The trapping itself can depend on the symmetry energy. Also note that, with different  $\gamma$ , n/p ratios are small compared to the pion ratios at this energy.

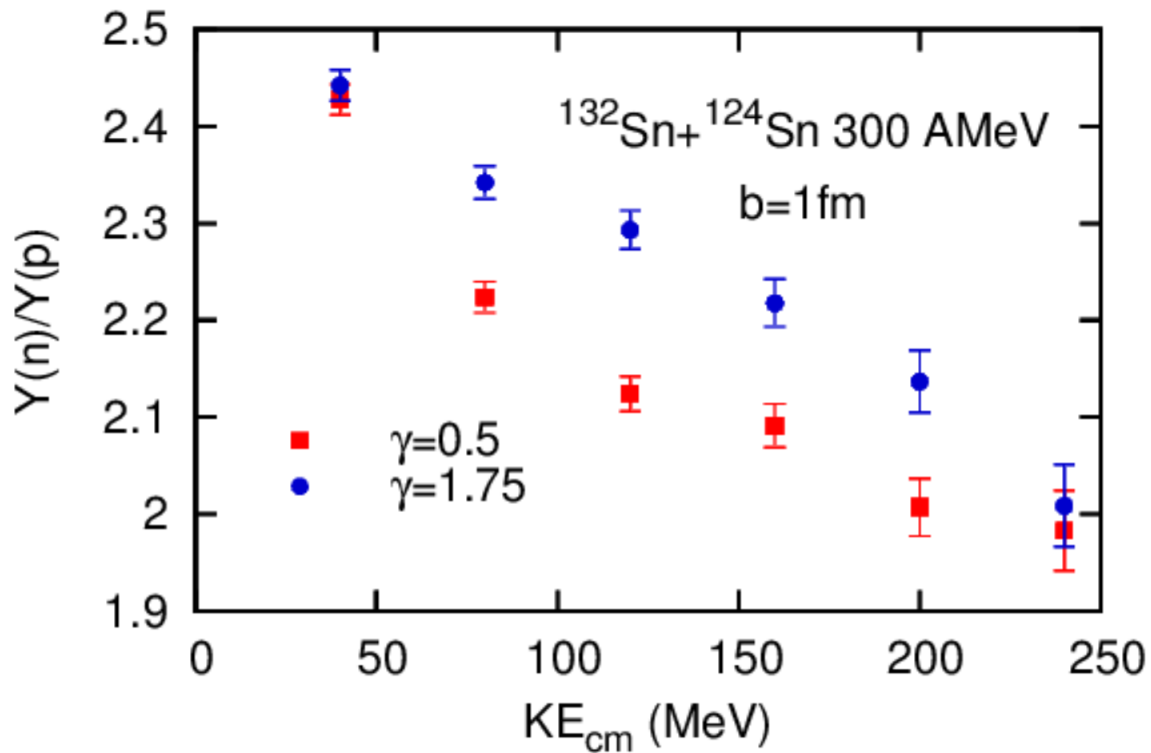


Figure 4.13 Ratio of neutron-to-proton numbers, in central  $^{132}\text{Sn}+^{124}\text{Sn}$  collisions at the beam energy of 300A MeV and impact parameter  $b=1\text{fm}$ , as a function of kinetic energy in center of mass frame.

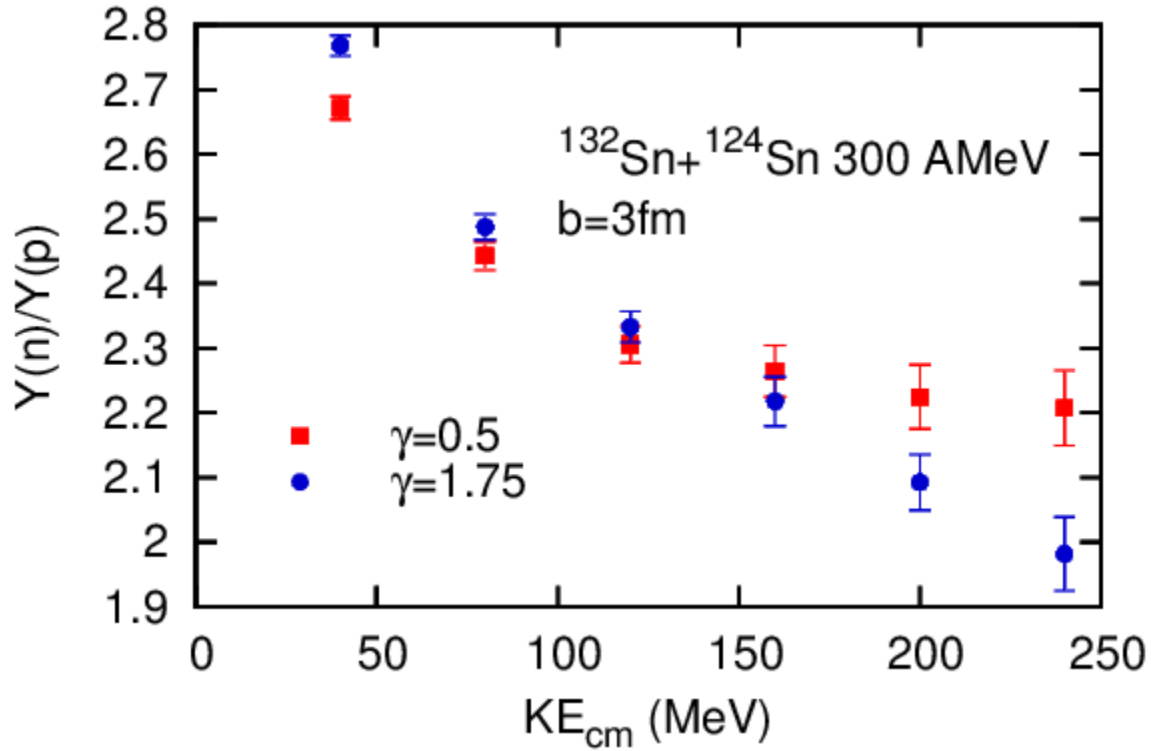


Figure 4.14 Ratio of neutron-to-proton numbers, in central  $^{132}\text{Sn}+^{124}\text{Sn}$  collisions at the beam energy of 300A MeV and impact parameter  $b=3\text{fm}$ , as a function of kinetic energy in center of mass frame.

In Fig. 4.13, we show n/p ratio calculations for  $^{132}\text{Sn}+^{124}\text{Sn}$  collision at higher beam energy of 300MeV/nucleon, at the impact parameter of  $b=1\text{fm}$ . Fig. 4.12 and 4.13 together demonstrate the dependence of n/p ratios on the beam energy. The overall fall of the n-p ratio with beam energy may be understood in the fact that the residual remnants are smaller in size at higher beam energy, hence the order of magnitude of the ratios for the remainder drifts towards n/p balance from the overall system asymmetry. Fig. 4.14 shows results from a calculation of  $^{132}\text{Sn}+^{124}\text{Sn}$  collision at 300MeV/nucleon, but now the calculation is at the impact parameter of  $b=3\text{fm}$ . At a higher impact parameter, the residual region increases in size and the n-p ratio for free nucleons drifts up again. Irrespectively of the impact parameter, beam energy, or system type, the high-energy n-p ratio is

always flatter as a function of energy for soft symmetry energy, and the low-energy ratio is always flatter for stiff, consistently with the expectation that the differential n-p yield ratio can be used to assess the symmetry energy both at the high and low density.

## 4.7 Conclusions

With a new parameterization for momentum-dependent MF, pBUU gives a reasonable description of pion multiplicities in moderate-energy central HIC. The puzzling finding is that the same parameterization of the MF momentum-dependence cannot be simultaneously used in describing the net pion yields around threshold and the high-momentum elliptic flow of protons. One potential avenue for resolving this puzzle is in the adjustment of nuclear incompressibility as described in Chapter 3. We compared our new momentum dependence of nucleonic optical potential with several microscopic calculations. The modified potential is within the realm of uncertainties for microscopic predictions, just like the previous potential.

Next, we used pion ratio observables to study the symmetry energy behavior at higher density than normal. While IBUU and ImIQMD yield opposing sensitivities to the density dependence of symmetry energy, for  $\pi^-/\pi^+$  net yield ratios, we find no significant sensitivity of that ratio to  $S(\rho)$  in pBUU. One factor affecting that sensitivity may be the pion optical potential in pBUU, driven by isospin asymmetry. We examined the dependence of charged pion ratio on pion c.m. energy in pBUU. To isolate the effect of symmetry energy at supranormal densities, we looked at the high energy tail of the spectra—where a clear sensitivity of pion ratio to different forms of supranormal symmetry energy is seen. Additionally, the difference of average c.m. kinetic energy of emitted  $\pi^+$  and  $\pi^-$  also shows a sensitivity to different symmetry energies. In Ref. [90], we applied combined energetic and angular cuts to the pion ratios and proposed it as a new differential observable for future experiments.

Lastly, we examined the impact of the density dependence of symmetry energy on the energy dependence of n/p yield ratio. Depending on the energy region, both the low- and high-density

dependence of the symmetry energy could be tested.

## CHAPTER 5

### GAUSSIAN QMC METHOD

#### 5.1 Introduction

Solving strongly correlated quantum many-body physics problems has been a challenge for theoretical physics. Because of the strong impact of interactions, use of perturbation theory can be questionable in such cases. The straight brute force approaches are not practical due to dimensionality and the intrinsic complexity of many-body wavefunctions. For fermionic systems, the notorious sign problem is encountered in numerical calculations, that inhibits understanding of many-body physics. The sign problem is encountered because fermion wavefunctions change sign under particle interchange. In numerical calculations, integrations need then to be carried out over functions that are highly oscillatory with positive and negative values nearly canceling each other. It becomes numerically expensive to obtain accurate results, and sampling errors become very large. The numerical sign problem is encountered in numerical calculations in many areas of physics, including lattice QCD calculations of quark matter and calculations of ultra-cold atomic Fermi gases. In condensed matter physics, the problem is encountered when tackling systems with strongly correlated electrons. In nuclear physics, where nucleons interact with each other through strong force, the sign problem limits application of ab-initio methods to light nuclei only. The Gaussian phase-space representation method has been developed in the context of dynamic and static problems in ultra-cold atomic physics[91, 92, 93]. It aims at simulating Boson and Fermion systems from first-principles. The density matrix of a system is expanded in the Gaussian phase-space basis that, by being overcomplete, allows for exclusively positive definite expansion coefficients. The quantum master equation for the density matrix is next cast into the form of a Fokker-Planck equation in the space of expansion coefficients. A Monte-Carlo sampling is used in solving the stochastic Ito stochastic equations equivalent to the Fokker-Planck equations. The

purpose of studying the Gaussian phase-space representation method in this thesis is to analyze the methodology and seek opportunities for its application to problems in nuclear physics.

## 5.2 Phase space methods

In 1932, Wigner brought the idea of an expectation value in quantum mechanics that corresponded to the classical probability function distribution in spatial coordinates and momenta[94]. Later, other constructions were put forward that aimed at providing simultaneous information on space and momentum for a system. These included the Husimi Q-function[95], P-representation[96, 97], complex P-representation, positive-P representation[98, 99], squeezed-state expansion[100], etc.

### 5.2.1 Classical phase-space representations

In 1963, Glauber[96] and Sudarshan[97] independently developed an important classical phase space method employing the coherent states as a basis for representing the density matrix of bosonic systems:

$$\hat{\rho} = \int P(\vec{\alpha}) |\vec{\alpha}\rangle \langle \vec{\alpha}| d^{2M} \vec{\alpha}. \quad (5.1)$$

In the above, M is dimension,  $\vec{\alpha}$  is an M-mode coherent state,  $P(\vec{\alpha})$  can be interpreted as the probability density. The method was later called Glauber-Sudarshan P-representation, and it was successfully employed in the quantum laser theories. However, since the specific basis could not describe entangled states, the application of classical phase space expansion became quite limited. In addition, due to incompleteness of the mapping, system evolution could result in negative values for P, incompatible with its interpretation as a probability.

### 5.2.2 Quantum phase-space representations

In 1980s, a positive P-representation was proposed, modified relative to original to allow for quantum entanglement in the expansion basis:

$$\hat{\rho} = \int P(\vec{\alpha}, \vec{\beta}) \frac{|\vec{\beta}\rangle\langle\vec{\alpha}|}{\langle\vec{\alpha}|\vec{\beta}\rangle} d^{2M}\vec{\alpha} d^{2M}\vec{\beta}. \quad (5.2)$$

Now the number of variables has been doubled, and off diagonal matrix elements got included in the expansion. The coefficients in the new basis can be chosen as positive and the method works well for Bosonic systems. However, complexity arises with fermionic coherent states in that Grassmann numbers get employed in the basis decomposition. Coherent states have been, in particular, used in path integrals for Fermions. The issue is that a Grassmann number is a mathematical construction made to obey anti-commutation relations and specific algebraic rules and it cannot be simply treated as probability.

### 5.3 Gaussian phase-space representation

Gaussian phase space representation uses a more generalized basis than coherent states, for both Bosons and Fermions. The Fermion operators are represented in pairs, hence no Grassmann numbers are needed within the algebra.

$$\hat{\rho}(t) = \int P(\vec{\lambda}, t) \hat{\Lambda}(\vec{\lambda}) d\vec{\lambda} \quad (5.3)$$

where  $P(\vec{\lambda}, t)$  is the probability distribution,  $\hat{\Lambda}$  is a member of the generalized basis and  $\vec{\lambda}$  represents the phase space coordinates. Regarding a connection to the classical phase-space representation,  $\hat{\Lambda}(\vec{\lambda})$  corresponds to  $|\alpha\rangle\langle\alpha|$  in the founding formula, and in connection to the quantum phase-space representation,  $\hat{\Lambda}(\vec{\lambda})$  corresponds to  $|\beta\rangle\langle\alpha|$ . The real time or imaginary time evolution of density matrix can be cast into a Liouville equation form:

$$\frac{\partial}{\partial t} \hat{\rho}(t) = \hat{L}(\hat{\rho}(t)). \quad (5.4)$$

Upon insertion of the expansion of the density matrix into the Liouville equation, the partial differential equation acquires an integro-differential form:

$$\int \frac{dP(\vec{\lambda}, t)}{dt} \hat{\Lambda}(\vec{\lambda}) d\vec{\lambda} = \int P(\vec{\lambda}, t) \hat{L}[\hat{\Lambda}(\vec{\lambda})] d\vec{\lambda}. \quad (5.5)$$

Actions in the Liouville operator can be mapped onto operations involving expansion coefficients (probability distribution) labeled in terms of phase-space variables, such as derivatives with respect to the variables and multiplication by the variables, i.e.  $\hat{\Lambda}$ . Integrating by parts and assuming vanishing of coefficients at infinity for a bounded system, we arrive at the following integro-differential equations for the distribution functions  $P(\vec{\lambda}, t)$ .

$$\int \frac{dP(\vec{\lambda}, t)}{dt} \hat{\Lambda}(\vec{\lambda}) d\vec{\lambda} = \int L'P(\vec{\lambda}, t) \hat{\Lambda}(\vec{\lambda}) d\vec{\lambda}. \quad (5.6)$$

For any arbitrary basis, the dynamical equation for the distribution function can be obtained:

$$\frac{dP(\vec{\lambda}, t)}{dt} = L'P(\vec{\lambda}, t). \quad (5.7)$$

If interactions in the system are of one-body and two-body type only, we arrive at a Fokker-Planck equation for  $P(\vec{\lambda}, t)$  containing only first-order and second-order derivatives.

$$\frac{dP(\vec{\lambda}, t)}{dt} = \left[ - \sum_{a=0}^p \frac{\partial}{\partial \lambda_a} A_a(\vec{\lambda}) + \frac{1}{2} \sum_{a,b=0}^p \frac{\partial}{\partial \lambda_a} \frac{\partial}{\partial \lambda_b} D_{ab}(\vec{\lambda}) \right] P(\vec{\lambda}, t). \quad (5.8)$$

The form of matrices A and D is determined during the mapping process, and they both turn out to be positive-definite. It can be shown that there exists an Ito stochastic equation equivalent to the above Fokker-Planck equation. As a result, the differential equation for P can be solved via Monte-Carlo sampling of the stochastic equation within the phase-space with  $\vec{\lambda}$  as a coordinate. Expectation values of the observables can be obtained from calculating moments of P. In the following subsections, we describe the Gaussian phase-space representations for Bosons and Fermions separately.

### 5.3.1 Gaussian phase-space representations for Bosons

For an M-mode bosonic system,  $\hat{\mathbf{a}}$  represents a column of annihilation operators, and  $\hat{\mathbf{a}}^\dagger$  a row of creation operators. Those operators satisfies the commutation relations:

$$[\hat{a}_i, \hat{a}_j^\dagger] = \delta_{ij}. \quad (5.9)$$

For convenience in manipulations, we next introduce 2M-vectors for complex numbers and operators  $\underline{\alpha}$  and  $\underline{\hat{a}}$ , and a displacement operator  $\delta \underline{\hat{a}}$ :

$$\delta \underline{\hat{a}} = \underline{\hat{a}} - \underline{\alpha} = \begin{pmatrix} \hat{\mathbf{a}} \\ \hat{\mathbf{a}}^\dagger \end{pmatrix} - \begin{pmatrix} \hat{\alpha} \\ \hat{\alpha}^\dagger \end{pmatrix} \quad (5.10)$$

The general Gaussian basis can be given a quadratic form in terms of the 2M-vectors:

$$\hat{\Lambda}(\vec{\lambda}) = \frac{\Omega}{\sqrt{|\underline{\sigma}|}} : \exp[-\delta \underline{\hat{a}}^\dagger \underline{\sigma}^{-1} \delta \underline{\hat{a}}/2] : \quad (5.11)$$

In the above expression,  $::$  represents normal ordering, introduced for algebraic purposes, in which all creation operators are moved to the left of the annihilation operators. In the case of Bosons, there is no sign changes associate with normal ordering:

$$: \hat{a}^\dagger \hat{a} : = \hat{a}^\dagger \hat{a}, \quad (5.12)$$

$$: \hat{a} \hat{a}^\dagger : = \hat{a}^\dagger \hat{a}. \quad (5.13)$$

Normal ordering applied to an exponential function of operators implies an expansion of the exponential into series and application of the normal ordering to each term in the series:

$$: \exp(\lambda \hat{a}^\dagger \hat{a}) : = \sum_{n=0}^{\infty} \frac{\lambda^n}{n!} \hat{a}^{\dagger n} \hat{a}^n. \quad (5.14)$$

The complex matrix elements in  $\underline{\sigma}$  play the role of phase-space variables that can have principally more physical content than just the classical coordinates  $(\vec{r}, \vec{p})$ :

$$\underline{\sigma} = \begin{bmatrix} \mathbf{I} + \mathbf{n} & \mathbf{m} \\ \mathbf{m}^+ & \mathbf{I} + \mathbf{n}^T \end{bmatrix}. \quad (5.15)$$

Here,  $\mathbf{n}$  and  $\mathbf{m}$ ,  $\mathbf{m}^+$  are complex M by M matrices, and  $\mathbf{m}$  and  $\mathbf{m}^+$  are two independent symmetric matrices. With those we can put together the phase-space variables for Bosons:

$$\vec{\lambda} = (\Omega, \alpha, \alpha^+, \mathbf{n}, \mathbf{m}, \mathbf{m}^+). \quad (5.16)$$

Among the variables,  $\Omega$  is the weight of different trajectories, of use in case of imaginary-time evolution,  $\alpha$  represents the eigenvalue of the annihilation operator  $\hat{a}$  associated with the coherent state  $|\alpha\rangle$ ,  $\hat{a}|\alpha\rangle = \alpha|\alpha\rangle$ .  $\alpha^+$  is the conjugate to  $\alpha$ . The matrix elements of  $\mathbf{n}$  represent the normal correlation between different pairs of modes; matrix elements of  $\mathbf{m}$  are the correlations of pairs of annihilation operators, and  $\mathbf{m}^+$  are the correlations of pairs of creation operators.

The generality of the Gaussian basis may be reduced and, in particular, the Gaussian basis for the positive-P representation takes on the following form:

$$\hat{\Lambda}_P(\Omega, \alpha, \beta) = \Omega \frac{|\alpha\rangle\langle\beta^*|}{\langle\beta^*|\alpha\rangle}. \quad (5.17)$$

Matrices  $(n)$ ,  $(m)$  and  $(m)^+$  are zero in this case. In this case, the mapping between the operators actions and phase-space operations is as follows:

$$\hat{\Lambda} = \Omega \frac{\partial}{\partial \Omega} \hat{\Lambda}, \quad (5.18)$$

$$\hat{\mathbf{a}}\hat{\Lambda} = \alpha\hat{\Lambda}, \quad (5.19)$$

$$\hat{\mathbf{a}}^\dagger\hat{\Lambda} = [\beta + \frac{\partial}{\partial \alpha}]\hat{\Lambda}, \quad (5.20)$$

$$\hat{\Lambda}\hat{\mathbf{a}} = [\alpha + \frac{\partial}{\partial \beta}]\hat{\Lambda}, \quad (5.21)$$

$$\hat{\Lambda}\hat{\mathbf{a}}^\dagger = \beta\hat{\Lambda}. \quad (5.22)$$

### 5.3.2 Gaussian phase-space representations for Fermions

For an M single-particle modes fermionic systems, creation and annihilation operators for each mode satisfy the anticommutation relations:

$$[\hat{b}_k, \hat{b}_j^\dagger] = \delta_{kj}, \quad (5.23)$$

$$[\hat{b}_k, \hat{b}_j]_+ = 0. \quad (5.24)$$

The subscripts k and j here span values from 1 to M. For convenience in manipulations, we can define an M-column vector  $\hat{\mathbf{b}}$  consisting of annihilation operators, and an M-row vector  $\hat{\mathbf{b}}^\dagger$  of creation operators. We can moreover define an extended vector with 2M operators as:

$$\underline{\hat{\mathbf{b}}} = \begin{pmatrix} \hat{\mathbf{b}} \\ \hat{\mathbf{b}}^{\dagger T} \end{pmatrix} \quad (5.25)$$

The phase-space variables can be similarly combined into an arrow vector  $\vec{\lambda}$ , and consequently a member of the Gaussian operator basis can be cast into the following general form:

$$\hat{\Lambda}(\vec{\lambda}) = \Omega \frac{1}{N} : \exp[-\underline{\hat{\mathbf{b}}}^\dagger \underline{\underline{\Sigma}} \underline{\hat{\mathbf{b}}}/2] : . \quad (5.26)$$

In the above, N is the factor that combines with the trace of the following Gaussian operator to 1.

The dimension of the complex matrix  $\underline{\underline{\Sigma}}$  is  $2M \times 2M$ , and that matrix can be expressed as

$$\underline{\underline{\Sigma}} = (\underline{\underline{\sigma}}^{-1} - 2\underline{\underline{I}}). \quad (5.27)$$

The matrix elements of  $\underline{\underline{\sigma}}$  are similarly defined and have similar physical content as in the case of Bosons:

$$\underline{\underline{\sigma}} = \begin{bmatrix} \mathbf{n}^T - \mathbf{I} & \mathbf{m} \\ \mathbf{m}^+ & \mathbf{I} - \mathbf{n} \end{bmatrix} \quad (5.28)$$

The matrix  $\underline{\underline{I}}$  is defined with

$$\underline{\underline{I}} = \begin{bmatrix} -\mathbf{I} & \mathbf{0} \\ \mathbf{0} & \mathbf{I} \end{bmatrix} \quad (5.29)$$

For fermionic systems, the phase-space coordinates are

$$\vec{\lambda} = (\Omega, \mathbf{n}, \mathbf{m}, \mathbf{m}^+). \quad (5.30)$$

To calculate an expectation value of an operator  $\hat{O}$ , one can use the following expression:

$$\langle \hat{O} \rangle = Tr[\hat{O}\hat{\rho}] / Tr[\hat{\rho}] = \frac{\int P(\vec{\lambda}, t) Tr[\hat{O}\hat{\Lambda}] d\vec{\lambda}}{\int P(\vec{\lambda}, t) \Omega d\vec{\lambda}} \equiv \langle O(\vec{\lambda}) \rangle_P. \quad (5.31)$$

## 5.4 Properties of Gaussian phase-space method for Fermions

Since the Gaussian phase-space representation is closely tied to the positive P representation, various desired features of the basis extend in a natural manner from one to another. For nuclear physics more important is the fermionic case and those features are less obvious in that case. Hence, we concentrate now on the aspects of the basis in that case. Some details relevant to the derivation can be found in the paper by J.F. Corney [92].

### 5.4.1 Single-mode Gaussian operator

First, we arrive at explicit expressions for single-mode Gaussian operators. Similarly to the normal ordering of the exponential function of Bosonic operators, the single-mode Gaussian operator for Fermions can be represented as a sum of series:

$$\hat{\Lambda}'_1(\mu) =: exp[-\mu \hat{b}^\dagger \hat{b}] :=: \sum_{k=0}^{\infty} \frac{1}{k!} (-\mu \hat{b}^\dagger \hat{b})^k := 1 - \mu \hat{b}^\dagger \hat{b}. \quad (5.32)$$

The Gaussian operator is left with two terms only because of the Pauli principle for Fermions and the normal ordering applied within each term. The trace of the operator above is then  $2 - \mu$ . Upon

introducing  $n = (1 - \mu)/(2 - \mu)$ , and  $\tilde{n} = 1 - n$ , the normalized Gaussian operator can be next expressed in terms of a new variable:

$$\hat{\Lambda}_1(n) = \tilde{n} : \exp[-(2 - 1/\mu)\hat{b}^\dagger \hat{b}] := \tilde{n}\hat{b}\hat{b}^\dagger + n\hat{b}^\dagger \hat{b}. \quad (5.33)$$

Equivalently we can write

$$\hat{\Lambda}_1(n) = \tilde{n}|0\rangle\langle 0| + n|1\rangle\langle 1|. \quad (5.34)$$

We can see that the Gaussian basis is a complete basis for the number-conserving single-mode Hilbert space. Within that space any density matrix can be expanded into Gaussian operators with positive-definite coefficients.

$$\hat{\rho} = \tilde{n}\hat{\Lambda}_1(0) + n\hat{\Lambda}_1(1). \quad (5.35)$$

## 5.4.2 Completeness

To prove the completeness of a Gaussian phase-space basis, we first expand the density matrix using states with definite occupations:

$$\hat{\rho} = \sum_{\vec{n}} \sum_{\vec{m}} |\vec{n}\rangle\langle \vec{n}| \hat{\rho} |\vec{m}\rangle\langle \vec{m}|. \quad (5.36)$$

Within the basis of  $|\vec{n}\rangle\langle \vec{m}|$ , each state can be occupied by zero or one Fermion. In total, the number-state projector has  $2^{2M}$  independent elements. The products of states form a complete basis for the density operator. In fact, since that basis contains non-Hermitian matrices, it is necessarily an overcomplete basis. One can find non-unique expressions for the expansion of the density matrix, as has been shown in the single-mode case.

## 5.5 Free gas

A noninteracting Fermi gas in equilibrium can be naturally described using the Gaussian phase-space representation. Thus, the Hamiltonian for free gas only contains diagonal single-particle energy terms:

$$\hat{H} = \hat{b}^\dagger \omega \hat{b}. \quad (5.37)$$

The evolution equation for grand canonical density matrix in inverse temperature/imaginary time is

$$\frac{d}{d\beta} \hat{\rho} = -\frac{1}{2} [H - \mu N, \hat{\rho}], \quad (5.38)$$

$$\frac{\partial}{\partial \beta} \hat{\rho} = -\frac{1}{2} (\hat{b}^\dagger \omega \hat{b} \hat{\rho} + \hat{\rho} \hat{b}^\dagger \omega \hat{b}). \quad (5.39)$$

Here,  $\beta$  is the scaled inverse temperature  $T = 1/k_B\beta$ , and  $\mu$  is the chemical potential associated with particle number.

The following mapping relations apply here for the thermal states:

$$\hat{b}^\dagger \hat{b} \hat{\rho} \rightarrow [n_k - \frac{\partial}{\partial n_k} (1 - n_k) n_k] P, \quad (5.40)$$

$$\hat{\rho} \hat{b}^\dagger \hat{b} \rightarrow [n_k - \frac{\partial}{\partial n_k} (1 - n_k) n_k] P, \quad (5.41)$$

$$\hat{\rho} \rightarrow -\frac{\partial}{\partial \Omega} \Omega P. \quad (5.42)$$

In consequence, we arrive at the first-order Fokker-Planck equation:

$$\frac{\partial P}{\partial \beta} = \sum_k \omega_k \left[ \frac{\partial}{\partial n_k} (1 - n_k) + \frac{\partial}{\partial \Omega} \Omega \right] n_k P. \quad (5.43)$$

The above equation can be recast into the differential equation set:

$$\dot{\Omega} = - \sum_k \omega_k \Omega n_k, \quad (5.44)$$

$$\dot{n}_k = -\omega_k n_k (1 - n_k). \quad (5.45)$$

The Fermi-Dirac distributions readily follow as a solution of the second part of the set and yield

$$n_k = \frac{1}{e^{\omega_k \beta} + 1}, \quad (5.46)$$

$$\Omega = \Omega_0 \prod_k e^{-\omega_k n_k \beta}. \quad (5.47)$$

## 5.6 Fermi-Bose modeling

Fermi-Bose model has been historically used in condensed matter physics for simulating the formation of two electrons into a bosonic Cooper pair. In the context of ultra-cold atomic physics, the model represents dissociation of a Bose molecule into two atomic constituents (two Bosons or two Fermions) and their reassociation. We tested the utility of the Gaussian operator representation for studying time evolution within a model where a single-mode Boson dissociates into two two-mode Fermions.

The Hamiltonian of the system is:

$$H = \hbar v \hat{a}^\dagger \hat{a} + \hbar \omega (\hat{b}_1^\dagger \hat{b}_1 + \hat{b}_2^\dagger \hat{b}_2) + \hbar g (\hat{a}^\dagger \hat{b}_1 \hat{b}_2 + \hat{a} \hat{b}_2^\dagger \hat{b}_1^\dagger). \quad (5.48)$$

In the above,  $\hat{a}^\dagger$  ( $\hat{a}$ ) is the creation (annihilation) operator for the quanta of the bosonic field, and  $\hat{b}_i^\dagger$  ( $\hat{b}_i$ ) are creation (annihilation) operators of the fermionic single-particle energy levels in, e.g. different spin states. The conserved combination of the atomic particle numbers is

$$N = 2\hat{a}^\dagger \hat{a} + \hat{b}_1^\dagger \hat{b}_1 + \hat{b}_2^\dagger \hat{b}_2. \quad (5.49)$$

As the Hamiltonian is quadratic in the operators, higher-order products of annihilation and creation operators will be factorized to products of the normal and anomalous densities:  $n_1 = \hat{b}_1^\dagger \hat{b}_1 = n_2 = \hat{b}_2^\dagger \hat{b}_2$ ,  $m = \hat{b}_1 \hat{b}_2$ ,  $m^+ = \hat{b}_1^\dagger \hat{b}_2^\dagger$ .

We consider a uniform system in a cubic box of side  $L$ , with atomic particle density  $\rho_0$ , and the total number of atoms equal to  $N = \rho_0 L^3$ . Applying the mean field approximation, where the bosonic operator  $a(t)$  is replaced by a real function  $\alpha(t)$ , we can arrive at the differential equations for the normal and anomalous densities:

$$\frac{dn_i}{dt} = 2g\alpha_0 \text{Re}\{m\}, \quad (5.50)$$

$$\frac{dm}{dt} = -2i(\omega - \nu)m + g\alpha_0(1 - 2n_i). \quad (5.51)$$

where  $i=1,2$ . The solution to the above equations are:

$$n_i = \frac{(g\alpha_0)^2}{(g\alpha_0)^2 + (\omega - \nu)^2} \sin^2(\sqrt{(g\alpha_0)^2 + (\omega - \nu)^2}t), \quad (5.52)$$

$$m = \frac{g\alpha_0}{\sqrt{(g\alpha_0)^2 + (\omega - \nu)^2}} \cos(\sqrt{(g\alpha_0)^2 + (\omega - \nu)^2}t) \sin(\sqrt{(g\alpha_0)^2 + (\omega - \nu)^2}t) - i \frac{g\alpha_0(\omega - \nu)}{\sqrt{(g\alpha_0)^2 + (\omega - \nu)^2}} \sin^2(\sqrt{(g\alpha_0)^2 + (\omega - \nu)^2}t). \quad (5.53)$$

The averaged bosonic molecule numbers can be next calculated exploiting conservation of atomic particle numbers (Eq. 5.44):

$$\alpha(t)^2 = N/2 - \frac{(g\alpha_0)^2}{(g\alpha_0)^2 + (\omega - \nu)^2} \sin^2(\sqrt{(g\alpha_0)^2 + (\omega - \nu)^2}t). \quad (5.54)$$

On the other hand, when employing the Gaussian operator basis, the density matrix of the system may be described in terms of six independent complex variables:  $(\alpha, \alpha^+, n_1, n_2, m, m^+)$ . The action of different operators can be mapped on the density operator. Applying the mapping identities in Eq. 5.17 - Eq. 5.20, the equations of motion for these variables follow:

$$\dot{n}_1 = ig(\alpha^+ m - \alpha m^+) - \sqrt{i}n_1(mW_1^* + m^+W_2^*), \quad (5.55)$$

$$\dot{n}_2 = ig(\alpha^+ m - \alpha m^+) - \sqrt{i}n_2(mW_1^* + m^+W_2^*), \quad (5.56)$$

$$\dot{m} = -ig\alpha(1 - n_1 - n_2) + \sqrt{i}[-(\omega - \nu)m^2W_1^* + n_1n_2W_2^*], \quad (5.57)$$

$$\dot{m}^+ = ig\alpha^+(1 - n_1 - n_2) + \sqrt{i}[n_1n_2W_1^* - (\omega - \nu)m^2W_2^*], \quad (5.58)$$

$$\dot{\alpha} = -igm - \sqrt{i}W_1, \quad (5.59)$$

$$\dot{\alpha}^+ = igm^+ + \sqrt{i}W_2. \quad (5.60)$$

In those equations,  $W_1(t), W_2(t)$  represent complex Gaussian noises that satisfy the relations:

$$\langle W_i(t)W_{i'}(t') \rangle = 0, \quad (5.61)$$

$$\langle W_i(t)W_{i'}^*(t') \rangle = \delta_{ii'}\delta(t - t'). \quad (5.62)$$

We have solved this set of Langevin equations numerically and we display the average number of molecules as a function of time in Fig. 5.1-5.2. For simplicity, the values for the parameters in Hamiltonian have been chosen as:  $g=1$ ,  $\alpha_0 = \sqrt{N/2}$ ,  $\omega - \nu = -0.1$ . The dashed lines represent analytic solution in Eq. 5.49. The difference between the Gaussian QMC method and the analytic solution is due to non-uniformity of the bosonic field and due to finite number of bosonic molecules. In the figure one can observe that, up to small errors that shrink as sampling is increased, the method produces the expected gradual decrease of Boson molecule number towards equilibrium. However, beyond a certain critical time, the error increases dramatically. For a given sampling size, such a dramatic growth of error is eventually reached around a time that little depends on sample size. Changing the system size or time step in the calculation have little effect on sampling error.

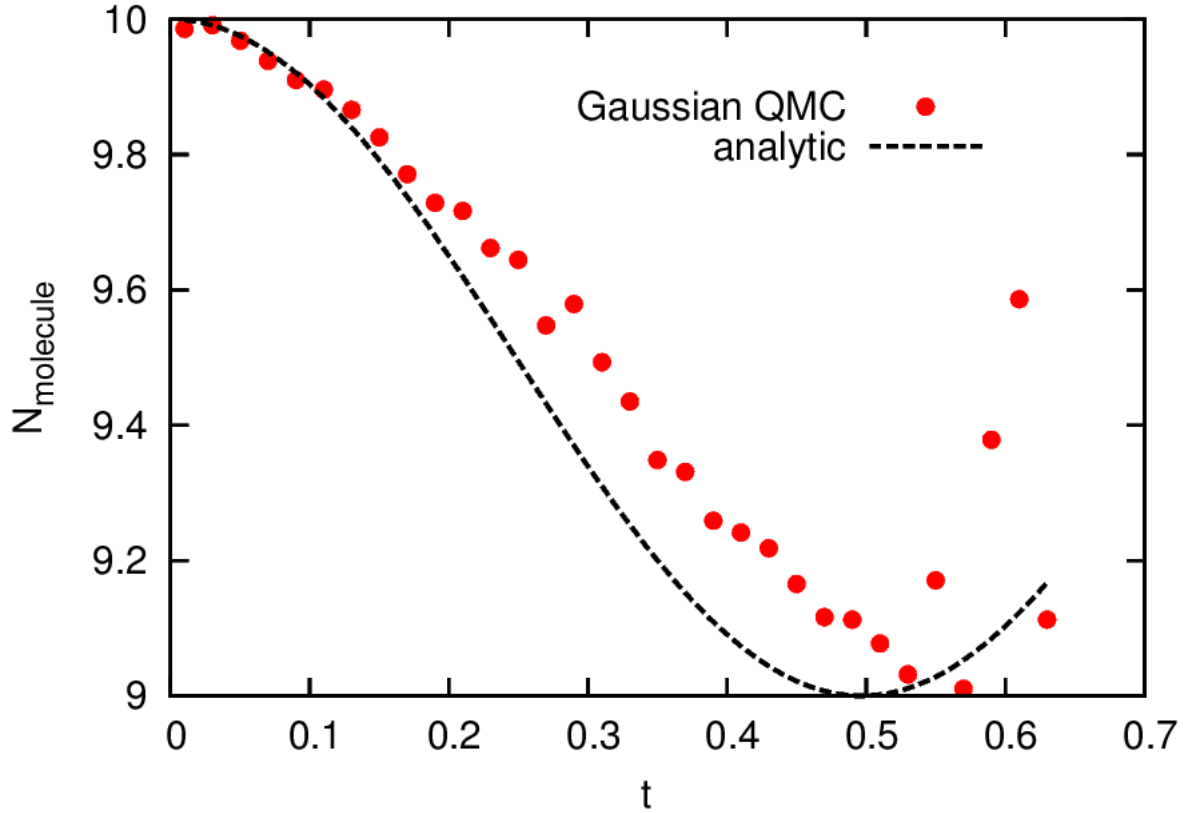


Figure 5.1 Average number of boson molecules as a function of time, in a system of single-mode boson molecules dissociating into two two-mode fermions, from a simulation within the Gaussian operator representation. Dashed line represent analytic solution using mean field approximation in Eq. 5.49. The system starts with 10 molecules and no fermions. In the specific case, the number bosonic molecules is calculated from the average 4000 trajectories. The sampling error is under control for a short time and then grows dramatically.

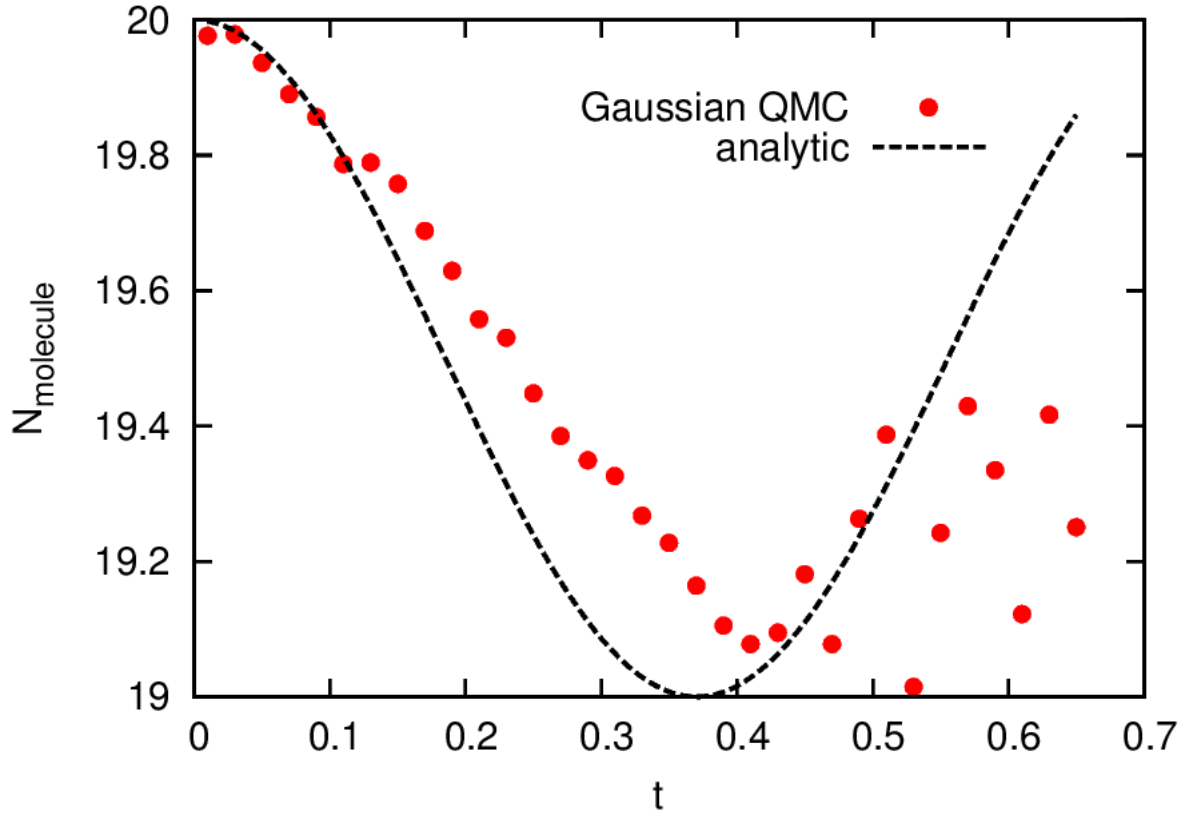


Figure 5.2 Average number of boson molecules as a function of time, in a system of single-mode boson molecules dissociating into two two-mode fermions, from a simulation within the Gaussian operator representation. Dashed line represent analytic solution using mean field approximation in Eq. 5.49. The system starts with 20 molecules and no fermions. In the specific case, the number bosonic molecules is calculated from the average 4000 trajectories. The sampling error is under control for a short time and then grows dramatically.

A good control of the sampling error for a certain time, followed by a dramatic growth in the error seems to be a generic feature of the Gaussian representation method. Notably, the growth in the particular case is around the time where the system appears to reach equilibrium and equilibrium is expected both for the average number of molecules and fluctuation of the number around equilibrium. Qualitatively different way of controlling sampling error for long times may be put forward, exploiting flexibility in the stochastic realization of the evolution equations. In this con-

text, we explored three specific stochastic gauges aiming at control of the sampling error. First was the Fermi gauge. For Fermion operators, any term with more than two fermionic operators vanishes on account of the Pauli principle. Correspondingly, one can add such terms to the Hamiltonian without affecting the physics, while altering the stochastic strategy. The second gauge we explored was the Diffusion gauge. The freedom of choosing that gauge follows from the square root of a matrix being non-unique. In mapping the Fokker-Planck equations onto the Ito stochastic equations, one has to evaluate a square root of the diffusion matrix - the extra freedom in the diffusion coefficients will change the stochastic noise. The third gauge we explored is the drift gauge. The freedom of employing that gauge follows from the following.

We attempted to use the latter two gauges in order to change the noise in stochastic calculations and extend the period over which solutions to the evolution in Gaussian operator representations could be of utility. However, any improvements in controlling the noise for long times turned out to be negligible. Similar difficulties have been encountered elsewhere when employing the Gaussian representations, no matter whether a system of Fermions or Bosons was investigated.

## **5.7 Conclusion**

In this chapter, we discussed the Gaussian phase-space representation method, which was before discussed in the literature only in the context of either condensed matter physics or physics of ultra-cold atomic systems. The method allows for a first-principle approach in solving quantum many-body problems, of special benefit for strongly correlated systems. The method relies on a general overcomplete Gaussian basis, both for Fermions and Bosons, and on expansion of the density matrix of a system within such basis has positive definite coefficients. Those coefficient can be interpreted as positive probability weights allowing to use the Monte-Carlo sampling for solving the time evolution. This approach in principle largely improves the efficiency in numerical calculations, and is able to deal with Hamiltonians of large dimensions that more transitional methods cannot cope with. The method can be employed to solve imaginary time as well as real time prob-

lems. The limitation of the method is that the system should only interact up to two-body force to maintain the expansion coefficients positive. Abrupt divergence in the sampling error appears to permeate the real-time evolutions in the Gaussian representations and has been illustrated here within the Fermi-Bose model.

## CHAPTER 6

### CONCLUSIONS

When parameterization of momentum-dependent MF is changed, pBUU can provide a reasonable description of pion multiplicities in moderate-energy central HIC. The puzzling finding is that the same parameterization of the MF momentum-dependence cannot be simultaneously used for describing the net pion yields around threshold and the high-momentum elliptic flow of protons. We compared our new momentum dependence of nucleonic optical potential with several microscopic calculations. The modified potential is within the realm of uncertainties for microscopic predictions, just like the previous potential.

Inspired by the recent elliptic flow analysis of the FOPI-IQMD Partnership, we studied the density dependence of nuclear mean field to arrive at constraints on equation of state of symmetric matter. By exploring a wider range of nuclear incompressibility and momentum-dependencies than before, we were able to reproduce pion yields and elliptic flow simultaneously. On the basis of that analysis we can conclude that the incompressibility  $K$  for nuclear matter is in the range of 240-300MeV. The deduced range of energies per nucleon and pressure for nuclear matter at moderately supranormal densities is fairly narrow and represents somewhat stiffer EOS than claimed by the FOPI-IQMD Partnership. The deduced constraints should be of utility in astrophysical modeling of supernova explosions and neutron stars.

Next, we used pion ratio observables to study the symmetry energy behavior at higher density than normal. While IBUU and ImIQMD yield opposing sensitivities to the density dependence of symmetry energy, for  $\pi^-/\pi^+$  net yield ratios, we find no significant sensitivity for that ratio to  $S(\rho)$  in pBUU. One factor affecting that sensitivity may be the pion optical potential in pBUU, driven by isospin asymmetry. We examined the dependence of charged pion ratio on pion c.m. energy. To isolate the effect of symmetry energy at supranormal densities, we looked at the high energy tail of the spectra—there a clear sensitivity of pion ratio to different forms of supranormal

symmetry energy is seen. Additionally, the difference of average c.m. kinetic energy of emitted  $\pi^+$  and  $\pi^-$  also shows a distinguishing power for different symmetry energies. In Ref. [90], we applied combined energy and angular cuts to the pion ratios and proposed it as a new differential observable for future experiments.

Finally, we explored the utility of the Gaussian phase-space representation methods for solving quantum many-body problems. We examined the basic properties of the Gaussian operator basis, and applications to the free gas problem and 3-mode Fermi-Bose model. We examined the use of gauge terms for coping with sampling errors. The method in general works better for many weakly-interacting particles than for a few strong-interacting particles. Unfortunately, the potential advantage of the Gaussian operator method for HIC, over any other method, would be expected in the latter limit.

## **BIBLIOGRAPHY**

## BIBLIOGRAPHY

- [1] W. Reisdorf and et al. (FOPI Collaboration). *Nucl. Phys. A*, 848:366, 2010.
- [2] D. Brill and et al. *Z. Phys. A*, 355:61, 1996.
- [3] A. Steiner and et al. *Phys. Rep.*, 411:325, 2005.
- [4] B. A. Li and et al. *Phys. Rep.*, 464:113, 2008.
- [5] H. Toki and et al. *Nucl. Phys. A*, 501:653, 2009.
- [6] U. Garg. *Nucl. Phys. A*, 791:3, 2004.
- [7] M. B. Tsang and et al. *Phys. Rev. C*, 76:034603, 2007.
- [8] G. A. Lalazissis and P. Ring J. Konig. *Phys. Rev. C*, 55:540, 1997.
- [9] A. Le Fevre, Y. Leifels, W. Reisdorf, J. Aichelin, and Ch. Hartnack. *Nucl. Phys. A*, 945:112, 2016.
- [10] M. B. Tsang, Y. Zhang, P. Danielewicz, M. Famiano, Z. Li, W. G. Lynch, and A. W. Steiner. *Phys. Rev. Lett.*, 102:122701, 2009.
- [11] A. Klimkiewicz and et al. *Phys. Rev. C*, 76:051603, 2007.
- [12] L. Trippa, G. Colo, and E. Vigezzi. *Phys. Rev. C*, 77:061304, 2008.
- [13] B. A. Brown. *Phys. Rev. Lett.*, 85:5296, 2000.
- [14] R. Serber. *Phys. Rev.*, 72:1114, 1947.
- [15] N. Metropolis, R. Bivins, M. Storm, J. Miller, G. Friedlander, and et al. *Phys. Rev.*, 110:204, 1958.
- [16] H. W. Bertini. *Phys. Rev.*, 131:1801, 1963.
- [17] J. Cugnon. *Phys. Rev. C*, 22:1885, 1980.
- [18] P. Carruthers and F. Zachariasen. *Rev. Mod. Phys.*, 55:245, 1983.
- [19] G. Bertsch, H. Kruse, and S. Gupta. *Phys. Rev. C*, 29:673, 1984.
- [20] H. Stocker and W. Greiner. *Phys. Rep.*, 137:277, 1986.
- [21] W. Bauer, G. Bertsch, W. Cassing, and U. Mosel. *Phys. Rev. C*, 34:2127, 1986.
- [22] G. Bertsch and S. Das Gupta. *Phys. Rep.*, 160:189, 1988.
- [23] P. Danielewicz and G. Bertsch. *Nucl. Phys. A*, 533:712, 1991.

- [24] D. R. Hartree. *Proc. Cambridge Phil. Sco.*, 24:89, 1928.
- [25] J. C. Slater. *Phys. Rev.*, 81:385, 1951.
- [26] M. Borromeo, D. Bonatsos, H. Muther, and A. Polls. *Nucl. Phys.*, A539:189, 1992.
- [27] J. Cugnon, T. Mizutani, and J. Vandermeulen. *Nucl. Phys. A*, 352:505, 1981.
- [28] L. P. Kadanoff and G. Baym. *Quantum Statistical Mechanics*, 1962.
- [29] P. Danielewicz. *Nucl. Phys. A*, 673:375, 2000.
- [30] L. Boltzmann. *Sitzungsberichte Akad. Wiss.*, 66:275, 1872.
- [31] E. A. Uehling and G. E. Uhlenbeck. *Phys. Rev.*, 43:552, 1933.
- [32] W. Cassing, V. Metag, U. Mosel, and K. Niita. *Phys. Rep.*, 188:363, 1990.
- [33] S. Teis, W. Cassing, M. Effenberger, A. Hombach, U. Mosel, and G. Wolf. *Z. Phys. A*, 356:421, 1997.
- [34] J. Aichelin. *Phys. Rep.*, 202:233, 1991.
- [35] C. Hartnack and et al. *Eur. Phys. J. A*, 1:151, 1998.
- [36] Q. Li, J. Wu, and C. Ko. *Phys. Rev. C*, 39:849, 1989.
- [37] B. Blaettel, V. Koch, and U. Mosel. *Rep. Prog. Phys.*, 56:1, 1993.
- [38] S. Bass, M. Belkacem, M. Bleicher, M. Brandstetter, L. Bravina, and et al. *Prog. Part. Nucl. Phys.*, 41:255, 1998.
- [39] E. Santini, M. Cozma, A. Faessler, C. Fuchs, M. Krivoruchenko, and et al. *Phys. Rev. C*, 78:034910, 2008.
- [40] W. Ehehalt and W. Cassing. *Nucl. Phys. A*, 602:449, 1996.
- [41] P. Danielewicz. *Phys. Rev. C*, 51:716, 1995.
- [42] P. Danielewicz. *Nucl. Phys. A*, 661:82, 1999.
- [43] C. Gale and et al. *Phys. Rev. C*, 41:1545, 1990.
- [44] B. Sinha. *Phys. Rep.*, 20:1, 1975.
- [45] F. Perey and D. S. Saxon. *Phys. Lett.*, 10:107, 1964.
- [46] P. Danielewicz, R. Lacey, and W. G. Lynch. *Science*, 298:1592, 2002.
- [47] B. Friedman and V. R. Pandharipande. *Nucl. Phys. A*, 361:502, 1981.
- [48] M. R. Anastasio, L. S. Celenza, W. S. Pong, and C. M. Shakin. *Phys. Rep.*, 100:327, 1983.

- [49] L. S. Celenza and C. M. Shakin. *Relativistic Nuclear Physics: Theories of Structure and Scattering*. World Scientific, Singapore, 1986.
- [50] B. ter Haar and R. Malfliet. *Phys. Rep.*, 149:207, 1987.
- [51] R. Brockmann and R. Machleidt. *Phys. Lett. B*, 149:283, 1984.
- [52] R. Brockmann and R. Machleidt. *Phys. Rev. C*, 42:1965, 1990.
- [53] M. Baldo, I. Bombaci, G. Giansiracusa, and U. Lombardo. *Phys. Rev. C*, 40:R491, 1989.
- [54] A. Insolia and et al. *Phys. Lett. B*, 334:12, 1994.
- [55] H. H. Gutbrod, A. M. Poskanzer, and H. G. Ritter. *Rep. Prog. Phys.*, 52:1267, 1989.
- [56] K. H. Kampert. *Ann. Rev. Nucl. Part. Phys.*, 15:691, 1989.
- [57] A. K. Chaudhur. *Advances in High Energy Physics*, 2013:693180, 2013.
- [58] A. Andronic and (FOPI collaboration). *Nucl. Phys. A*, 661:333, 1999.
- [59] C. H. Simon and P. Danielewicz. *Phys. Rev. C*, 87:054619, 2013.
- [60] J. Piekarewicz. *Phys. Rev. C*, 69:041301, 2004.
- [61] V. B. Soubbotin, V. I. Tselyaev, and X. Vinas. *Phys. Rev.*, 69:064312, 2004.
- [62] D. Vretenar, T. Niksic, and P. Ring. *Phys. Rev. C*, 68:024319, 2003.
- [63] S. Shlomo, V. M. Kolomietz, and G. Colo. *Eur. Phys. J. A*, 30:23, 2006.
- [64] J. R. Stone, N. J. Stone, and S. A. Moszkowski. *Phys. Rev. C*, 89:044316, 2014.
- [65] D. H. Youngblood et al. *Phys. Rev. Lett.*, 39:1188, 1977.
- [66] J. P. Blaizot. *Phys. Rep.*, 64:171, 1980.
- [67] J. Treiner, H. Krivine, and O. Bohigas. *Nucl. Phys. A*, 371:253, 1981.
- [68] S. Shlomo and D. H. Youngblood. *Phys. Rev. C*, 47:2, 1992.
- [69] Q. Pan and P. Danielewicz. *Phys. Rev. Lett.*, 70:2062, 1993.
- [70] P. Danielewicz et al. *Phys. Rev. Lett.*, 81:2438, 1998.
- [71] A. E. L. Dieperink, Y. Dewulf, D. Van Neck, M. Waroquier, and V. Rodin. *Phys. Rev. C*, 68:064307, 2003.
- [72] C. J. Horowitz and J. Piekarewicz. *Phys. Rev. Lett.*, 86:5647, 2001.
- [73] S. Typel and B. A. Brown. *Phys. Rev. C*, 64:027302, 2001.
- [74] L. W. Chen, C. M. Ko, and B. A. Li. *Phys. Rev. C*, 72:064309, 2005.

- [75] M. A. Famiano and et al. *Phys. Rev. Lett.*, 97:052701, 2006.
- [76] T. X. Liu and et al. *Phys. Rev. C*, 76:034603, 2007.
- [77] H. Muller and B. D. Serot. *Phys. Rev. C*, 52:2070, 1995.
- [78] S. R. Souza, M. B. Tsang, Donangelo, W. G. Lynch, and A. W. Steiner. *Phys. Rev. C*, 78:014605, 2008.
- [79] H. S. Xu and et al. *Phys. Rev. Lett.*, 85:716, 2000.
- [80] M. B. Tsang, W. A. Friedman, C. K. Gelbke, W. G. Lynch, G. Verde, and H. Xu. *Phys. Rev. Lett.*, 86:5023, 2001.
- [81] B. A. Li. *Phys. Rev. Lett.*, 88:192701, 2002.
- [82] M. Lattimer and M. Prakash. *The Astrophysical Journal*, 550:426, 2001.
- [83] M. Lattimer. *Annual Review of Nuclear and Particle Science*, 62:485, 2012.
- [84] J. M. Lattimer and Y. Lim. *ApJ*, 771:51, 2013.
- [85] M. B. Tsang and et al. *Phys. Rev. C*, 86:015803, 2012.
- [86] B. A. Li. *Nucl. Phys. A*, 734:593, 2004.
- [87] W. Reisdorf and et al. (FOPI Collaboration). *Nucl. Phys. A*, 781:459, 2007.
- [88] Z. Xiao, B. A. Li, L. W. Chen, G. C. Yong, and M. Zhang. *Phys. Rev. Lett.*, 102:062502, 2009.
- [89] Z. Q. Feng and G. M. Jin. *Phys. Lett. B*, 683:140, 2010.
- [90] J. Hong and P. Danielewicz. *arXiv*, 1307:7654, 2013.
- [91] J. F. Corney and P. D. Drummond. *Phys. Rev. A*, 68:063822, 2003.
- [92] J. F. Corney and P. D. Drummond. *J. Phys. A: Math. Gen*, 39:269, 2006.
- [93] J. F. Corney and P. D. Drummond. *Phys. Rev. B*, 73:125112, 2006.
- [94] E. P. Wigner. *Phys. Rev.*, 40:749, 1932.
- [95] K. Husimi. *Proc. Phys. Math. Soc. Jpn*, 22:264, 1940.
- [96] R. J. Glauber. *Phys. Rev.*, 131:2766, 1963.
- [97] E. C. G. Sudarshan. *Phys. Rev. Lett.*, 10:277, 1963.
- [98] S. Chaturvedi, P. D. Drummond, and D. F. Walls. *J. Phys. A*, 10:187, 1977.
- [99] P. D. Drummond and C. W. Gardiner. *J. Phys. A*, 13:2353, 1980.
- [100] F. Haake and M. Milkens. *J. Stat. Phys.*, 53:345, 1988.